On the Modelling of Collisions in Cold Particle Electron Sources

Master's Thesis

Tim Wyssling

Supervisor: Dr. A. Adelmann
AMAS, PSI

September 30, 2023

Abstract

Recent measurements indicate that cryo-cooled photo-injectors promise to be an important cornerstone in the quest for next generation high brightness electron sources. State-of-the-art sources are capable of producing electron beams with very low beam temperatures, which are correlated and potentially quantum-degenerate. Accurate simulations of these sources require a numerical model that includes inter-particle collisions in a way that is consistent with the low-temperature limit. This thesis investigates the quantum nature of the plasmas produced and reviews multiple approaches to modelling collisions with regard to their applicability. The approaches considered range from kinetic Boltzmann and Landau schemes, over to randomized models, such as cumulative collisions, up to models such as P^3M. On the grounds of effective potential theory pioneered by Baalrud and Daligault [1] it could be shown that classical approaches suffice for modern sources. An additional feature of this thesis includes a variational description of the P^3M algorithm, which is used for an in-depth analysis of the role of electrostatic boundary conditions in collision modelling.

Contents

I Collision Modelling for Ultracold Sources **3**

1 Introduction **4**
1.1 Cold Particle Electron Sources 4
1.2 Approaches to Collision Modelling 5

2 Effective Potential Theory **9**
2.1 Introduction: Debye Screening 9
2.2 Ornstein-Zernike Equation with Hyper-Netted Chain Approximation 10
2.3 Solving the Ornstein-Zernike Equation 12
2.3.1 Forcing Convergence: Initial Conditions and Damping 13
2.3.2 Comparison with Literature 16
2.3.3 Possible Reasons for Failure 17
2.3.4 Numerical Effective Potential 19

3 Inclusion of Quantum Effects **22**

4 Estimating the Significance of Pauli Repulsion **24**
4.1 Procedure 25
4.2 Results 27

II Review of Approaches to Collision Modelling **33**

5 Kinetic Description of Collision Dynamics **36**
5.1 Base Equations 36
5.1.1 Klimontovich 36
5.1.2 Liouville's Equation and Truncation Schemes 37
5.2 Boltzmann's Collision Operator 40
5.3 Landau's Approximation 41
5.3.1 Langevin Equation 46

6 Variational Description of Collision Dynamics **48**
6.1 Collisionless Lagrangian 48
6.1.1 Spatial Discretization 49
6.1.2 Temporal Discretization 51
6.2 Ewald's Summation 53
6.3 P^3M 54
6.4 Interplay with Boundary Conditions 58

7 Statistical Description of Collision Dynamics **68**
7.1 Random binary Collisions 68
7.2 Cumulative Collisions 69

III Summary **72**

IV Appendix **76**

A Numerical Transforms **77**
A.1 Discrete 3-dim Fourier Transform 77
A.2 Regularization 79

B Computation of Pauli's Potential **81**
B.1 Theoretical Basis 81
B.2 Numerical Transform 81
B.3 Continuation 82

C Reconstructing Distributions from a Pair Distribution Function **84**

D Classical Two-Body Scattering Cross Sections **85**
D.1 Classical Two-Body Scattering Theory 85
D.2 Rutherford's Cross Section 87
D.3 Cross Sections of Screened Potentials 88
D.4 Solving Classical Scattering Integrals 90
D.4.1 Root Solver 90
D.4.2 Scattering Integral Solver 90
D.4.3 Computing the Cross Section 92
D.4.4 Choice of Incident Impact Parameter 92

E Mirror Charge Configurations **94**

Part I

Collision Modelling for Ultracold Sources

Chapter 1

Introduction

1.1 Cold Particle Electron Sources

The performance of applications of electron particle sources, such as X-ray free electron lasers and electron diffraction imaging systems, depends strongly on the ability to generate and control high-brightness beams. The emittance of photo-injector sources has a lower limit that cannot be undercut. This limit is referred to as intrinsic emittance [2–4] and reads,

$$\varepsilon = \sigma_r \sqrt{\frac{\mathrm{MTE}}{mc^2}},$$

where MTE is the mean transverse energy of the electrons and σ_r the spot size of the laser used for excitation. The mean transverse energy can be directly connected to the physical temperature of the electrons [4–6],

$$\varepsilon = \sigma_r \sqrt{\frac{k_B T}{mc^2}}.$$

Recent experiments have shown that cryogenic cooling of photocathodes [6–9] or laser-ionization of optically trapped, ultracold gases [5, 10–12] allow for beams with effective temperatures as low as 10 K. The drastically decreased intrinsic emittance allows for higher brightness and consequentially these results pose a promising lead in the quest for ultra-low emittance electron sources. The comparison in table 1.1 highlights the increase in brightness that is currently possible, as well as the expected plasma temperature range for ultra-cold sources.

Observable	Magneto-Optical Trap	Ultra-Cold Photoinjector	Regular Photoinjector
e^- Temperature [K]	$<$10	50$<$	1e3 - 1e4
Beam Charge [pC]	1000	-	100-3000
Emittance [mm.mrad]	0.04	$\propto$ 0.05	1
Brightness [A/m^2·sr]	1e16	$\propto$ 1e16	1e12 - 1e13
Bunch Length [ps]	0.1-1	-	$<$ hundreds

Table 1.1: Data from [5], [7].

However, the performance of a source is not only dependent on the intrinsic emittance. The final emittance of the beam will certainly be larger than ε, as the emittance will grow due to inter-particle collision effects. As results by Pierce *et al.* [3] indicate, ultracold sources still promise a solid improvement. Nevertheless, for the purpose of precise simulations, we require a model that

includes collision effects into the transport model, in a way that accurately reflects the physical conditions. The main questions of this thesis is, how collision modelling is affected by the low temperature limit.

It must be noted that this question combines concepts from several different fields of study. This arises because collision (or transport) models are often rooted in statistical mechanics and plasma physics but are applied to problems routinely encountered in an accelerator setting. Although the intrinsic emittance provides an example, that an accelerator observable (the emittance) can be connected to statistical properties (the temperature) the conversion often requires approximations. Notably, whenever in the following chapters a particle number density is stated, it will be an estimation. In practice particle sources rarely have a homogeneous number density and are usually characterized by other metrics, such as bunch charge.

With this in mind, it can be said that ultracold sources operate in a regime that is characterized by extremely low temperatures (10 - 50 K) and moderate particle number densities (1e17 - 1e20 cm^{-3}). Consequentially, due to both strong coupling between individual particles as well as quantum mechanical effects, such as Fermi pressure, the physical picture is quite different compared to the high temperature limit. This thesis investigates the nature of these conditions and possible ways in which collision dynamics can be modelled for the purpose of an accelerator simulation of ultracold particle sources.

An additional complication that arises for photo-cathode based sources is the presence of electrostatic boundary conditions. The interplay between boundaries and collision modelling will be investigated over the course of this thesis as well.

1.2 Approaches to Collision Modelling

In the following an abbreviated overview over collision models will be given. The different models will be reintroduced later with greater attention to detail.
Considering a configuration of N classical charged particles, as in figure 1.2, a full description of the dynamics can be given by solving Newton's equations, i.e. a system of N coupled second order differential equations. In other words the electrostatic energy of particle j in a configuration is given as the sum over all interactions,

$$E_j = \frac{e^2}{4\pi\varepsilon_0} \sum_{i \neq j}^{N} \frac{1}{|\mathbf{r}_i - \mathbf{r}_j|},$$

where $\mathbf{r}_i$ is the position of particle i. Given that this was computationally possible, there would be no need for a collision model, as the entire interaction would be described. The need for including collisions separately arises only, when an approximation was made at some point. The collisional dynamics then account for everything that e.g. the mean-field description neglected. In this sense, collisions are artificially re-introduced electromagnetic interaction.

One possible way to categorize collision models is shown in figure 1.4. The base equations are placed in the centre and describe the time evolution completely. Since the direct solution of e.g. Liouville's equation is mostly impossible, appropriate simplifications have to be made. Either, one solves the full Liouville equation approximately, or the equation itself is simplified first.

Schemes like the fast-multipole-method (FMM) [13, 14] or Ewald-Splitting-based methods [15], such as $\mathrm{P}^3\mathrm{M}$ [16–18], distinguish between far-field and near-field interaction and are - in the above sense - to be considered as collision models as well. Usually, the far-field is solved in a mean field

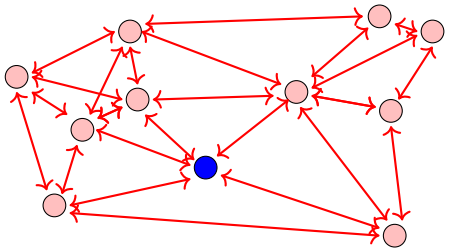

Figure 1.1: Illustration of a configuration of particles, where a particle interacts directly with $N-1$ others, which interact among themselves

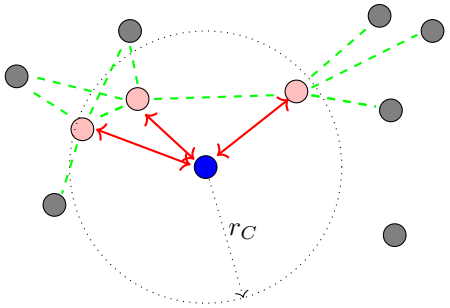

Figure 1.2: Illustration of a configuration of particles, where a particle interacts directly with close neighbours, which interact with their immediate surroundings.

approach, whereas the near-field interaction is computed by direct summation. A visualization of this procedure is shown in figure 1.2. These schemes provide an approximate solution to Newton's equations and can be fully described via Lagrangian formalism. How the electrostatic energy is computed in this case will be detailed in chapter 6.

One can understand this approximation in terms of statistical correlation. By virtue of Newton's equations the position and velocity of each particle depends on the position of all other particles within the configuration. Through this dependency the particle positions are statistically correlated with each other. Considering figure 1.2, the *direct correlation* between particles is given through the direct interaction with near neighbours and the *indirect correlation* summarizes everything that was neglected. In schemes like FMM or $\mathrm{P^3M}$ there is an implicity assumption that r_C is chosen such that the indirect correlation, that remains, can be approximated well with either a mean-field approach or a multipole expansion respectively. Naturally, if the cut-off radius r_C is chosen large enough, the entire interaction is computed directly and there is no approximation.

An additional simplification can be made by considering only two-particle interactions in the collision dynamics [19–27]. This approximation is known as *binary collision picture* and requires that the indirect correlation between particles is negligible. In terms of the electrostatic energy, this can be written as follows,

$$E_j = \underbrace{\boxed{\frac{e^2}{4\pi\varepsilon_0}\frac{1}{|\mathbf{r}_i-\mathbf{r}_j|}}}_{\text{dir. corr.}} + \underbrace{\boxed{\gamma(|\mathbf{r}_i-\mathbf{r}_j|)k_BT}}_{\text{ind. corr.}} \approx \underbrace{\boxed{\frac{e^2}{4\pi\varepsilon_0}\frac{1}{|\mathbf{r}_i-\mathbf{r}_j|}}}_{\text{dir. corr.}}, \tag{1.1}$$

where $\gamma = \gamma(r, T, \rho)$ quantifies the contribution of indirect correlation and i is reasonably close to j. Regarding the dimensions it is understood that γ denotes an energy measured in units of thermal energy.

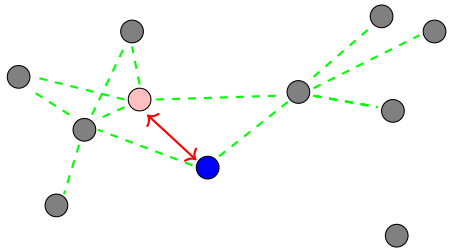

Figure 1.3: In the binary collision picture only two particles interact and indirect correlation is neglected.

One can equivalently describe the dynamics in macroscopic terms with a distribution function $f(\mathbf{x}_1, \mathbf{x}_2, ...)$ in the 6N-dimensional phase space, where $\mathbf{x}_i = (\mathbf{q}_i, \mathbf{p}_i)$ consists of position and momentum of the i-th particle. The base equation is known to be Liouville's equation,

$$\frac{df}{dt} = 0,$$

which provides an equivalent to Newton's equations on the macroscopic scale and is equally costly to solve directly. The kinetic approach is to simplify Liouville's equation first, before (approximately) solving it, which can be achieved by writing out the RHS. One distinguishes the diffusion term, which contains the mean field, and the collision operator, which contains everything else. Through the introduction of the Bogoliubov-Born-Green-Kirkwood-Yvon-Hierarchy (BBGKY) this abstract equation can be brought to workable forms, yielding Boltzmann's or Landau's collision operator [28]. In order to translate the macroscopic equation into particle equations of motion, one can discretize the operators in velocity space using Monte Carlo methods [29–31], or - in the case of Landau's operator - reformulate the equation to Langevin's form [32–37].

In the fluid limit, one can further simplify by expanding Boltzmann's equation in a moment expansion which is warranted, as long as the matter can be treated as a continuous system. Useful branches with many applications, such as Magneto-Hydro-Dynamics (MHD), have their roots in this treatment [38]. For the purpose of this thesis, these models are generally not of interest, since electrons cannot be reasonably considered in the fluid limit in most contexts.

The low temperature limit is characterized by the loss of validity of classical plasma physics assumptions. The typical [39] parameters to distinguish the regimes from one another are the Coulomb logarithm λ, the Plasma coupling parameter Γ and the electron degeneracy parameter (or Fermi pressure) Θ. Since the Coulomb logarithm will be subject of chapter 5, we will focus the on the remaining two, in order to motivate the problem. The plasma coupling parameter is defined the ratio between electrostatic and thermal energy,

$$\Gamma = \frac{E_\mathrm{C}}{k_B T}.$$

The higher Γ, the more important are collisional and indirect correlation effects. If indirect correlations are relevant, the binary collision assumption fails and a collision event consists not only of two collision partners, but includes every other particle that is correlated with either of the two. In contrast the assumption works reasonably well, as long as the particles are weakly correlated.

The plasma degeneracy parameter is the ratio between thermal and Fermi energy,

$$\Theta = \frac{k_B T}{E_F}.$$

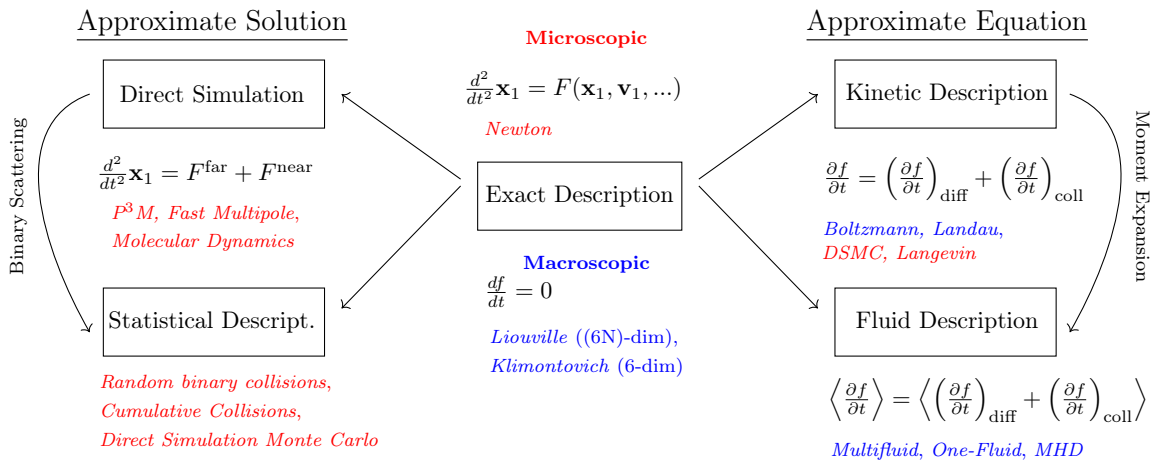

Figure 1.4: Overview over collision modelling approaches. In the figure F denotes a force, f a phase space distribution function, $\mathbf{x}$ a position coordinate and $\langle\cdot\rangle$ a mean value. The term $\left(\frac{\partial f}{\partial t}\right)_{\text{diff}}$ refers to the diffusion term in Boltzmanns original notation, which contains the mean field. In the same notation $\left(\frac{\partial f}{\partial t}\right)_{\text{coll}}$ represents the collision operator. Microscopic descriptions based around particle equations of motion are colored red, whereas macroscopic descriptions based around distribution functions are given in blue.

The smaller Θ, the more important are quantum effects generally and Pauli repulsion specifically. For a typical ultracold photo-cathode based source ($\rho \approx 1e18$ cm^{-3}, $T = 50$ K) we get $\Gamma \approx 46$, $\theta \gtrsim 1$. For comparison the uncorrelated/non-degenerate regime is given by approximately $\Gamma \gtrapprox 0.1$, $\theta \lll 1$. This rough estimate indicates, that the modelling of ultra-cold plasma potentially requires the inclusion of correlation effects and quantum corrections. It stands to question, how the collision modelling approaches mentioned above fare under these conditions and how an ideal model would present itself.

This main part of this thesis is divided in two parts. The first part is dedicated to the quantum nature of the electron beam. Through using an effective interaction potential it will be estimated how relevant quantum mechanical effects are in the description of ultracold electron particle sources. The second part reviews various approaches to collision modelling with special consideration of their applicability in the low temperature limit. In addition to the ones already mentioned the models considered include kinetic Boltzmann schemes, cumulative collisions and others.

Chapter 2

Effective Potential Theory

In the following chapter the concept of an effective interaction potential will be introduced. The results of Baalrud and Daligault [1] will be summarized and it will be shown how the binary collision approximation can be retained even in the presence of strong coupling.

2.1 Introduction: Debye Screening

The idea behind an effective potential is to include several physical effects into a single potential. The approximation of (1.1) is refined in the following way,

$$E_j = \underbrace{\boxed{\frac{e^2}{4\pi\varepsilon_0}\frac{1}{|\mathbf{r}_i - \mathbf{r}_j|}}}_{\text{dir. corr.}} + \underbrace{\boxed{\gamma(|\mathbf{r}_i - \mathbf{r}_j|)k_B T}}_{\text{ind. corr.}} \approx \underbrace{\boxed{e\Phi(|\mathbf{r}_i - \mathbf{r}_j|)}}_{\text{eff. corr.}}, \tag{2.1}$$

where Φ is an *effective interaction potential*. This is illustrated for a configuration of particles in figure 2.1.
The most prominent example of this technique in plasma physics is Yukawa's potential, which accounts for charge screening. The potential has an analytic form that can be derived using Poisson's equation. The necessary assumption is that the density of particles $\rho(\mathbf{x})$ follows a Maxwell-Boltzmann distribution,

$$\rho(\mathbf{x}) = \rho^0 e^{-\frac{q\phi(\mathbf{x})}{k_B T}}, \tag{2.2}$$

where $q\phi$ is the Coulomb potential energy, ρ^0 a constant number density and $k_B T$ the thermal energy. This can be inserted into Poisson's equation, which yields,

$$\nabla^2\phi(\mathbf{x}) = \rho^0 e^{-\frac{q\phi(\mathbf{x})}{k_B T}}.$$

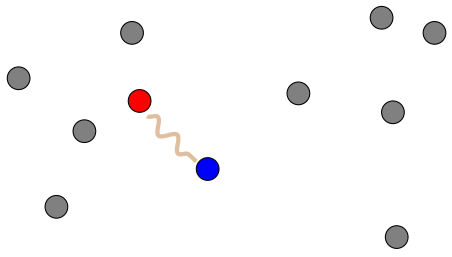

Figure 2.1: Illustration of a configuration of particles, where a particle interacts directly with only one other particle, but with an effective interaction potential.

The solution is known as Yukawa's potential,

$$\phi_Y = \frac{e^{-\frac{r}{\lambda_D}}}{r}, \tag{2.3}$$

where λ_D is the Debye length. Typically, this is a good approximation for the interaction potential in weakly coupled ($\Gamma < 0.01$) classical ($\Theta < 1$) plasmas. For non-neutral plasmas there is a similar effect, as shown by F. Ruggiero [40], as long as the shielding length is small compared to the extension of the configuration.

In other words, an effective potential mediates the interaction between two particles, while considering the influence of their environment. Moreover, effective potentials provide a useful way to use the binary collision picture, without neglecting collective and correlation effects by including them directly into the interaction.

2.2 Ornstein-Zernike Equation with Hyper-Netted Chain Approximation

If two particles interact via electromagnetic forces, their positions and velocities are statistically correlated. In a bunch of many particles all of them are correlated to some degree, as Coulomb's potential has infinite reach.

As mentioned previously, one can further distinguish correlation effects into *direct* and *indirect* effects. The former describes the interaction between two particles, whereas the latter consists of the interaction with all other third-party correlated particles. In a weakly coupled plasma, the two of them together make up Yukawa's potential. The Ornstein-Zernike equation is a relationship between direct and indirect correlations and allows to calculate them even in the strong coupling regime. The knowledge of both correlation functions can be used to find an effective potential for this regime. The idea of using this approach for plasma physics was originally introduced by Baalrud and Daligault [1, 41, 42]. In the following a brief introduction to the method will be provided.

A thorough derivation of the relation will not be given here and can be found in e.g. [43]. The notation of Busigin and Phillips [44] will be used, which denotes the indirect correlation function by $\gamma(\mathbf{r})$, the direct correlation function by $c(r)$ and the total correlation function as $h(\mathbf{r}) = \gamma(\mathbf{r}) + c(\mathbf{r})$. With this notation the Ornstein-Zernike equation for a one-component plasma reads,

$$\gamma(\mathbf{r}) = \rho \int d^3\mathbf{s}\; c(\mathbf{r}-\mathbf{s})h(\mathbf{s}). \tag{2.4}$$

For easier evaluation this is mostly used in Fourier form,

$$\hat{\gamma}(\mathbf{k}) = \frac{\rho\hat{c}^2(\mathbf{k})}{1-\rho\hat{c}(\mathbf{k})}. \tag{2.5}$$

For two components $1, 2$ with densities ρ_1, ρ_2 the functions are generalized to matrices, e.g. $c(\mathbf{r}) \rightarrow$

$c_{ij}(\mathbf{r})$, which describe the correlations between components i and j,

$$\begin{aligned}
\gamma_{11}(\mathbf{r}) &= \rho_1 \int d^3\mathbf{s}\; c_{11}(\mathbf{r}-\mathbf{s})h_{11}(\mathbf{s}) + \rho_2 \int d^3\mathbf{s}\; c_{12}(\mathbf{r}-\mathbf{s})h_{21}(\mathbf{s}) \\
\gamma_{22}(\mathbf{r}) &= \rho_1 \int d^3\mathbf{s}\; c_{21}(\mathbf{r}-\mathbf{s})h_{12}(\mathbf{s}) + \rho_2 \int d^3\mathbf{s}\; c_{22}(\mathbf{r}-\mathbf{s})h_{22}(\mathbf{s}) \\
\gamma_{12}(\mathbf{r}) &= \rho_1 \int d^3\mathbf{s}\; c_{11}(\mathbf{r}-\mathbf{s})h_{12}(\mathbf{s}) + \rho_2 \int d^3\mathbf{s}\; c_{12}(\mathbf{r}-\mathbf{s})h_{22}(\mathbf{s}) \\
\gamma_{21}(\mathbf{r}) &= \rho_1 \int d^3\mathbf{s}\; c_{21}(\mathbf{r}-\mathbf{s})h_{11}(\mathbf{s}) + \rho_2 \int d^3\mathbf{s}\; c_{22}(\mathbf{r}-\mathbf{s})h_{21}(\mathbf{s}).
\end{aligned} \tag{2.6}$$

The Fourier transformed version reads accordingly [45],

$$\begin{aligned}
\hat{\gamma}_{11} &= \frac{\rho_1\hat{c}_{11}^2(1-\rho_2\hat{c}_{22}) + \rho_2\hat{c}_{01}^2(1+\rho_1\hat{c}_{11}^2)}{(1-\rho_1\hat{c}_{11})(1-\rho_2\hat{c}_{22}) - \rho_1\rho_2\hat{c}_{01}^2} \\
\hat{\gamma}_{11} &= \frac{\rho_2\hat{c}_{22}^2(1-\rho_1\hat{c}_{11}) + \rho_1\hat{c}_{01}^2(1+\rho_2\hat{c}_{22}^2)}{(1-\rho_1\hat{c}_{11})(1-\rho_2\hat{c}_{22}) - \rho_1\rho_2\hat{c}_{01}^2} \\
\hat{\gamma}_{01} &= \hat{c}_{01}\left(\frac{1}{(1-\rho_1\hat{c}_{11})(1-\rho_2\hat{c}_{22}) - \rho_1\rho_2\hat{c}_{01}^2} - 1\right) \\
\hat{\gamma}_{10} &= \hat{\gamma}_{01}.
\end{aligned} \tag{2.7}$$

Since the Ornstein-Zernike-relation(s) only gives a single equation per two functions c and γ, another relation is required to solve for both quantities. The general closure relation is given as follows [46],

$$c(\mathbf{r}) = e^{-\frac{q\phi(\mathbf{r})}{k_B T} + \gamma(\mathbf{r}) + B(\mathbf{r})} - \gamma(\mathbf{r}) - 1, \tag{2.8}$$

where $q\phi(\mathbf{r})$ is the potential energy of Coulomb's potential and B is a bridge function that accounts for very short-ranged correlation effects, that start appearing for coupling strengths $\Gamma > 3-5$. For the calculations in this thesis the bridge function proposed by Ng [47] was used,

$$B(\mathbf{r}) = -1.6\frac{\Gamma}{|\mathbf{r}|/a}\mathrm{Erf}(0.024\Gamma\cdot(|\mathbf{r}|/a)), \tag{2.9}$$

where a denotes the Wigner-Seitz radius. In the so-called hyper netted chain closure, as it was used in the original approach by Baalrud and Daligault [1, 41, 42], the bridge function $B(\mathbf{r})$ is neglected.

For multiple components the closure relation generalizes component-wise,

$$c_{ij}(\mathbf{r}) = e^{-\frac{q\phi(\mathbf{r})}{k_B T} + \gamma_{ij}(\mathbf{r}) + B(\mathbf{r})} - \gamma_{ij}(\mathbf{r}) - 1. \tag{2.10}$$

The Ornstein-Zernike equation together with the hyper netted chain closure relation is a self-consistent system of equations, which allows to compute the correlation functions c and γ. In order to obtain the effective potential, one must use the following general relation,

$$g(\mathbf{r}) = \gamma(\mathbf{r}) + c(\mathbf{r}) + 1 = e^{-\frac{q\phi(\mathbf{r})}{k_B T} + \gamma(\mathbf{r})} = e^{-\frac{e\Phi(\mathbf{r})}{k_B T}}, \tag{2.11}$$

where $\Phi(\mathbf{r})$ is the effective potential and $h(\mathbf{r})$ and $c(\mathbf{r})$ come from the Ornstein-Zernike-relation. The function $g(\mathbf{r})$ is called *pair distribution function* and describes the distribution of inter-particle distances. Taking a fixed particle in the origin $g(\mathbf{r})d^3\mathbf{r}$ gives the probability to find another particle in a volume $[\mathbf{r}, \mathbf{r}+d^3\mathbf{r}]$. Denoting the average density by ρ_0, the radial density around a particle reads,

$$\rho(\mathbf{r}) = \rho_0 g(r) = \rho_0 e^{-\frac{q\phi(\mathbf{r})}{k_B T} + \gamma(\mathbf{r})}. \tag{2.12}$$

Comparing eqns (2.12) and (2.2), one can see that the Yukawa potential is indeed the effective potential if $\gamma(r)$ is negligible, i.e. in the weak coupling limit.

With the method proposed in this chapter, one can obtain an effective potential that accounts for all correlation effects. It self-consistently reproduces Debye-screening in the weak-coupling limit and allows to use the binary collision picture even for strongly coupled electrons.

2.3 Solving the Ornstein-Zernike Equation

The Ornstein-Zernike equation (2.4) or (2.6) together with a closure relation (2.8) or (2.10) presents itself as a self-consistent set of integral equations. It can be directly solved by using an initial guess and subsequently refining it by iteration. Basically, one constructs a sequence of functions $\gamma^{(0)}$, $\gamma^{(1)}$, $\gamma^{(2)}$, ... which will approximate the solution better with every step.

The correlation functions typically share the symmetries of the underlying interaction potential ϕ. In the case of Coulomb interaction, due to spherical symmetry, the correlation functions are dependent on absolute distance $|\mathbf{r}| =: r$ only. For a discrete representation, one can discretize the functions using $r_i := i \cdot \delta r$, which can be noted succinctly as $\gamma_i^{(0)} := \gamma^{(0)}(r_i)$

The entire procedure is summarized in Algorithm 1 and will be laid out in the following. Let us denote the initial guess with $\gamma^{(0)}$, then we can use the closure relation (2.8) to compute the direct correlation function,

$$c_i = e^{-\frac{q\phi_i}{k_B T} + \gamma_i^{(0)} + B_i} - \gamma_i^{(0)} - 1.$$

This result can be used to compute the next function in the sequence $\gamma^{(1)}$ by using the Ornstein-Zernike equation (2.4). In order to circumvent the convolution the problem can be transported into Fourier-Space. For this step the spherical symmetry allows to simplify the Fourier-Integration by setting spherical coordinates up in such a way that the z-axis coincides with $\mathbf{k}$,

$$\begin{aligned}
\hat{c}(k) &= \int d^3\mathbf{r}\ c(r) e^{-i\mathbf{k}\cdot\mathbf{r}} \\
&= 2\pi \int_{-1}^{1} d(\cos\theta) \int_0^\infty dr\ r^2 c(r) e^{-ikr\cos\theta} \\
&= 2\pi \int_0^\infty dr\ r^2 c(r) \frac{1}{-ikr} \left(e^{-ikr} - e^{ikr}\right) \\
&= 4\pi \int_0^\infty c(r) \frac{\sin(kr)}{kr} r^2 dr
\end{aligned} \tag{2.13}$$

Instead of requiring a multidimensional Fourier-Transform, we can use a one-dimensional Fourier-Bessel transform due to radial symmetry. The details of how numerical Fourier-Bessel transforms can be implemented, especially the requirement for regularization functions, are laid out in appendix A.

In Fourier-Space we can then make use of the Fourier-Transformed Ornstein-Zernike equation (2.5) to compute $\hat{\gamma}'^{(0)}$,

$$\hat{\gamma}'^{(0)}(k) = \frac{\rho \hat{c}^2(k)}{1 - \rho \hat{c}(k)}.$$

The distinction between $\gamma'^{(0)}$ and $\gamma^{(1)}$ is made, because it can be beneficial to construct $\gamma^{(1)}$ via a damping procedure from multiple previous solutions. This will be laid out in the next chapter.

The back-transform can be made analogously, which results in $\gamma'^{(0)}$. This gives - without damping - the next member of the sequence $\gamma^{(1)} = \gamma'^{(0)}$. Ideally, the solution is reached after n steps when $\gamma'^{(n)} = \gamma^{(n)}$. In practice one tracks the self-consistency error ε,

$$\varepsilon^{(n)} = \sqrt{\sum_i (\gamma_i'^{(n)} - \gamma_i^{(n)})^2},$$

and stops the computation after a certain precision is achieved.

There are other methods available, which rely on reformulating the problem into e.g. an initial value or root finding problem [44, 45] and solving them with standard methods like Newton-Raphson or implicit Euler, while others use a complete angular integration [48]. These methods tend to have stronger stability but with steeper scaling of the computation cost with the number of grid points, due to matrix operations. For the purpose of this thesis it was found that - given good initial conditions and damping - simple iteration provides a very precise solution with small computation time on reasonably large grids (N>2^{14}).

Algorithm 1 Iteration of the Ornstein-Zernike Equation

Initial Condition $\gamma \leftarrow \gamma^{(0)}$

$\alpha \leftarrow 1/64$ ▷ Damping Factor

$a \leftarrow$ Wigner-Seitz Radius

$\Gamma \leftarrow$ Coupling Parameter

$\phi \leftarrow \frac{e^2}{4\pi\varepsilon_0} r$ Bare Coulomb Potential

K Regularization for ϕ ▷ Described in appendix A

$B \leftarrow -1.6\frac{\Gamma}{r/a}\mathrm{Erf}(0.024\Gamma \cdot (r/a))$ ▷ Ng's Bridge function (2.9)

while Self-Consistent Error $\varepsilon <$ 1e-12 **do**

$c \leftarrow \exp\left(-\left(\frac{q\phi}{k_B T} - K\right) + \gamma + B\right) - \gamma - 1$ ▷ hyper netted chain closure (2.8)

$\hat{c} \leftarrow \mathrm{FBT}[c]$ ▷ Fourier-Bessel transform

$\hat{c} \leftarrow \hat{c} - \hat{K}$

$\hat{\gamma} \leftarrow \frac{\hat{c}}{1-\hat{c}} - \hat{c}$ ▷ via Fourier-Transformed Ornstein-Zernike equation (2.5)

$\hat{\gamma} \leftarrow \hat{\gamma} + \hat{K}$

$\gamma' \leftarrow \mathrm{FBT}^{-1}[\hat{\gamma}]$ ▷ inverse Fourier-Bessel transform

$\varepsilon \leftarrow \mathrm{Norm}[\gamma' - \gamma]$

Compute $\gamma \leftarrow \alpha\gamma' + (1-\alpha)\gamma$ ▷ Obtain new input with damping procedure

2.3.1 Forcing Convergence: Initial Conditions and Damping

Whether an iteration process of an integral equation results in a self-consistent solution is highly dependent on the initial conditions, so the right choice is tantamount for success. The naive choice

of random or constant initial conditions rarely works consistently. Some authors [1, 44] suggest to use the weak coupling limit ($q\phi/k_BT \lll 1$, $\gamma \sim 0$) to expand the exponential in eq (2.8),

$$c_0(r) = -\frac{q\phi(r)}{k_BT}.$$

Others [45, 47] point out that the solutions γ (or c) are point-wise linearly dependent on the coupling constant. One can keep a record of some solutions and then extrapolate an initial condition point by point. Yet another approach is to use the fact that for the Percus-Yevick closure (where eq (2.8) is expanded in γ) with a hard-sphere potential as ϕ, the OZ equation is solvable analytically [49]. This is successful especially for Lennard-Jones potentials [44], which resemble a hard sphere potential due to their rapid decay. For this thesis, the following initial condition was used,

$$\gamma_0 = \mathrm{DST}\left[\frac{q\phi(r)}{k_BT} - \frac{q\phi(r)}{k_BT}\mathrm{Erf}(10r)\right]\frac{\mathrm{Erfc}(0.8r)}{r},$$

where DST[] is a discrete sine transformation. This form has the major advantage of adapting easily to a new grid or denser stepping. Generally, this yields a rapid convergence as long as $\Gamma < 250$, above which an extrapolation can no longer be circumvented.

Even with these methods it can still happen that the iteration converges slowly or not at all. A damping procedure is a way to ameliorate the dependency on the initial conditions and can prevent the iteration from spiralling out of control even for sub-optimal initial conditions. Let us denote the solution after one iteration step before damping as γ'_n, then the simplest form of damping can be set up as follows,

$$\gamma^{(n+1)} = (1-\alpha)\gamma'^{(n)} + \alpha\gamma^{(n)}, \tag{2.14}$$

where α is a damping parameter, than can be adaptive [44] or fixed. If the solution would diverge, i.e. $\varepsilon^{(n)}$ was very large, then the impact of $\gamma_i'^{(n)}$ on the solution $\gamma_i^{(n+1)}$ will be damped by mixing with the previous solution $\gamma^{(n)}$, thus preventing the iteration process from large jumps. Of course, this can be taken arbitrarily far in terms of how many previous solutions are included.

A more elaborate method was proposed by Ng [47] and relies on choosing the damping parameters every step with a scheme that minimizes the self-consistency error of the damped solution. True to Ng's original notation, let us denote an iteration step as an operator,

$$\gamma'^{(n)} = A\gamma^{(n)}$$

and their difference as

$$d^{(n)} = \gamma'^{(n)} - \gamma^{(n)} = (A-1)\gamma^{(n)}.$$

The solution $\gamma^{(n+1)}$ will be damped with the two previous solutions,

$$\gamma^{(n+1)} = (1-\alpha_1-\alpha_2)\gamma^{(n)} + \alpha_1\gamma^{(n-1)} + \alpha_2\gamma^{(n-2)}. \tag{2.15}$$

The main requirement of the method is that the self-consistency error of the damped solution $|A\gamma^{(n+1)} - \gamma^{(n+1)}|$ is minimized. Equivalently, one can minimize the square and obtain the following system of equations,

$$\begin{aligned} \frac{d}{d\alpha_1}\left(A\gamma^{(n+1)} - \gamma^{(n+1)}\right)^2 &= 0, \\ \frac{d}{d\alpha_2}\left(A\gamma^{(n+1)} - \gamma^{(n+1)}\right)^2 &= 0. \end{aligned} \tag{2.16}$$

This is equivalent to the following system,

$$
\begin{aligned}
2(A-1)\left[(1-\alpha_1-\alpha_2)\gamma^{(n)}+\alpha_1\gamma^{(n+1)}+\alpha_2\gamma^{(n-2)}\right](A-1)\left[-\gamma^{(n)}+\gamma^{(n-1)}\right]=0,\\
2(A-1)\left[(1-\alpha_1-\alpha_2)\gamma^{(n)}+\alpha_1\gamma^{(n+1)}+\alpha_2\gamma^{(n-2)}\right](A-1)\left[-\gamma^{(n)}+\gamma^{(n-2)}\right]=0,
\end{aligned}
\tag{2.17}
$$

which can be rewritten as follows,

$$
\begin{aligned}
\left[(1-\alpha_1-\alpha_2)d^{(n)}+\alpha_1 d^{(n+1)}+\alpha_2 d^{(n-2)}\right]\cdot\left[-d^{(n)}+d^{(n-1)}\right]=0,\\
\left[(1-\alpha_1-\alpha_2)d^{(n)}+\alpha_1 d^{(n+1)}+\alpha_2 d^{(n-2)}\right]\cdot\left[-d^{(n)}+d^{(n-2)}\right]=0.
\end{aligned}
\tag{2.18}
$$

Denoting a scalar product between vectors as $a\cdot$b, the system of equations (2.18) can be generally written with the following matrix equation,

$$
\begin{pmatrix}
\left[d^{(n)}-d^{(n-1)}\right]\cdot\left[d^{(n)}-d^{(n-1)}\right] & \left[d^{(n)}-d^{(n-1)}\right]\cdot\left[d^{(n)}-d^{(n-2)}\right] & \cdots\\
\left[d^{(n)}-d^{(n-2)}\right]\cdot\left[d^{(n)}-d^{(n-1)}\right] & \left[d^{(n)}-d^{(n-2)}\right]\cdot\left[d^{(n)}-d^{(n-2)}\right] & \cdots\\
\vdots & \vdots &
\end{pmatrix}
\begin{pmatrix}\alpha_1\\ \alpha_2\\ \vdots\end{pmatrix}
=\begin{pmatrix}
d^{(n)}\cdot\left[d^{(n)}-d^{(n-1)}\right]\\
d^{(n)}\cdot\left[d^{(n)}-d^{(n-2)}\right]\\
\vdots
\end{pmatrix},
$$

which can be solved using standard methods.

Once the coefficients $\alpha_1, \alpha_2, ...$ are obtained they can be used for damping. According to Ng [47] the damped solution must be composed of solutions γ' after the iteration step. This means the solution $\gamma^{(n+1)}$ looks as follows,

$$
\gamma^{(n+1)}=(1-\alpha_1-\alpha_2)\gamma'^{(n)}+\alpha_1\gamma'^{(n-1)}+\alpha_2\gamma'^{(n-2)}.
$$

The obvious requirement of this method is, that we have previous solutions γ' accessible, before we can start the damping. Consequentially, if the damping is of order m, the first m iteration steps cannot be damped,

$$
\begin{aligned}
\gamma^{(1)}&=\gamma'^{(1)}\\
\vdots\quad&\quad\vdots\\
\gamma^{(m)}&=\gamma'^{(m)}.
\end{aligned}
$$

While in most cases, damping accelerates the convergence by a large margin, it can happen that the divergence starts already within those first n steps required. Usually, the solution can still be obtained by using simple damping (2.14) for the first steps or modifying the initial conditions.

Another way [46] to achieve convergence in difficult cases is by solving the system at lower coupling than intended. This solution is then used as an initial condition to solve a case with slightly higher coupling, which is itself used as the initial condition for even higher coupling. In other words, one slowly approaches the desired regime by gradually increasing the coupling strength and reusing the previous solution each step as an initial condition.

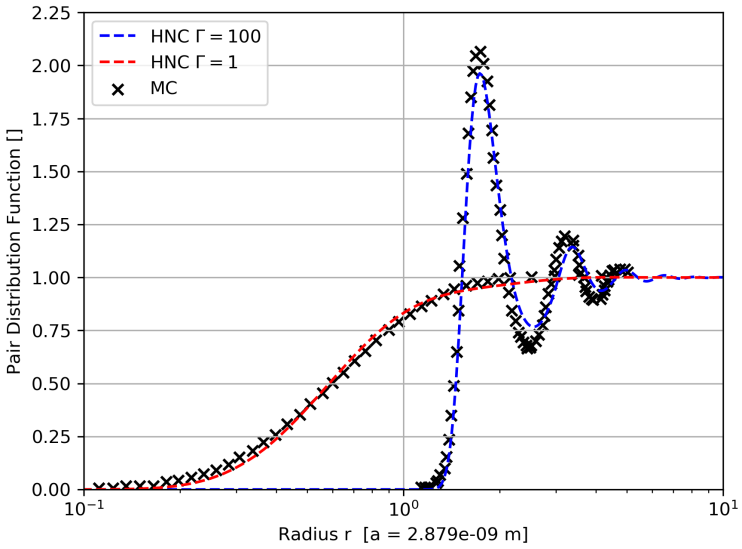

Figure 2.2: Comparison between the Ornstein-Zernike solver with hyper netted chain closure (HNC) with Monte-Carlo (MC) data from [41] for coupling values $\Gamma = 1, 100$.

2.3.2 Comparison with Literature

For verification purposes, the solution procedure for the Ornstein-Zernike equation was checked against MC data provided by Baalrud and Daligault [41], which can be seen in figure 2.2. It is obvious that the solver lies in good accordance to the expected values.
At this point it must be noted, that the original publication did not include the bridge term (2.9), which means in the higher coupling regime, their solver did not reproduce the peak heights to the accuracy possible. For comparison, the original figure from [41] is shown in figure 2.3.

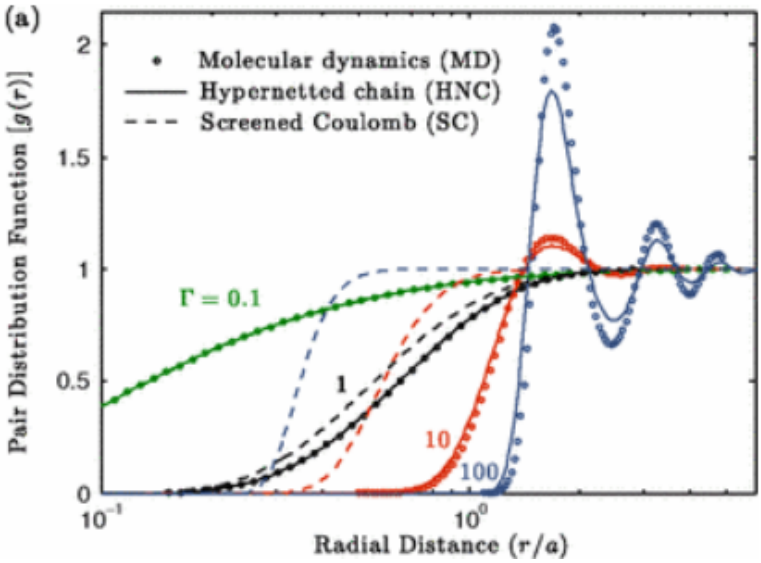

Figure 2.3: Graph from [41]

Another way to test for physical validity is to check the weak coupling limit. Under the absence of correlation effects the effective potential is expected to be the Debye potential (2.3). Assuming this we can neglect γ in eq (2.11) and the pair distribution function takes the form,

$$g_Y(r) = e^{-\frac{e\phi_Y(r)}{k_B T}}. \tag{2.19}$$

A comparison between eq (2.19) with the numerical solution can be seen in figure 2.4. It is noteworthy that the solution interval is quite large compared to the cases with stronger coupling (e.g. figure 2.7). In this limit the Debye length is approximately $\lambda_D \approx 6.9 \cdot 10^{-8}$ m and the interaction is comparatively long ranged. Consequentially, the solution had to be obtained on a grid with 2^{14} points.

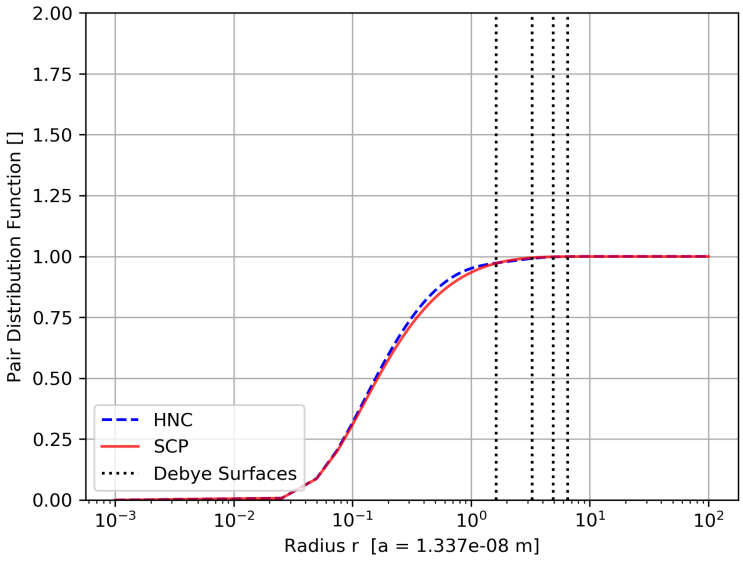

Figure 2.4: Pair Distribution function in the weak coupling limit with ρ =1e17 cm^{-3}, $T = 50$ K. The pair distribution function of the Ornstein-Zernike solver (HNC) is in good agreement with the pair distribution function corresponding to Yukawa's potential (SCP).

In the same spirit one can compare the effective potential with the Debye-screened potential, which is done in figure 2.5. One can see that towards the end of the interval there are deviations, which are due to the fact, that the effective potential eventually reaches zero, as opposed to the hyperbolic Yukawa potential. This happens due to the logarithm involved, as the same behaviour can be produced by evaluating $-\log(\exp(-\phi_Y/(k_B T)))$ numerically. This is an inevitable finite size effect stemming from numerical limitations.

2.3.3 Possible Reasons for Failure

The iteration spirals out of control when γ reaches high values. In the hyper netted chain equation (2.8) the exponential causes a numerical singularity, which cannot be damped away. In the one-component case this can only happen, if the initial conditions are chosen badly for the regime one wishes to solve the equations in. The computations for this thesis are stable and fast for about $\Gamma < 250$ but it is possible to solve them up to $\Gamma = 7000$ as it was done by Ng [47].

The multi-component case is more unstable in this respect as there are interactions in between different components. A typical case of a numerical singularity in a multi-component calculation

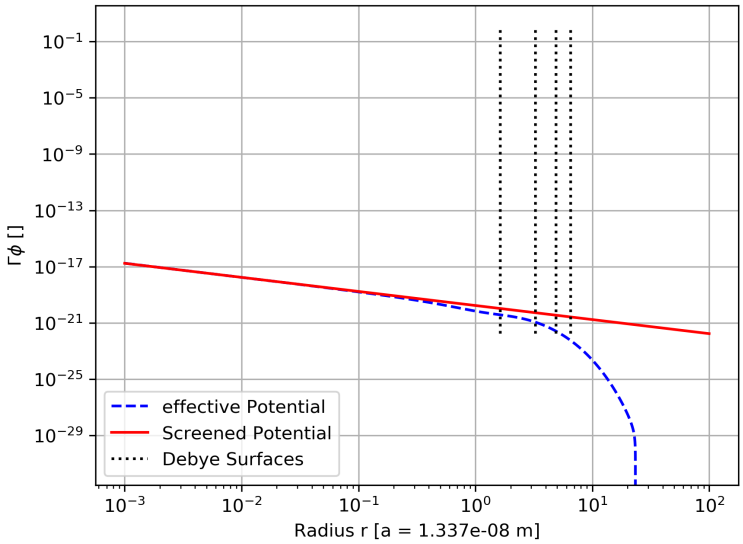

Figure 2.5: Effective potential in comparison with the Debye potential, corresponding to figure 2.4.

is shown in figure 2.6.

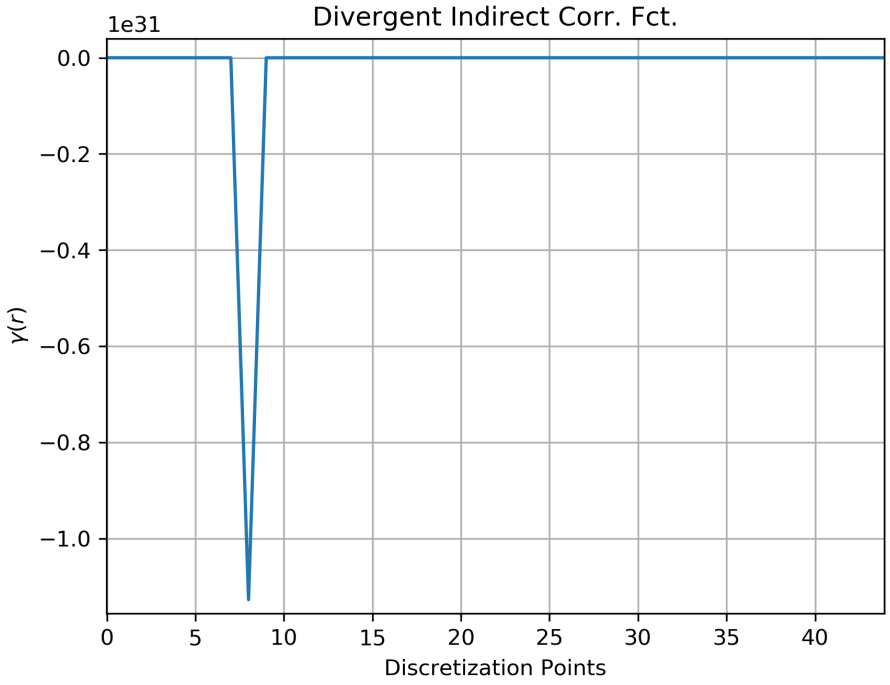

Figure 2.6: Numerical Singularity in a two-component calculation, which occurred in γ_{12}.

It seems that the interactions between different components cause the problem, as the two-component correlation functions γ_{12}, γ_{21} diverge before the others γ_{11}, γ_{22}. Since they are connected, as can be seen from the multi-component hyper netted chain closure (2.10), the calculation

quickly diverges. Apart from the above techniques there are currently no ways to salvage the computation, if it diverges at this point.

2.3.4 Numerical Effective Potential

The numerical solution of the integral equations is inevitably discrete and therefore all quantities are given only on a set of points over a restricted interval. An example to showcase the problem can be seen in figure 2.7. Of course it would be desirable, that the effective potential we obtain in the process was continuous and could be evaluated beyond a finite interval.

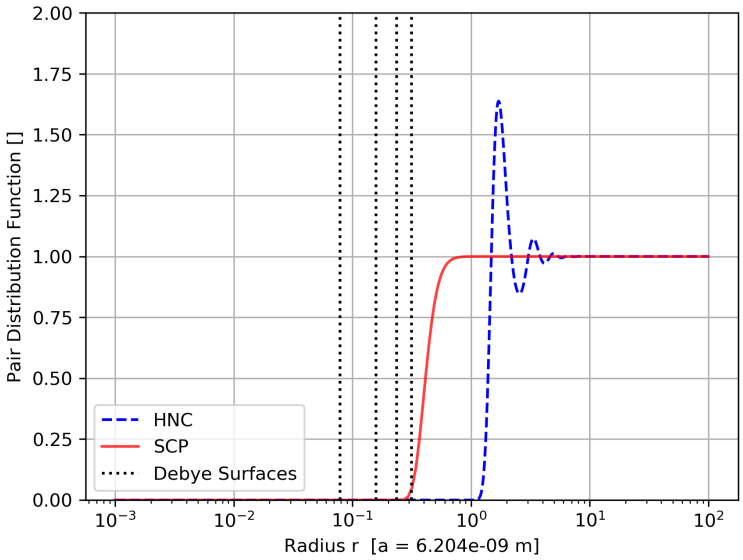

Figure 2.7: Radial pair distribution function for a plasma with density 1e18 cm^{-3} and temperature 50 K. These parameters are typical for ultracold sources.

Based on the general shape of a pair distribution function in figure 2.7, we can assume that the effective potential is still divergent for small radii and that it effectively vanishes for large enough radii. However, the concrete form, i.e. how strong the divergence and the decay are, cannot be read from the graph. At this point it is useful to recall eq (2.11) in the following form,

$$e\Phi = -\log(g)k_BT = e\phi - \gamma(r)k_BT.$$

Since correlation functions, such as $c(r)$ and $\gamma(r)$, are typically zero in the origin and short-ranged, we can expect that the effective potential does not deviate from the original potential ϕ outside of the interval of solution. Hence, we can assume the same functional form and fit a function similar to ϕ to the data.

Numerically, there are two caveats to this procedure. Firstly, the pair distribution function $g(r)$ will be effectively zero on the lower end of the interval (see figure 2.7), which causes infinities in the logarithm that need to be smoothed over. Secondly, for good accuracy the fitting procedure should only take into account the upper portion of the potential, before the oscillations take on. Both these points need to be considered by only taking the logarithm at non-zero values of g and using only the first $\sim 15\%$ of the points for the fit, depending on the potential at hand. The result of such a procedure can be seen in figure 2.8.

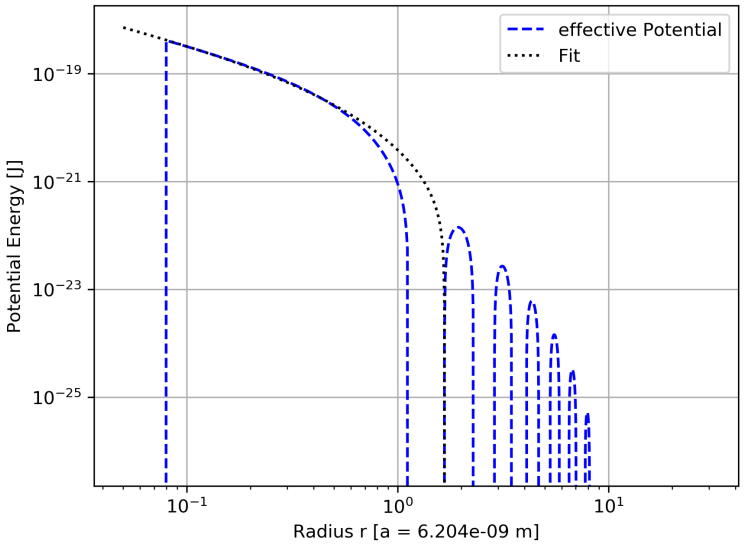

Figure 2.8: Effective Potential evaluated discretely and with the fit, corresponding to figure 2.7.

For radii larger than the evaluation interval, we can assume the potential to vanish. The transition to zero is guaranteed to be smooth, because the oscillation amplitude decreases gradually. The result of the entire procedure can be seen in figure 2.9.

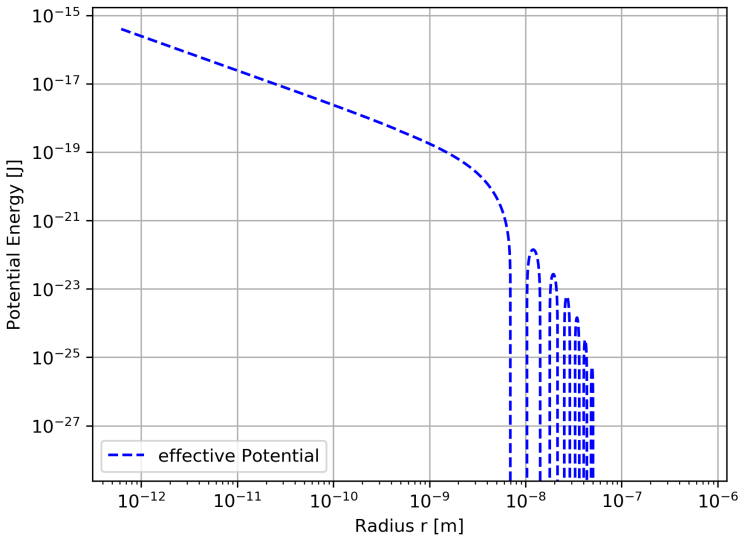

Figure 2.9: Effective Potential as in figure 2.8 including the continuation.

Another point wort mentioning is that the effective potential has an obvious screening length that may deviate from the Debye length, depending on the coupling strength. The effective screening length can be estimated by demanding the pair distribution function (see e.g. figure 2.7) to be 1 within some tolerance. Due to the oscillations we must look for the farthest away point, where the function leaves the tolerance. An example code can be seen in listing 2.1.

Listing 2.1: Effective Screening Length

```
n = len(g)
idx = np.zeros(n, dtype=bool)

for i in range(n):
   if(1.-1e-3 < g[n-i-1] < 1.+1e-3):
      idx[n-i-1] = True
   else:
      idx[n-i-1] = False

effscreen = r[idx][0]
```

Chapter 3

Inclusion of Quantum Effects

While there are some ways to properly account for correlation effects in the strong coupling regime, they are without exception purely classical. The Ornstein-Zernike equation, or direct schemes like P^3M, can only account for classical correlation effects. As pointed out by Claessens *et al.* [10], it is to be expected that ultra-cold sources potentially produce quantum degenerate electron bunches. In the following part, it will be elaborated what can be done to take quantum effects into consideration, and how far into the ultra-cold limit a purely classical approach can go.

While quantum kinetic theory is a sufficiently developed field [50], the study of quantum mechanical effects has largely been focused on either a fluid-like description with quantum magneto-hydrodynamics [51–60] or (comparatively) high temperature plasmas [34, 61–66], most notable among which are the quantum Landau [34] and quantum Langevin [67] approach. Overall, it is not entirely clear which quantum effects will become relevant in the ultracold regime. For example, one can say for certain, that Pauli repulsion will factor into the dynamics, but not, whether other effects, such as e.g. Alfven or Bohm-de-Broglie effects [59], must be considered as well.

For a particle accelerator simulation, the desired outcome is a model that dynamically computes particle positions and velocities under the influence of external fields. In this sense the most promising candidate for a first-principles quantum mechanical model is time-dependent density functional theory. However, the method seems to struggle to accurately describe strongly correlated electrons [68], which are inevitable in the ultracold limit.

The algorithm proposed by Dauger [69] is a semi-classical alternative, that incorporates elements of the wave-nature of electrons into the calculation, while retaining the basic PIC-scheme. In order to be of use for the modelling of collisions, one would need to extend the idea into a P^3M based scheme, where it remains unclear, how the continuous short-ranged part would be incorporated.

A quantum-mechanical extension to the effective potential theory is provided by the *classical-map hyper netted chain algorithm*, which was proposed by Dharma-Wardana and Perrot [70]. The approach is conceptually rooted in density functional theory and applies the ordinary Ornstein-Zernike procedure. The idea is to represent a quantum system by modelling a classical system in a special way. The original procedure is augmented in two ways:

- The one-component electron gas is considered as a homogeneous mixture of two components with equal density, which represent two types of spins. The interaction between particles with different spins contains Pauli repulsion in addition to classical electromagnetic interaction.
- The ("classical fluid") temperature of the mixture is $T_{\mathrm{cf}} = \sqrt{T^2 + T_q^2}$, where T is the physical temperature and T_q is a "quantum" temperature. The reasoning is that, opposite to their

classical pendant, quantum systems have non-vanishing zero-point energy. Hence, if we model the quantum case with a classical system, we need to map the temperature, such that at $T = 0$ it is non-zero $T_{\mathrm{cf}} = T_q > 0$. The quantum temperature T_q is obtained by making fits to MC data. For this thesis, the form of Bredow [46] was used,

$$k_B T_q = \frac{E_F}{1.594 - 0.316\sqrt{a}}, \tag{3.1}$$

where a is the Wigner-Seitz radius and E_F is the Fermi energy.

Usually, these calculations are done for plasma with high density $> 1e20$ cm^{-3} and relatively high temperatures > 4000 K [71]. In the parameter region of interest for this thesis, it was found that the two-component calculation is unstable and does not converge. Ignoring numerical considerations for a moment, Bredow [46] suggests that the instability could alternatively be interpreted physically. In other words the core assumptions of thermal equilibrium and homogeneous mixture are no longer viable in the quantum regime. It could be, that the configuration of two mixed spin populations is unphysical and we have to expect them to separate. Notwithstanding, there is not enough data on spin distributions in strongly coupled plasmas to make such a claim confidently.

Another approximate way to include quantum mechanical effects into the effective potential is via pseudo-potentials. The most common examples include the potential by Kelbg [72] and the (various) Deutsch potentials [71, 73], which account for different features via statistical approximations. One version of the Deutsch potential used by Bredow *et al.* [74] for a one-component electron plasma reads as follows,

$$\phi_D(r) = k_C \frac{1}{r}\left(1 - e^{-\frac{r}{\lambda_T}}\right) + k_B T \log(2) e^{-\frac{\log(2)}{\pi}\left(\frac{r}{\lambda_T}\right)^2}, \tag{3.2}$$

where $\lambda_T = \frac{\hbar}{m k_B T}$ is the thermal de-Broglie wavelength. The first term is a diffraction-correction, which accounts for the fact, that the position of the electron is uncertain on the scale of the thermal wavelength and the second term accounts for Pauli repulsion.

Unfortunately, the derivations of these pseudo-potentials involve approximations that are hard to justify if the temperatures are very low. The most prominent example is the assumption of the Slater determinant for the electron wave function. Since they fail to reproduce the appropriate peak heights in relatively cold plasma, as shown by Bredow *et al.* [71], it must be assumed that they lose validity in the ultracold limit.

In conclusion neither does a full first-principles quantum approach exist nor is there an obvious extension to the semi-classical effective potential approach. In general there seems to be no straightforward way to construct a collision model that properly accounts for quantum influences.

Chapter 4

Estimating the Significance of Pauli Repulsion

Ultracold plasmas experience both correlations as well as quantum mechanical effects. Results by Issanova *et al.* [75] show that for $\Gamma \to 1$ quantum diffraction and screening start to compensate each other. Whether these results generalize to configurations with stronger couplings stands to question, but it has to be assumed that both effects appear and possibly interact and influence each other.

As the previous chapter details there is no straight-forward way to extend commonly used computation schemes into the quantum domain. Since a fully quantum simulation is out of question for now as well, there seems little that can be done. For the sake of practicality an estimate of the importance of Pauli repulsion will be given, which allows to gauge the applicability of classical collision modelling schemes for certain ultracold sources.

Instead of the "fully" quantum approach, we can modify the classical effective Potential Φ from eq (2.11) directly with Pauli repulsion P,

$$\Phi \to \Phi + P.$$

Through a comparison between two cross sections, once with P added (corresponding to a collision with parallel spins) and once without (antiparallel spins) we can still get an idea of the importance of quantum effects, while also considering (strictly classical) correlations. The reasoning is that in the classical limit, the spins of two colliding electrons do not factor into the collisions. Correspondingly, if their difference is significant, Pauli repulsion may not be neglected.

In order to motivate, why the classical collision cross section is a reasonable measure, one can for example consider the Boltzmann collision operator in angular form (5.3),

$$\left(\frac{\partial f}{\partial t}\right)_{\text{coll}} = \int d^3\mathbf{v}'_a \int d^3\mathbf{v}'_b \int d^3\mathbf{v}_b \; |\mathbf{v}_b - \mathbf{v}_a| \boxed{\frac{d\sigma}{d\Omega}} \left[f(\mathbf{v}'_a) f(\mathbf{v}'_b) - f(\mathbf{v}_a) f(\mathbf{v}_b)\right],$$

where the cross section directly appears. As shown by Baalrud and Daligault [41], calculations based on this operator while using an effective potential, hold even into the strong coupling regime. Furthermore, for the purpose of this thesis, the idea is to get an idea on the applicability of classical schemes rather than an exact quantification.

4.1 Procedure

The first step is to compute the effective interaction potential by numerically solving the Ornstein-Zernike equation, as detailed in section 2.3. For a one-component plasma, this involves the iteration of the eqns (2.4), (2.8),

$$\gamma(r) = \rho \int d^3\mathbf{s}\; c(|\mathbf{r}-\mathbf{s}|)h(s),$$
$$c(r) = e^{-\frac{q\phi}{k_B T}+\gamma(r)+B(r)} - \gamma(r) - 1,$$

from which the effective potential Φ can be computed through relation (2.11),

$$g(r) = \gamma(r) + c(r) + 1 = e^{-\frac{q\phi}{k_B T}+\gamma(r)} = e^{-\frac{e\Phi}{k_B T}}. \tag{4.1}$$

In order to account for Fermi degeneracy, the Pauli potential is computed according the scheme outlined by Dharma-Wardana and Perrot [70], which is summarized in appendix B.

Let us denote the classical scattering angle by θ and the impact parameter by b, then the classical cross section is given through the following,

$$\frac{d\sigma}{d\Omega}(\theta, E) = \frac{b}{\sin\theta}\left|\left(\frac{d\theta}{db}\right)^{-1}\right|. \tag{4.2}$$

The derivative can be evaluated, using relation,

$$\theta = \pi - 2\int_{r_{\min}}^{\infty} \frac{b}{r^2\sqrt{1-\frac{\phi(r)}{E}-\frac{b^2}{r^2}}}dr, \tag{4.3}$$

where $r_{\min}$ is the root of the perihelion equation,

$$1 = \frac{\phi(r_{\min})}{E} + \frac{b^2}{r_{\min}^2}. \tag{4.4}$$

A detailed derivation of eqns (4.2), (4.3) and (4.4) and a procedure for their numerical solution can be found in appendix D. One noteworthy peculiarity is that whenever the potential vanishes, the cross section will diverge. From e.g. figure 2.9 it is clear that an effective potential oscillates and decays, so we expect the cross section to diverge accordingly.

The issue when comparing cross sections with each other is that they might not be evaluated at the same angles, since the relation (D.2) depends greatly on the form of the potential. This problem is further intensified by the oscillating behaviour. In order to not solely rely on eyesight for comparison, the following measure will be used to compare the cross sections $\frac{d\sigma_1}{d\Omega}$ and $\frac{d\sigma_2}{d\Omega}$ with each other,

$$\Delta = \frac{\sqrt{\frac{1}{N}\sum_i \left(\frac{d\sigma_1}{d\Omega}(\theta_i) - \frac{d\sigma_2}{d\Omega}(\theta_i)\right)^2}}{\sqrt{\frac{1}{N}\sum_i \left(\frac{d\sigma_1}{d\Omega}(\theta_i)\right)^2}} \cdot 100. \tag{4.5}$$

The idea is to interpolate the cross sections and evaluate the quadratic difference between them for N samples. For scaling it is normalized to percentages of one of the results. This method is not perfect as it is prone to errors due to interpolation but still gives an idea of the qualitative behaviour.

The entire calculation involves a lot of different numerical procedures, among which are integration, interpolation, differentiation, iteration and others. All of those steps introduce random deviations

which propagate and possibly influence each other, therefore it is impossible to track each and every error. For the purpose of estimation, one can compute the same result multiple times and measure the deviation between samples with the measure introduced previously eq (4.5). For 2048 sample points in the OZ-solver, 1000 points in the cross section solver and 100 sample calculations, the (normalized) deviation is below 1e-11% of the largest result. The only error of the same order comes from the numerical integration of the classical scattering integral (4.3), which can hardly be improved.

4.2 Results

Figures 4.2 - 4.6 show the cross sections for increasing coupling parameter. Figure 4.1 shows the overall behaviour of the difference in cross section as a function of temperature for various densities.

One can observe that the weak coupling limit reproduces the Rutherford cross section, as was to be expected. The rise of correlation effects can be observed in the spikes that occur for stronger coupling, which reflect the oscillations in the effective potential. The results show that the appearance of exchange interaction is predominantly affecting the large-angle portion of the cross section. This was to be expected as the Pauli potential is short-ranged and collisions with small impact parameters correspond to larger scattering angles. From the cross sections and especially from figure 4.1 we see, that Pauli repulsion may be neglected over a large temperature range as long as the density is below $1e19$ cm^{-3}. The non-zero values for the $1e17$ cm^{-3} contour are likely due to interpolation errors, to which the measure (4.5) is prone to. Firstly, this means that the line $\Theta = 1$ (where Θ is the degeneracy parameter) in configuration space is to be understood as a hard limit. Secondly, this also shows that a classical picture suffices for state-of-the art sources.

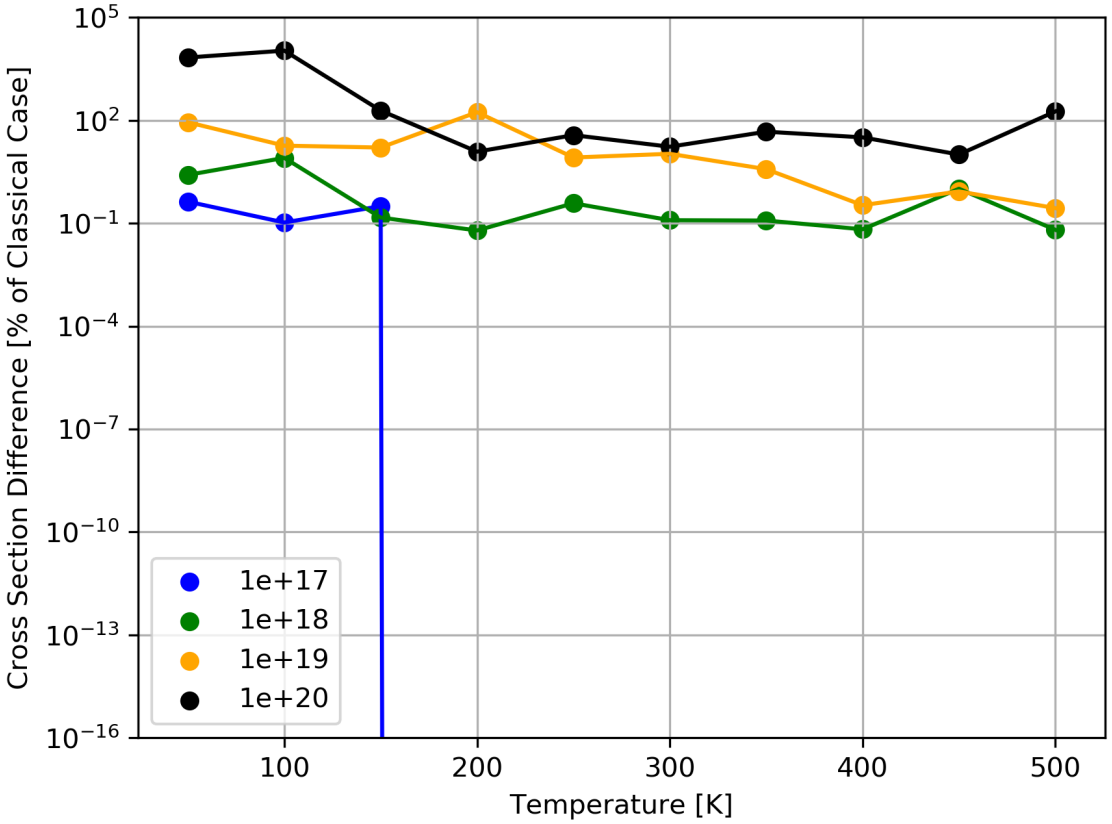

Figure 4.1: Estimated overall difference in cross section (calculated as in eq (4.5)) for various densities in cm^3.

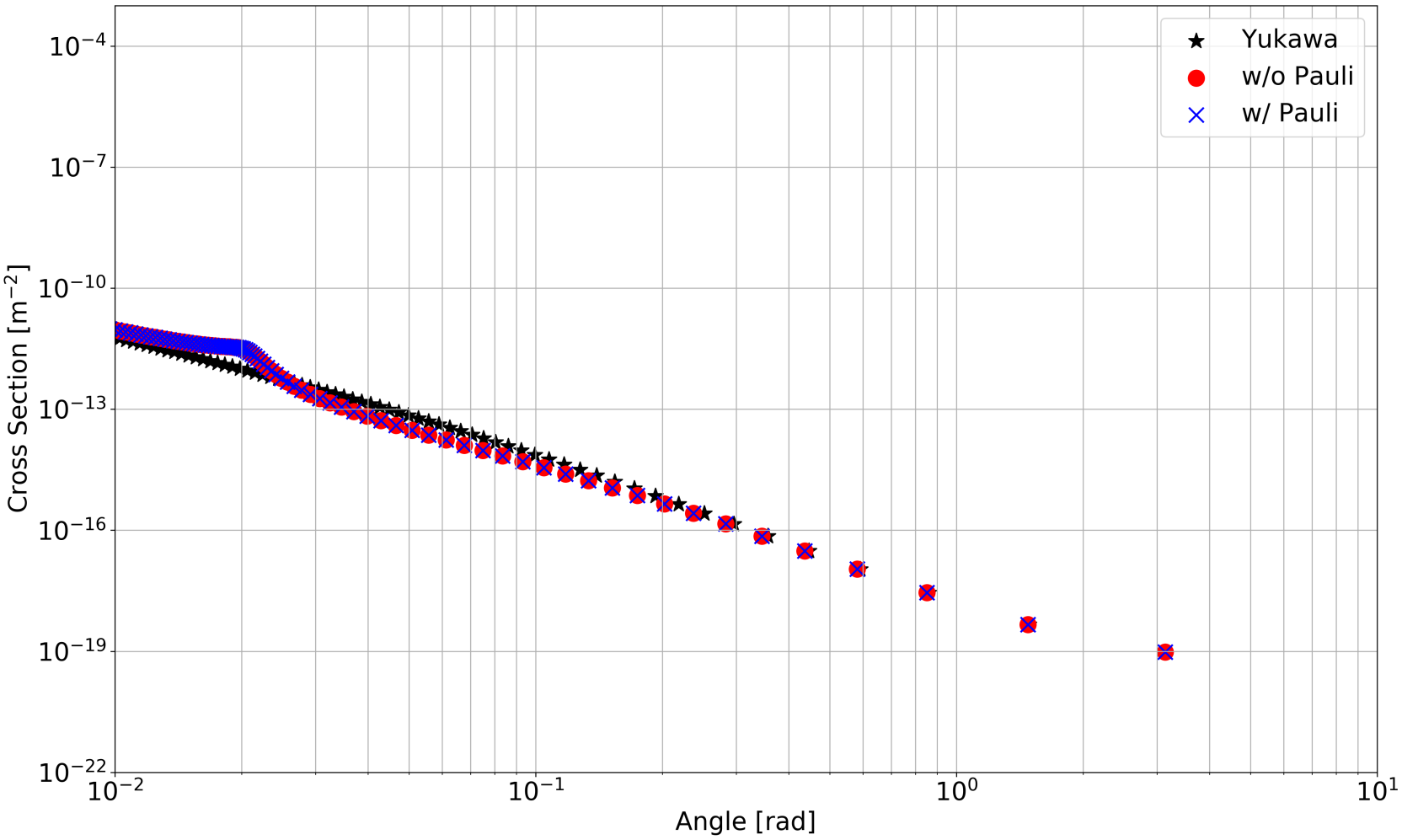

Figure 4.2: Comparison between cross section for collisions with parallel (blue, crossed) and anti-parallel spins (red, dotted). The configuration parameters are $\rho = 1e17$ cm^{-3}, $T = 1e4$ K.

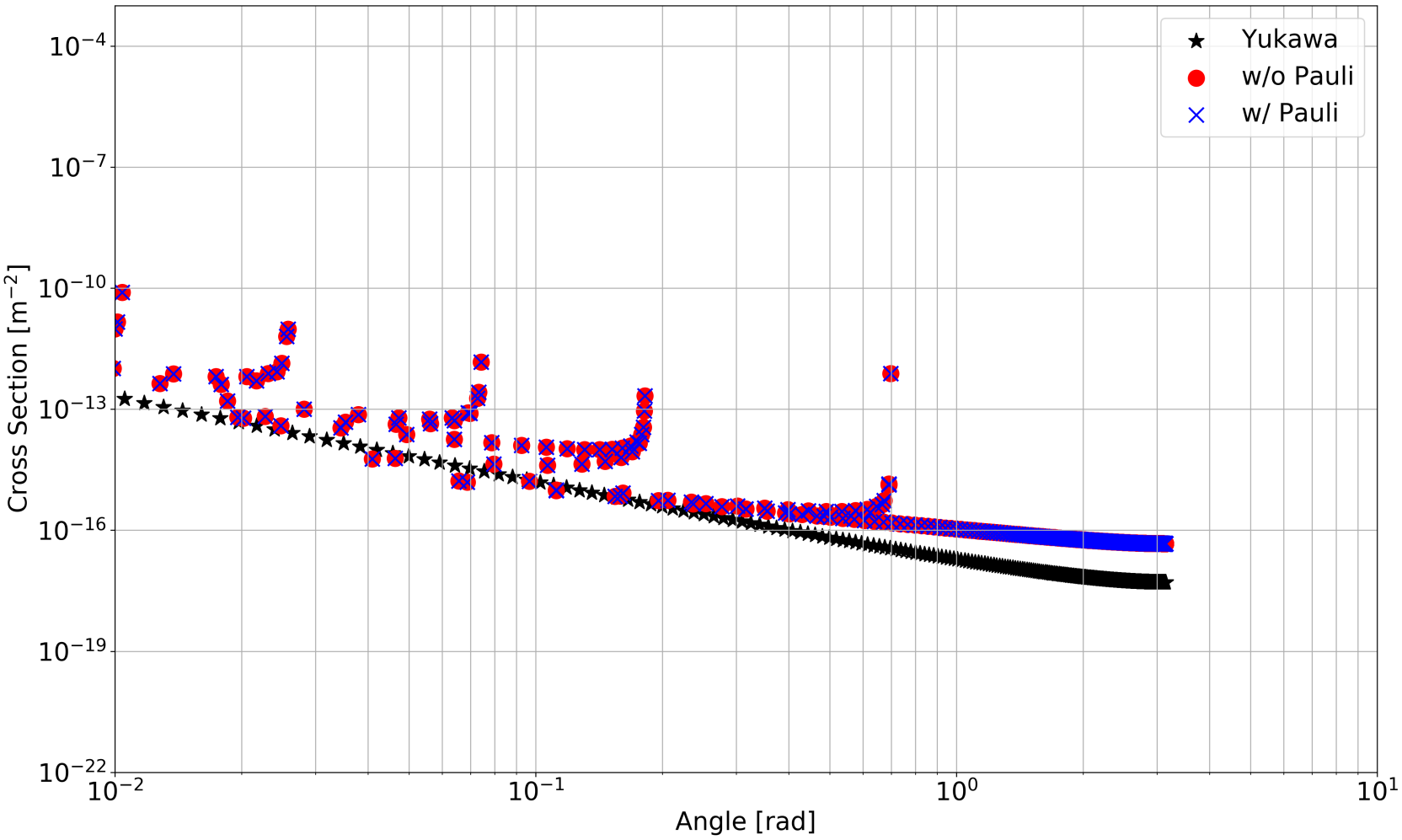

Figure 4.3: Comparison between cross section for collisions with parallel (blue, crossed) and anti-parallel spins (red, dotted). The configuration parameters are $\rho = 1e17$ cm^{-3}, $T = 50$ K.

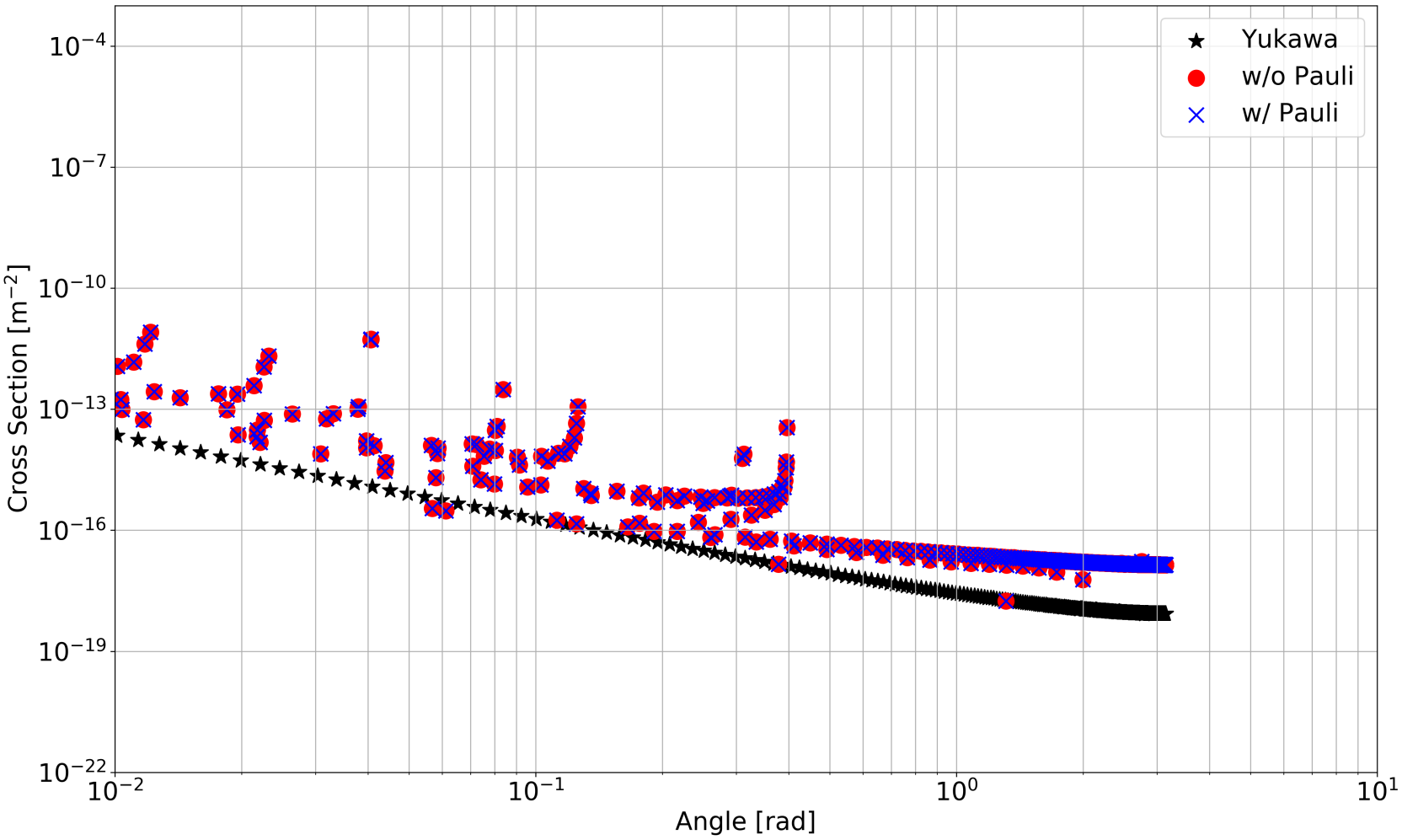

Figure 4.4: Comparison between cross section for collisions with parallel (blue, crossed) and anti-parallel spins (red, dotted). The configuration parameters are $\rho = 1e18$ cm^{-3}, $T = 50$ K.

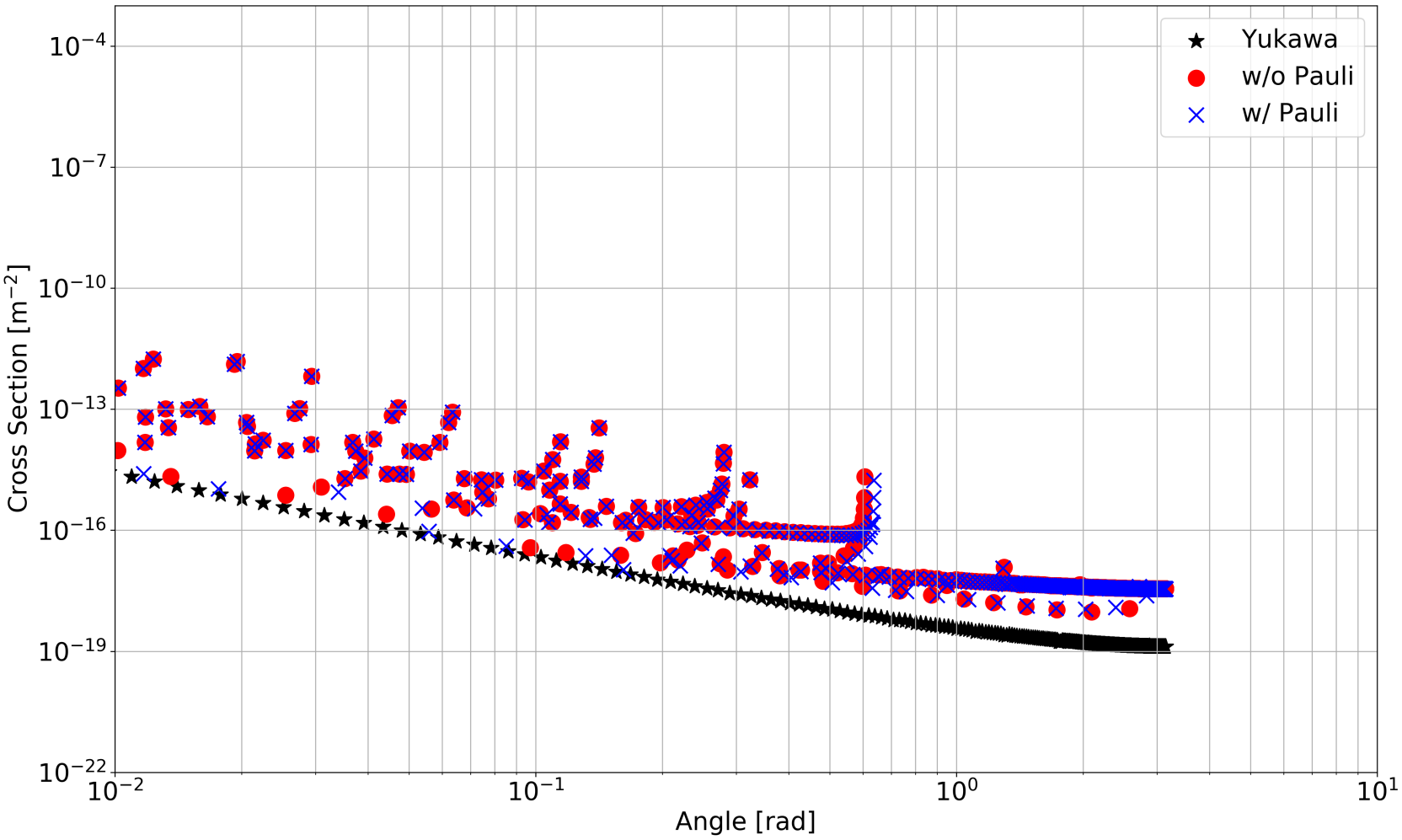

Figure 4.5: Comparison between cross section for collisions with parallel (blue, crossed) and anti-parallel spins (red, dotted). The configuration parameters are $\rho = 1e19$ cm^{-3}, $T = 50$ K.

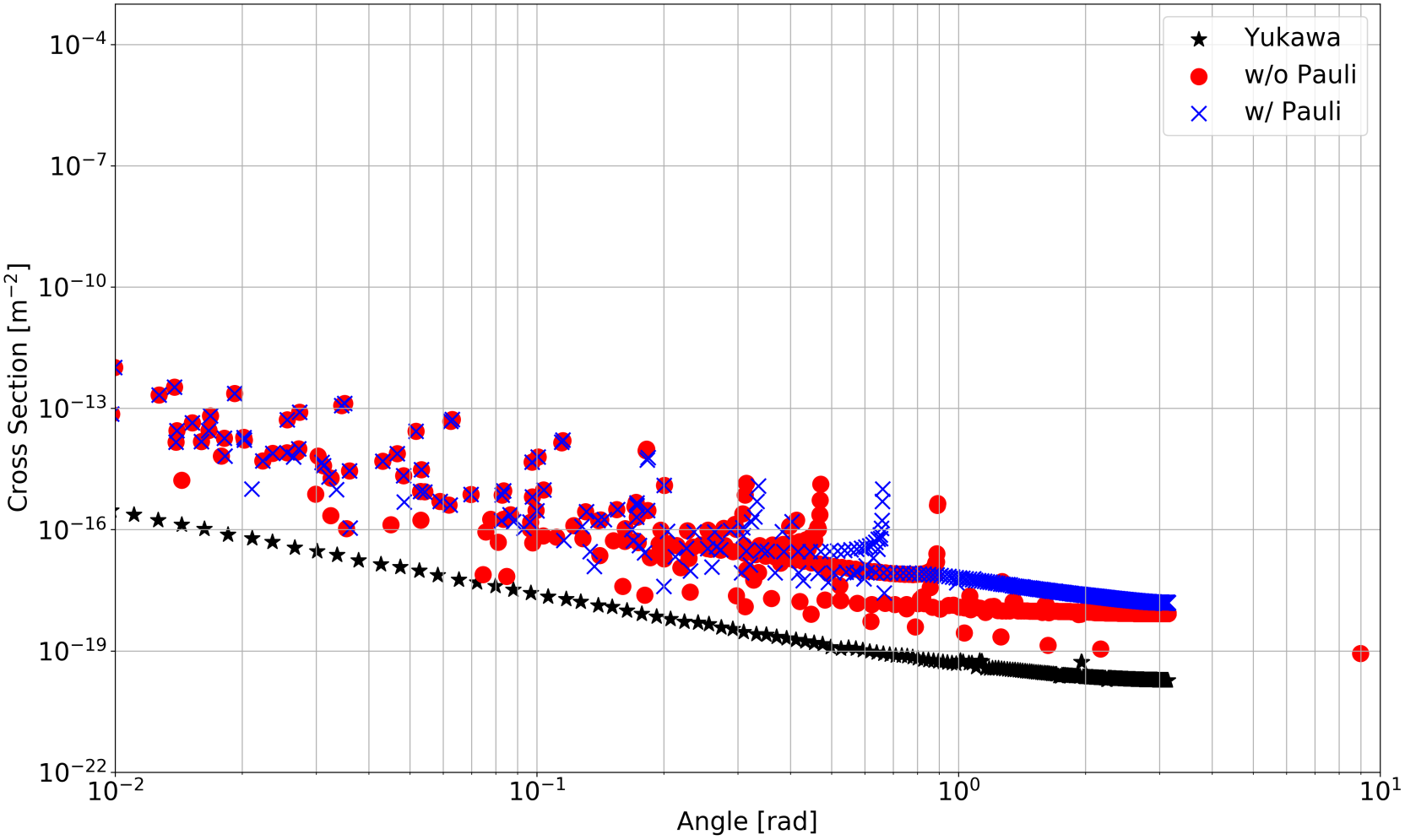

Figure 4.6: Comparison between cross section for collisions with parallel (blue, crossed) and anti-parallel spins (red, dotted). The configuration parameters are $\rho = 1e20$ cm^{-3}, $T = 50$ K.

Part II

Review of Approaches to Collision Modelling

Since this part is heavy in mathematical notation, a glossary of the commonly used symbols is provided in table 4.1. Sparsely used notation is introduced when needed.

Table 4.1: Collection of mathematical symbols used in chapter 6.

Symbol	Meaning
$\mathbf{x}_1$	3-dim vector of initial spatial conditions
$\mathbf{v}_1$	3-dim vector of initial velocity conditions
f	Probability density function in 6-dim phase space
f_0	Initial probability density function
$\mathbf{x}(\mathbf{x}_1, \mathbf{v}_1, t)$, $\mathbf{v}(\mathbf{x}_1, \mathbf{v}_1, t)$	Position and velocity of a point in phase space as a function of initial conditions and time.
$\boldsymbol{\xi}_\alpha$	3-dim position vector of (macro-)particle α
$\boldsymbol{\xi}_\alpha^n$	3-dim position vector of (macro-)particle α at time $n\Delta t$
$\{\boldsymbol{\xi}_\alpha\}$	Set of 3-dim position vectors of all (macro-)particles
$\dot{\boldsymbol{\xi}}_\alpha$	3-dim velocity vector of (macro-)particle α
$\{\dot{\boldsymbol{\xi}}_\alpha\}$	Set of 3-dim velocity vectors of all (macro-)particles
ω_α	Weight of (macro-)particle α, i.e. the number of physical particles that α contains
ϕ	Electric potential
ρ	Charge density function. Corresponds to spatial part of the probability density function.
$\mathcal{L}$	Lagrangian
S_x	Spatial shape function, e.g. B-spline of order 0
S_v	Velocity shape function, e.g. δ-function
∇_x	3-dim spatial derivative of first order
Δ, ∇_x^2	3-dim spatial derivative of second order
∇_v	3-dim velocity derivative of first order
N_x, N_y, N_z	Number of grid points in different spatial directions
h_x, h_y, h_z, Δt	Grid stepping in different spatial directions and time
D_x	Finite difference operator of second order in x-direction
D_{xyz}	Discrete Laplacian operator
$W(\mathbf{x}_i - \boldsymbol{\xi}_\alpha)$	Interpolation function, i.e. the amount of charge that particle α contributes to grid point i.
$\mathcal{L}_d(..., \Delta t)$	Lagrangian averaged over span of time Δt
$\otimes$	Convolution between two continuous functions
$\otimes_d$	Discrete convolution of two finite sets
γ	Charge smearing function
ϕ^S, $\phi_{\rho-\rho\otimes\gamma}$	Potential corresponding to the Poisson equation $\varepsilon_0\Delta\phi_{\rho-\rho\otimes\gamma} = \rho - \rho\otimes\gamma$
ϕ^S, $\phi_{\rho\otimes\gamma}$	Potential corresponding to the Poisson equation $\varepsilon_0\Delta\phi_{\rho\otimes\gamma} = \rho\otimes\gamma$
W^S	The screened charge distribution $\rho - \rho\otimes\gamma$, dubbed the short-ranged interpolation function for consistency reasons alone, as there are no interpolation steps involved.
W^L	Interpolation function for the charge distribution $\rho\otimes\gamma$
$\mathcal{L}_f^L$, $\mathcal{L}_{\text{int}}^L$	Field energy and interaction term of the Lagrangian for the potential ϕ^L
$\mathcal{L}_f^S$, $\mathcal{L}_{\text{int}}^S$	Field energy and interaction term of the Lagrangian for the potential ϕ^S
$(\rho^L)_k^n$	Discretized charge distribution $\rho\otimes\gamma$ at grid point k and time n
$(\rho^S)^n(\mathbf{x})$	Continuous charge distribution $\rho - \rho\otimes\gamma$ at position $\mathbf{x}$ and time n
G^S	Green's function to the Poisson equation $\varepsilon_0\Delta\phi^S = \rho^S$
G^L	Discrete Green's function to the discrete version (6.20b) of the following Poisson equation: $\varepsilon_0\Delta\phi^L = \rho^L$

G^C	Correction function to Green's function, which is added to enforce Dirichlet boundary conditions
G^F	The "free" Green's function $G^F(r) = \frac{1}{r}$
$S(x, y, z)$	Symmetry map that gives the mirror image of the position vector (x,y,z)
$\mathbf{x}$, $\mathbf{y}$	Position vectors
R	Analytical Green's function that gives the correct boundary conditions for an arbitrary geometry
Φ	True potential, corresponds to $\Phi = R \otimes \rho$
Φ^S	True short-ranged potential, corresponds to $\Phi^S = R \otimes \rho^S$
ϕ^{tot}	Potential as computed via P^3M algorithm
E	Total integrated error committed by P^3M algorithm
$\tilde{\phi}^L(\mathbf{x})$	Continuous form of $(\phi^L)_k$
$\mathbf{m}, \mathbf{k}$	Discrete reciprocal grid vector and continuous Fourier space variable respectively
$\mathbf{n}$	Vector of integers $\mathbf{n} \in \mathbb{N}^3$

Chapter 5

Kinetic Description of Collision Dynamics

Fundamentally, a kinetic description relies on simplifying Liouville's equation to a solvable form. Over the course of the following chapter, the basis for Boltzmann's and Landau's equation will be motivated and their assumptions investigated. It will be made clear, which conditions must be fulfilled for these approximations to be useful and whether or not this is the case for ultra-cold sources.

5.1 Base Equations

The first step of a kinetic description is to build a phase space. Therein lies the fundamental difference between Liouville's and Klimontovich's equation. In the following a quick outline of the differences between them will be given, which roughly follows [28].

5.1.1 Klimontovich

As mentioned above, an exact description of the dynamics of a set of charged particles is given by solving Newton's equations for each particle individually. The system of equations can be compactly expressed by using a density function f in 6D phase space $(\mathbf{x}, \mathbf{v})$, where each particle corresponds to a point. Denoting the position of particle α as $\boldsymbol{\xi}_\alpha$, the distribution function reads,

$$f(\mathbf{x}, \mathbf{v}) = \sum_{\alpha=1}^{N} \delta^{(3)}(\mathbf{x} - \boldsymbol{\xi}_\alpha)\delta^{(3)}(\mathbf{v} - \dot{\boldsymbol{\xi}}_\alpha).$$

The conservation of phase space density can then be written as,

$$\frac{\partial f}{\partial t} + \mathbf{v}\nabla_x f + \frac{q}{m}\mathbf{E}\nabla_v f = 0,$$

where we used the electrostatic approximation $m\dot{\mathbf{v}} = -q\mathbf{E}$, where m denotes mass and assume only one species of particles. This equation is referred to as *Klimontovich's* equation. The electric field is given self-consistently,

$$\nabla\mathbf{E}(\mathbf{x}, t) = \frac{1}{\varepsilon_0}\int d^3\mathbf{v}\ f(\mathbf{x}, \mathbf{v}, t).$$

These equations together are exact and contain the entire dynamics, including collisional effects. In order to single out the collision part, one can consider a mean field distribution function $\langle f \rangle$, that is averaged over patches $\Delta\Gamma$ of the phase space,

$$\langle f \rangle (\mathbf{x}, \mathbf{v}, t) = \frac{1}{\Delta\Gamma} \int_{\Delta\Gamma} d\Gamma \; f(\mathbf{x}, \mathbf{v}, t),$$

where $\Delta\Gamma = \Delta x \Delta y \Delta z \Delta v_x \Delta v_y \Delta v_z$ is a volume element of 6D phase space.
We can then write the fields as fluctuations around the mean field, denoting the deviations as δf, $\delta\mathbf{E}$ respectively, we can write

$$f = \langle f \rangle + \delta f$$
$$\mathbf{E} = \langle \mathbf{E} \rangle + \delta\mathbf{E}.$$

The fluctuation terms fulfil $\langle \delta\mathbf{E} \rangle = 0$, $\langle \delta f \rangle = 0$, where the former corresponds to Newton's third law. With this splitting, we arrive at the *averaged Klimontovich's equation*,

$$\frac{d}{dt} \langle f \rangle = \frac{\partial \langle f \rangle}{\partial t} + \mathbf{v} \nabla_x \langle f \rangle + \frac{q}{m} \langle \mathbf{E} \rangle \nabla_v \langle f \rangle = -\frac{q}{m} \langle \delta\mathbf{E} \nabla_v \delta f \rangle . \tag{5.1}$$

The collision term on the RHS can intuitively be understood in such a way, that collisions are regarded as interactions of particles with localized field fluctuations.

5.1.2 Liouville's Equation and Truncation Schemes

In contrary to the 6D description, Liouville's equation describes distribution functions in a $6N$D dimensional phase space, where N is the number of particles.
Let us consider the 6D vector $\mathbf{x}_i = (\mathbf{q}_i, \mathbf{p}_i)$ as the phase space coordinates of particle i. The evolution of the N-particle-distribution function is then described by Liouville's equation,

$$\frac{d}{dt} f_N(\mathbf{x}_1, ..., \mathbf{x}_N) = \frac{\partial f_N}{\partial t} + \sum_{i=1}^{N} \frac{\mathbf{p}_i}{m} \frac{\partial f_N}{\partial \mathbf{q}_i} + \sum_{i=1}^{N} \sum_{j<i}^{N} \frac{\partial \phi_{(i,j)}}{\partial \mathbf{q}_i} \frac{\partial f_N}{\partial \mathbf{p}_i} = 0,$$

where $\phi_{(i,j)}$ is the interaction potential between particles i and j. This equation can be rewritten by introducing reduced s-particle-distribution functions with $s < N$, where the degrees of freedom of $N - s$ particles have been integrated out [40],

$$f_s(\mathbf{x}_1, ..., \mathbf{x}_s) = \frac{N!}{(N-s)!} \int d^3\mathbf{x}_{s+1} \cdots d^3\mathbf{x}_N f_N(\mathbf{x}_1, ..., \mathbf{x}_N).$$

This leads to a set of N equations, which are termed the Bogoliubov-Born-Green-Kirkwood-Yvon (BBGKY) hierarchy of equations. The name stems from the hierarchic dependence of f_s on f_{s+1} for $s = 1, ..., N-1$. These equations read as follows [40],

$$\frac{d}{dt} f_s(\mathbf{x}_1, ..., \mathbf{x}_s) = (N-s) \sum_{i=1}^{s} \int d^3\mathbf{x}_s \frac{\partial \phi_{(i,s+1)}}{\partial \mathbf{q}_i} \frac{\partial f_{s+1}}{\partial \mathbf{p}_i}, \qquad s = 1, ..., N-1.$$

Because they depend hierarchically on each other, the RHS for f_s essentially represents the interaction with the $N - s$ remaining particles, that have been integrated out previously. In this picture, collision effects are the cumulation of direct interactions in between particles.

Thanks to the hierarchical structure, solving all these equations would be as impossible as solving Liouville's equation directly. For the purpose of simplification there are various schemes, which

can be used to truncate the series $f_1,\ f_2,\ ...$ at some point, of which the most prominent ones are *Boltzmann*, *Landau* and *Lennard-Balescu*, of which the first two are commonly used in collision modelling. All of them truncate at second order, meaning that they assume binary scattering implicitly.

In the following, these schemes will be illustrated and the differences made clear. In order to get an understanding of the assumptions that these schemes require, the physical meaning of the neglected terms will be shown. For this purpose we write out the last two equations of the hierarchy,

$$\frac{\partial f_1(\mathbf{x}_1)}{\partial t} = -\frac{\mathbf{p}_1}{m}\frac{\partial f_1(\mathbf{x}_1)}{\partial \mathbf{q}_1} + (N-1)\int d^3\mathbf{q}_2 d^3\mathbf{p}_2\ \frac{\partial \phi_{(12)}}{\partial \mathbf{q}_1}\frac{\partial f_2(\mathbf{x}_1,\mathbf{x}_2)}{\partial \mathbf{p}_1}, \tag{5.2a}$$

$$\begin{aligned}\frac{\partial f_2(\mathbf{x}_1,\mathbf{x}_2)}{\partial t} = &-\left(\frac{\mathbf{p}_1}{m}\frac{\partial f_2(\mathbf{x}_1,\mathbf{x}_2)}{\partial \mathbf{q}_1} + \frac{\mathbf{p}_2}{m}\frac{\partial f_2(\mathbf{x}_1,\mathbf{x}_2)}{\partial \mathbf{q}_2}\right)\\ &+ \frac{\phi_{(12)}}{\partial \mathbf{q}_1}\frac{\partial f_2(\mathbf{x}_1,\mathbf{x}_2)}{\partial \mathbf{p}_1} - \frac{\phi_{(21)}}{\partial \mathbf{q}_2}\frac{\partial f_2(\mathbf{x}_1,\mathbf{x}_2)}{\partial \mathbf{p}_2}\\ &+ (N-2)\int d^3\mathbf{q}_3 d^3\mathbf{p}_3\left(\frac{\phi_{(13)}}{\partial \mathbf{q}_1}\frac{\partial f_3(\mathbf{x}_1,\mathbf{x}_2,\mathbf{x}_3)}{\partial \mathbf{p}_1} + \frac{\phi_{(23)}}{\partial \mathbf{q}_2}\frac{\partial f_3(\mathbf{x}_1,\mathbf{x}_2,\mathbf{x}_3)}{\partial \mathbf{p}_2}\right).\end{aligned} \tag{5.2b}$$

Note that each of these equations is complete on its own, as their respective dependency on all other f_i contains the entire physics. For the purpose of illustration one can separate the correlated part from the uncorrelated part, using a *Mayer Cluster expansion* as follows [40],

$$\begin{aligned} f_1(1) &= f_1(1)\\ f_2(1,2) &= f_1(1)f_1(2) + g(1,2)\\ f_3(1,2,3) &= f_1(1)f_2(2)f_3(3) + f_1(1)g(2,3) + f_1(2)g(3,1) + f_1(3)g(1,2) + t(1,2,3).\end{aligned}$$

where g_2 is the two-particle and t_3 the three-particle correlation function respectively. With this we can rewrite eq (5.2b) accordingly:

$$\frac{\partial g}{\partial t} = -\left(\frac{\mathbf{p}_1}{m}\frac{\partial}{\partial \mathbf{q}_1} + \frac{\mathbf{p}_2}{m}\frac{\partial}{\partial \mathbf{q}_2}\right) g(1,2)$$

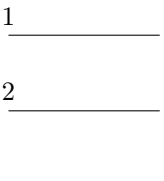

$$+ \frac{\partial \phi_{(1,2)}}{\partial \mathbf{q}_1}\left(\frac{\partial}{\partial \mathbf{p}_1} - \frac{\partial}{\partial \mathbf{p}_2}\right)(f_1(1) f_1(2))$$

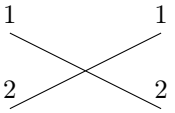

$$+ \frac{\partial \phi_{(1,2)}}{\partial \mathbf{q}_1}\left(\frac{\partial}{\partial \mathbf{p}_1} - \frac{\partial}{\partial \mathbf{p}_2}\right)(g(1,2))$$

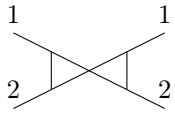

$$+ \int d^3\mathbf{x}_3 \left[\frac{\partial \phi_{(1,2)}}{\partial \mathbf{q}_1}\left(\frac{\partial}{\partial \mathbf{p}_1} - \frac{\partial}{\partial \mathbf{p}_2}\right) f_1(1) g(2,3) + \frac{\partial \phi_{(2,3)}}{\partial \mathbf{q}_2}\left(\frac{\partial}{\partial \mathbf{p}_2} - \frac{\partial}{\partial \mathbf{p}_3}\right) f_1(2) g(1,3) + \frac{\partial \phi_{(1,3)}}{\partial \mathbf{q}_1}\left(\frac{\partial}{\partial \mathbf{p}_1} - \frac{\partial}{\partial \mathbf{p}_3}\right) f_1(3) g(1,2) + \frac{\partial \phi_{(2,3)}}{\partial \mathbf{q}_2}\left(\frac{\partial}{\partial \mathbf{p}_2} - \frac{\partial}{\partial \mathbf{p}_3}\right) f_1(3) g(1,2)\right]$$

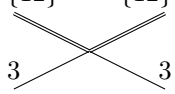

$$+ \int d^3\mathbf{x}_3 \left[\frac{\partial \phi_{(1,3)}}{\partial \mathbf{q}_1}\left(\frac{\partial}{\partial \mathbf{p}_1} - \frac{\partial}{\partial \mathbf{p}_3}\right) t(1,2,3) + \frac{\partial \phi_{(2,3)}}{\partial \mathbf{q}_2}\left(\frac{\partial}{\partial \mathbf{p}_2} - \frac{\partial}{\partial \mathbf{p}_3}\right) t(1,2,3)\right]$$

For simplification and illustration purposes a graphical representation of the mathematical expressions will be used. The first two terms are the propagator and the collision between uncorrelated particles respectively. The third term corresponds to a close encounter, i.e. the colliding particles get near enough to be correlated. Typically, this happens between particles that collide head-on and correspond to events with large scattering angles. The fourth term represents the collision of a correlated system of two with another particle, which can be interpreted as a collision with a screened particle. As previously, the last term contains the entire remaining physics by containing t.

In figure 5.1 it is visualized which terms are being kept by each truncation scheme, according to Baalrud and Daligault [1]. The following can be noted:

- Landau's operator only describes collisions between uncorrelated particles with small scattering angles.
- Lenard-Balescu's approach is the only one to include screening.

For practical applications, especially Boltzmann's and Landau's approach are significant.

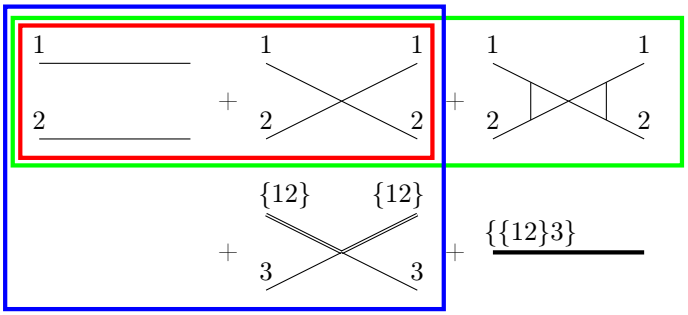

Figure 5.1: Terms kept in BBGKY Truncation Schemes for **Landau**, **Boltzmann** and **Lenard-Balescu**.

5.2 Boltzmann's Collision Operator

Boltzmann's collision operator can be derived from the BBGKY hierarchy using eq (5.2b), by neglecting the last term, which corresponds to assuming that all collisions are binary. A full account of the derivation can be found in [76]. For the sake of brevity, only an intuitive derivation will be given here.

Essentially, Boltzmann's Ansatz for a collision integral (i.e. for the second term of eq (5.2b)) describes the difference between particles that leave and enter a point in 6-dim phase space. Let us denote the probability of changing the velocities $(\mathbf{v}_1, \mathbf{v}_2) \leftrightarrow (\mathbf{v}_1', \mathbf{v}_2')$ with P, which is assumed to be symmetric ("micro-reversible"). The collision term reads as follows,

$$\left(\frac{\partial f}{\partial t}\right)_{\text{coll}} = \int d^3\mathbf{v}_1' \int d^3\mathbf{v}_2' \int d^3\mathbf{v}_2 \; P\left[(\mathbf{v}_1, \mathbf{v}_2) \leftrightarrow (\mathbf{v}_1', \mathbf{v}_2')\right] \cdot \left[f(\mathbf{v}_1')f(\mathbf{v}_2') - f(\mathbf{v}_1)f(\mathbf{v}_2)\right].$$

The probability $P = |\mathbf{v}_2 - \mathbf{v}_1| \frac{d\sigma}{d\Omega}$ is closely related to the cross section, which is assumed to be given by Rutherford's formula. The use of Rutherford's cross section is justified by assuming binary collisions. If θ denotes the scattering angle and $\mathbf{u} = \mathbf{v}_2 - \mathbf{v}_1$ the relative velocity, P looks as follows,

$$B(|\mathbf{u}|, \theta) = \frac{1}{|\mathbf{u}|^3 \sin^4(\theta/2)} \left(\frac{q^2}{4\pi\varepsilon_0 m}\right)^2.$$

Since the cross section only depends on $\mathbf{u}$ and θ, the integration can be changed to angular form,

$$\left(\frac{\partial f}{\partial t}\right)_{\text{coll}} = \left(\frac{q^2}{4\pi\varepsilon_0 m}\right)^2 \int_{S^2} d\Omega \int d^3\mathbf{v}_2 \; \frac{1}{u^3 \sin^4(\theta/2)} \left[f(\mathbf{v}_1')f(\mathbf{v}_2') - f(\mathbf{v}_1)f(\mathbf{v}_2)\right]. \tag{5.3}$$

This operator is singular, since Rutherford's cross section diverges for forward scattering ($\theta \sim 0$). The meaning of this divergence can be understood by the following reasoning. Assuming elastic collisions both energy and momentum are conserved and for particles of equal mass this means the absolute value of the relative velocity stays the same $|\mathbf{u}'| = |\mathbf{u}|$ and only the direction changes. The change in relative momentum $\delta\mathbf{u} = \mathbf{u}' - \mathbf{u}$ is then dependent on the deviation angle,

$$\begin{aligned} |\delta\mathbf{u}|^2 &= |\mathbf{u}'|^2 + |\mathbf{u}|^2 - 2|\mathbf{u}'||\mathbf{u}|\cos\theta \\ &= 2|\mathbf{u}|^2(1 - \cos\theta). \end{aligned} \tag{5.4}$$

This means that collisions with small angles correspond to small changes in velocity. Physically, the divergence translates such that soft collisions with far away particles are the main influence due to the infinite-range nature of Coulomb's potential, that enters through Rutherford's formula. This notion arises as a direct consequence of assuming binary collisions.

5.3 Landau's Approximation

Boltzmann's operator is divergent and to be of use, it must be renormalized. One possible procedure is to exploit the strong dominance of forward scattering and expand the distribution functions in a small angle expansion. This leads to Landau's collision operator [77–79], which is a valid approximation of Boltzmann's operator as long as small scattering angles dominate.

For a collision between two particles of identical mass, we can define the centre of mass vector $\mathbf{v}_{\mathrm{COM}} = (\mathbf{v}_2 + \mathbf{v}_1)/2$. This allows us to write,

$$\mathbf{v}_2 = \mathbf{v}_{\mathrm{COM}} + \frac{\mathbf{u}}{2},$$
$$\mathbf{v}_1 = \mathbf{v}_{\mathrm{COM}} - \frac{\mathbf{u}}{2},$$

where the factor $\frac{1}{2}$ comes from the reduced mass. Since the centre of mass does not change through collision, the change in velocity is dependent only on the change in relative velocity $\mathbf{v}_2' - \mathbf{v}_2 = \delta\mathbf{u}/2$. We can write the following,

$$\mathbf{v}_2' = \mathbf{v}_2 + \frac{1}{2}\delta\mathbf{u},$$
$$\mathbf{v}_1' = \mathbf{v}_1 - \frac{1}{2}\delta\mathbf{u}.$$

Since the absolute value $|\delta\mathbf{u}|$ is small for small angles according to (5.4), we can expand the velocity part of the distribution function $f(\mathbf{v}_2')$,

$$f(\mathbf{v}_2') \approx f(\mathbf{v}_2) + \frac{1}{2}\sum_{i=1}^{3}\delta u^i \frac{\partial f}{\partial v^i}(\mathbf{v}_2) + \frac{1}{8}\sum_{i,j=1}^{3}\delta u^i \delta u^j \frac{\partial^2 f}{\partial v^i \partial v^j}(\mathbf{v}_2) + ... \tag{5.5}$$

For the calculation of the components of $\delta\mathbf{u}$, we can use spherical coordinates, where the axis $\theta = 0$ is coincides with the incoming relative velocity vector $\mathbf{u}$. This choice implies that the scattering angle is the polar angle θ. This yields,

$$\delta\mathbf{u} = \mathbf{u}' - \mathbf{u} = |\mathbf{u}| \left[\begin{pmatrix} \sin\theta\cos\varphi \\ \sin\theta\sin\varphi \\ \cos\theta \end{pmatrix} - \begin{pmatrix} 0 \\ 0 \\ 1 \end{pmatrix} \right].$$

If we insert the expansion eq (5.5) up to second order in Boltzmann's operator eq (5.3), we obtain Landau's equation [33],

$$\frac{d}{dt}f = \sum_{i,j=1}^{3}\frac{\partial}{\partial v_i}\left(f\,\langle\delta u^i\rangle\right) + \frac{1}{2}\frac{\partial^2}{\partial v^i \partial v^j}(f\,\langle\delta u^i \delta u^j\rangle), \tag{5.6}$$

where the averages $\langle\delta u^i\rangle$, $\langle\delta u^i \delta u^j\rangle$ refer to the following angular integral,

$$\langle\delta u^i\rangle(\mathbf{x}, \mathbf{v}_1) = \left(\frac{q^2}{4\pi\varepsilon_0 m}\right)^2 \int d^3\mathbf{v}_2 \int_{S^2} d\Omega\; f(\mathbf{x}, \mathbf{v}_2)\frac{1}{u^3 \sin^4(\theta/2)}\;\delta u^i(|\mathbf{u}|, \theta).$$

Since eq (5.6) has the form of a Fokker-Planck equation, it is often referred to as Landau-Fokker-Planck equation. The divergencies in the angular integrals can be regularized with cut-off parameteres $\theta_\pm$,

$$\langle \delta u^i \rangle (\mathbf{x}, \mathbf{v}_a) = \left(\frac{q^2}{4\pi\varepsilon_0 m} \right)^2 \int d^3\mathbf{v}_2 \int_{\theta_-}^{\theta_+} \sin\theta d\theta \int_0^{2\pi} d\varphi \; f(\mathbf{x}, \mathbf{v}_2) \frac{1}{u^3 \sin^4(\theta/2)} \delta u^i(|u|, \theta).$$

Using eq (5.4), one can find the following,

$$\begin{aligned}
\int_{\theta_-}^{\theta_+} d\theta \; \sin\theta \frac{|\mathbf{u}|}{\sin^4(\theta/2)} &= u \int_{\theta_-}^{\theta_+} d\theta \; \frac{\sin\theta(1-\cos\theta)}{\sin^4(\theta/2)} \\
&\propto \int_{\theta_-}^{\theta_+} d\theta \; \frac{1}{\sin(\theta/2)} \\
&\approx \int_{\theta_-}^{\theta_+} d\theta \; \frac{1}{\theta/2} \\
&= \ln\left(\frac{\theta_+}{\theta_-}\right) =: \Lambda,
\end{aligned}$$

where Λ is called Coulomb logarithm [80] (or Landau logarithm [78]). It is commonly agreed upon that the approximation via small angle expansion is only valid for $\Lambda > 10$ [77, 78, 80]. Physically, this means that the approximation treats collisions as a large number of weak, binary interactions with far away particles. The regularization procedure simply removed all large angle collisions by cutting them out.

As shown by Rosenbluth *et al.* [81] the averages can be rewritten (without additional assumptions) using the so-called Rosenbluth potentials $h(\mathbf{x}, \mathbf{v})$ and $g(\mathbf{x}, \mathbf{v})$, which fulfil a Poisson-like equation. They are computationally easier to handle and can be implemented self-consistently, which was demonstrated by Ji Qiang *et al.* [35]:

$$\begin{aligned}
\langle \delta u^i \rangle &= C \frac{\partial h}{\partial v_i} \qquad \text{with } \nabla^2 h = f \implies h = 2 \int d^3\mathbf{w} \; \frac{f(\mathbf{x}, \mathbf{w})}{|\mathbf{v} - \mathbf{w}|} \\
\langle \delta u^i \delta u^j \rangle &= C \frac{\partial^2 g}{\partial v_i \partial v_j} \quad \text{with } \nabla^2 g = 2h \implies g = \int d^3\mathbf{w} \; f(\mathbf{x}, \mathbf{w}) |\mathbf{v} - \mathbf{w}| \\
C &= \frac{q^4 \Lambda}{4\pi\varepsilon_0^2 m^2}
\end{aligned} \tag{5.7}$$

Coulomb Logarithm

In order to determine the applicability of Landaus collision operator to the case of ultracold electron sources, one needs to find physically reasonable values for $\theta_\pm$ and determine whether $\Lambda > 10$ can be fulfilled. For this purpose λ can be rewritten conveniently with the ratio between the maximum and minimum allowed impact parameters,

$$\Lambda = \ln\left(\frac{r_{\max}}{r_{\min}}\right),$$

since we may rely on Rutherford's formalism.

The divergence of Boltzmann's operator was brought about by the infinite reach of Coulomb's potential. In ideal plasma the range is ultimately capped by Debye shielding, therefore the upper cut-off is readily given by the Debye length $r_{\max} = \lambda_D$.

For the lower cut-off there is quite some controversy regarding the justification. Most authors use the minimal scattering radius (corresponding to $\theta_+ = \pi/2$) from classical collision theory. Above

certain temperatures, this definition can lead to a value of $r_{\min}$ that is smaller than the corresponding de-Broglie wavelength, so the majority chooses the larger one of the two [80, 82, 83]. However, it has been argued, that this choice relates to an assumption regarding the shape of the screening cloud and not to quantum uncertainty [84, 85]. Hence it is expected, that this definition fails at sufficiently low temperatures, as it is tied to assumptions of the screening cloud from ideal plasma physics. These concerns will be ignored in the following since the goal of this chapter is not to obtain the most accurate Coulomb logarithm but rather to estimate the validity of the Landau approximation.

For the purpose of a simple validity estimate, we will differentiate between classical and quantum regime [83]. For the classical case, one chooses the radius of minimal approach, which reads as follows,

$$r_{\min} = \frac{q^2}{4\pi\varepsilon_0 m_e u^2},$$

where $\mathbf{u}$ is the relative velocity before collision. Assuming a thermal Maxwellian distribution, the relative kinetic energy can be expressed through the temperature $m_e u^2 = 3k_B T$. This cut-off parameter is velocity-independent, and therefore cannot remove the divergence of eq (5.3) in the incident energy, which was pointed out by Chang and Li [86–89]. In other words, it is possible that a large angle event is not removed, as long as the kinetic energy is small enough. Likewise, it may happen that small angle events are removed, if the energy is too large. While there are ways to retain the velocity dependence [86, 89–91], the situation for ultra-cold sources is, that the (thermal) energy varies very little and the approximation $m_e u^2 = 3k_B T$ is justified. The mean approximation gives,

$$r_{\min} = \frac{q^2}{12\pi\varepsilon_0 k_B T}.$$

In the classical approximation the Debye length for an electron plasma assumes the following form [39],

$$\lambda_D = \left(\frac{\varepsilon_0 k_B T}{n q^2}\right)^{\frac{1}{2}}.$$

Together this gives the classical Coulomb logarithm for electron-electron collisions,

$$\begin{aligned}\Lambda^{\mathrm{cl}} &= \ln\left(\frac{\varepsilon_0^{3/2} 12\pi}{q^3}\right) + \frac{1}{2}\ln\left(\frac{(k_B T)^3}{n}\right) \\ &\approx 23.463 + \frac{1}{2}\ln\left(\frac{T[\mathrm{eV}]^3}{n[\mathrm{cm}^{-3}]}\right).\end{aligned}$$

Above certain temperatures, this must be replaced with a quantum mechanical analogon, which can be obtained from a quantum cross section. In the final form this enters via correction term [83],

$$\begin{aligned}\Lambda^{\mathrm{qm}} &= \Lambda^{\mathrm{cl}} + \ln\left(\frac{2\alpha c m_e^{1/2}}{(3k_B T)^{1/2}}\right) - \frac{1}{2} \\ &= \Lambda^{\mathrm{cl}} + 1.796 + \frac{1}{2}\ln\left(\frac{1}{k_B T}\right) - \frac{1}{2} \\ &\approx 23.948 + \frac{1}{2}\ln\left(\frac{T[\mathrm{eV}]^2}{n[\mathrm{cm}^{-3}]}\right).\end{aligned}$$

The critical temperature T_c that distinguishes both regimes is found, where both definitions agree. It evaluates to [83],

$$T_c \approx 6.67 \text{ eV} \approx 77405.13 \text{ K},$$

from which we see, that for the purpose of modelling ultracold electron sources the classical definition suffices.

Mathematically, the Coulomb logarithm is a renormalization parameter, that - physically - is a measure for the dominance of small-angle (soft) collisions with far-away particles over short and hard collisions. In table 5.1, it is shown how the values of Λ can be used to distinguish different regimes [82].

Value	**regime**
$\Lambda > 10$	weak coupling
$2 < \Lambda < 10$	moderate coupling
$\Lambda < 2$	strong coupling

Table 5.1: Different Coupling regimes according to their Coulomb Logarithm.

For the weak coupling regime, Landau's operator provides a good approximation. From figure 5.2 we see that Landau's approximation in the classical limit holds in the ultracold regime only if the density is very small.

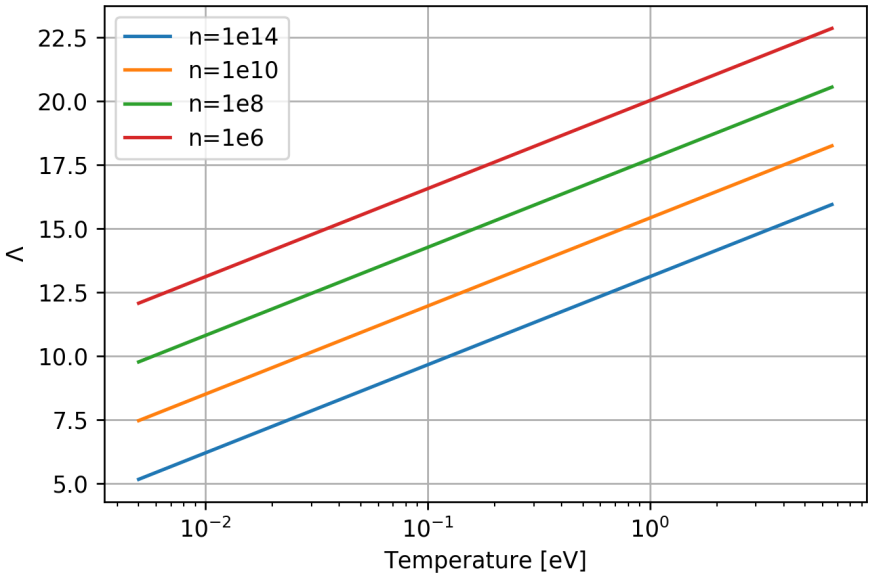

Figure 5.2: Classical Coulomb logarithm as a function of temperature for various electron densities.

In order to get an idea about actual applications, one can assume cylindrical bunches of volumes in between 8e-4 and 6e-2 cm^3. In the low (resp. high) charge regime with 20 pC (resp. 20 nC) the Coulomb logarithm assumes the values as depicted in figure 5.3.
The values for the (classical) Coulomb logarithm shown in figure 5.3 suggest, that the Landau approximation does not hold in the ultracold regime. In other words, large-angle collisions contribute

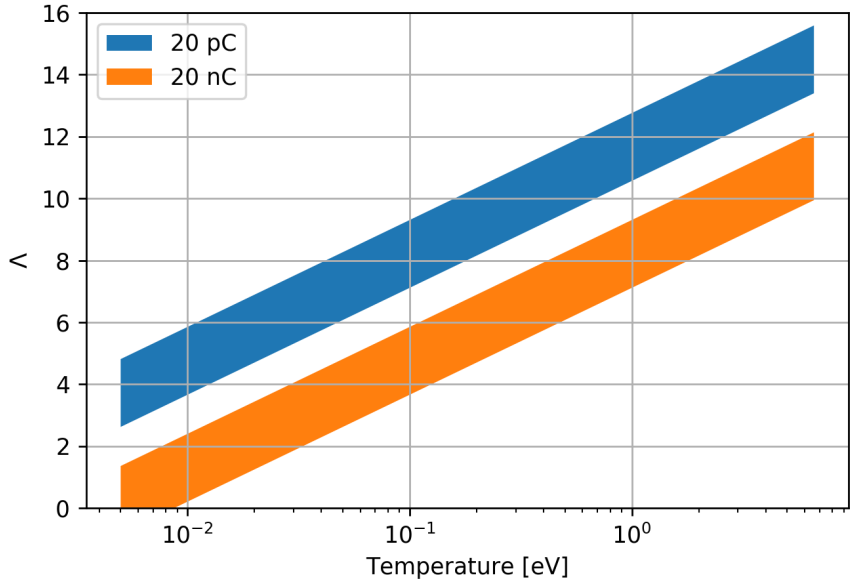

Figure 5.3: Classical Coulomb logarithm in the low and high-charge regime for cylindrical bunches with radii in between 0.5 and 2 mm and lengths in between 1 and 5 mm.

significantly to the dynamics.

So far, the Coulomb logarithm rests on the assumption that collisions are binary and Rutherford's scattering cross section is suitable to describe collisions within plasma. It is shown in figures 4.2-4.6 that inter-particle correlation effects, that arise in ultracold sources, significantly alter the collision cross section compared to Rutherford's result. While the Coulomb logarithm can be generalized to account for correlation effects [82], for the purpose of this thesis, it is only relevant whether this changes the validity of Landau's approximation. To get an idea how the Coulomb logarithm changes by including correlation effects, one can include Debye shielding numerically. In the following we will use the approximation provided by Ordonez and Molina [92] to include Debye shielding. The Coulomb logarithm for a Yukawa-screened potential is denoted by $\tilde{\Lambda}^{\mathrm{cl}}$ and reads,

$$\begin{aligned} \iota &= 1.17 e^{\Lambda^{\mathrm{cl}}} \\ \tilde{\Lambda}^{\mathrm{cl}} &= \frac{(1+\iota)^2 \log(1+\iota)}{(2+\iota)^2} - \frac{\iota}{2(1+\iota)} + 0.15\iota e^{-0.5\iota}. \end{aligned}$$

The dependence on the temperature is best illustrated graphically. For the same range of values as in figure 5.3 the Coulomb logarithm for a Yukawa-screened potential is shown in figure 5.4.

Apart from a slight overall decrease in value, the form changes only in the high-charge regime for temperatures below 0.1 eV. In general, the above statement still holds: typical ultracold electron sources display moderate or strong coupling. Additionally, we can see that the introduction of Debye-shielding restricts the Coulomb logarithm to strictly positive values. This can be interpreted as a feature brought about by using an interaction potential that naturally accommodates the cut-off regularization.

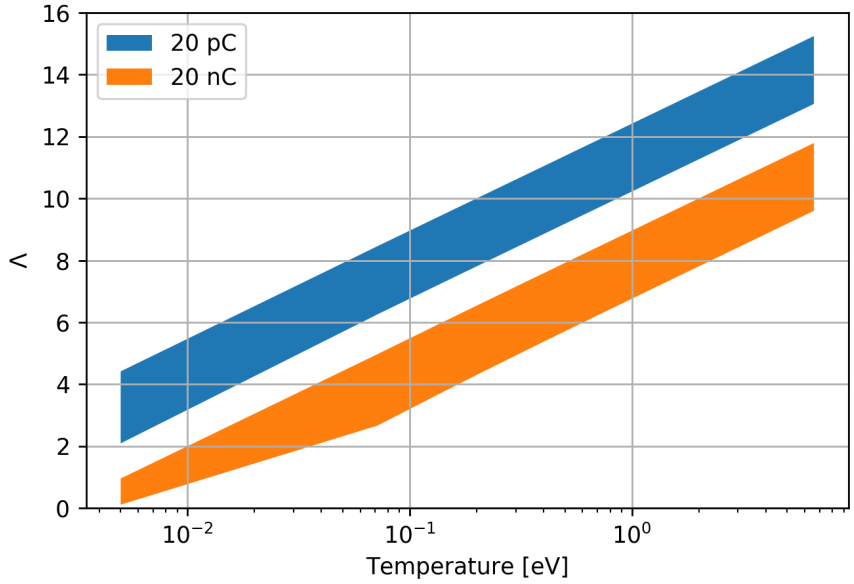

Figure 5.4: Classical screened Coulomb logarithm in the low and high-charge regime for cylindrical bunches with radii in between 0.5 and 2 mm and lengths in between 1 and 5 mm.

Possibilities of Extension

As demonstrated by Li [93] it is possible to retain a third-order term in the small-angle expansion eq (5.5) to obtain a collision operator that holds in the moderate coupling regime. The collision operator takes the following form,

$$\left(\frac{\partial}{\partial t}f\right)_{\text{coll}} = \sum_{i=1}^{3}\frac{\partial}{\partial v_i}\left(f\,\langle\delta u^i\rangle\right) + \frac{1}{2}\sum_{i,j=1}^{3}\frac{\partial^2}{\partial v^i\partial v^j}\left(f\,\langle\delta u^i\delta^j\rangle\right) - \frac{1}{6}\sum_{i,j,k=1}^{3}\frac{\partial^3}{\partial v_i\partial v_j\partial v_k}\left(f\,\langle\delta u^i\delta u^j\delta u^k\rangle\right),$$

where the last term can be represented with a vector potential that has an expression similar to Rosenbluth's potentials (5.7).

The main drawback is that the distribution equation can no longer be expressed through a Langevin approach, due to Pawula's theorem, which is shown in detail e.g. by Risken and Frank [32]. With this in mind, there is no easy way to find a system of corresponding microscopic equations. Additionally, it is unclear whether the truncation after the third term is justified or not [82]. The first two terms are of order $\mathcal{O}(\lambda)$ and are dominant, as long as $\lambda >> 1$. The remaining terms are all of the same order and there is a priori no reason to prefer one of them.

5.3.1 Langevin Equation

For completeness' sake a brief description of the the Langevin equation will be given. Usually, simulations rely on microscopic variables like position and velocity rather than macroscopic distribution functions. The Langevin equation is a microscopic formulation of the Landau equation,

which is significantly more practical for applications.

The Landau-Fokker-Planck equation (5.6) with Rosenbluth's notation (5.7) reads as follows,

$$\frac{\partial f}{\partial t} + \mathbf{v}\ \nabla_v f + \frac{\mathbf{F}}{m}\nabla_x f = \frac{q^4\Lambda}{4\pi\varepsilon_0^2 m^2}\sum_{i,j=1}^{3}\left[\frac{\partial}{\partial v_i}\left(f\frac{\partial h}{\partial v_i}\right) + \frac{1}{2}\frac{\partial^2}{\partial v^i \partial v^j}\left(f\frac{\partial^2 g}{\partial v_i \partial v_j}\right)\right].$$

This can be written in a bit more generic form with a dynamic friction term $\mathbf{F}_d$ and a Diffusion matrix D,

$$\frac{\partial f}{\partial t} + \mathbf{v}\ \nabla_v f + \frac{\mathbf{F}}{m}\nabla_x f = \sum_{i,j=1}^{3}\left[\frac{\partial}{\partial v_i}\left(fF_d^i\right) + \frac{1}{2}\frac{\partial^2}{\partial v^i \partial v^j}\left(fD^{ij}\right)\right].$$

Although Landaus equation is deterministic, it is equivalent to a set of Langevin equations, which are themselves stochastic. In other words, if all particles in a distribution are evolved according to a Langevin equation, it yields the same as if the distribution is evolved according to the Fokker-Planck equation. In generic form Langevin's equation can be stated as follows [32, 35],

$$\dot{\mathbf{v}} = \boldsymbol{\alpha}(\mathbf{v}, t) + \beta(\mathbf{v}, t)\boldsymbol{\Gamma}(t),$$

where Γ is δ-correlated noise,

$$\langle\Gamma_i(t)\rangle = 0 \tag{5.8a}$$
$$\langle\Gamma_i(t)\Gamma_j(t')\rangle = 2\delta_{ij}\delta(t-t'). \tag{5.8b}$$

Intuitively spoken, $\boldsymbol{\Gamma}$ is a different random variable at each time step. In this sense they are independent and identically distributed normal random variables. According to Wiener-Khintchine's theorem the spectral density of $\boldsymbol{\Gamma}$ is constant, which is the reason it is referred to as "white" noise.

The link between both descriptions is given by the following relations,

$$F_d^i = \alpha^i,$$
$$D_{ij} = \sum_{k=1}^{3}\beta_{ik}\beta_{jk}$$

The reverse relationship can be found as well,

$$\beta_{ij} = (\sqrt{D})_{ji}.$$

The proof that these formulas indeed imply the equivalence of Fokker-Planck's equation with Langevin's equation can be found e.g. in the book by Risken and Frank [32]. Consequentially, both approaches share the same underlying assumptions and drawbacks.

Chapter 6

Variational Description of Collision Dynamics

In the following, a fully discrete Lagrangian description of the P^{3}M algorithm will be developed for the first time. This formalism will be employed to investigate the applicability in the ultracold regime and whether near-field interaction must adhere to electrostatic boundary conditions. This chapter mainly revolves around the P^{3}M algorithm but analogous considerations could be made about other direct simulation schemes.

6.1 Collisionless Lagrangian

A Lagrangian approach is commonly used to describe beam dynamics in particle accelerators. For photocathode-based electron sources the dominating influence are conservative electromagnetic forces either from external fields or from inter-particle interaction. The conservative nature means firstly that Liouville's theorem holds and secondly that a Lagrangian description is warranted.

The first collisionless Lagrangian description stems from Low and Chandrasekhar [94], whose derivation (but not result) was later corrected by Galloway and Kim [95]. It is not the only possibility for a Lagrangian [96] but reproduces the physical equations of motions nevertheless, as shown by Evstatiev and Shadwick [97], whose notation will be used in the following.

We denote the 6-dim phase space distribution as $f(\mathbf{x}, \mathbf{v}, t) = f(\mathbf{x}(t), \mathbf{v}(t), t)$. The quantities $\mathbf{x}$, $\mathbf{v}$ are themselves solutions to the equations of motion and only dependent on time t and on initial conditions $\mathbf{x}_0$, $\mathbf{v}_0$. If Liouville's theorem holds, we can express the distribution at time t through an initial distribution f_0 as $f(\mathbf{x}(t), \mathbf{v}(t), t) = f_0(\mathbf{x}_0, \mathbf{v}_0)$, i.e. there is no time dependence. Speaking in terms of fluid dynamics, $\mathbf{x}_0$, $\mathbf{v}_0$ are Eulerian variables and $\mathbf{x}$, $\mathbf{v}$ and the potential ϕ are Lagrangian fields.
With this in mind, Low's Lagrangian reads as follows,

$$\begin{aligned}\mathcal{L}(\mathbf{x}, \mathbf{v}, \phi) &= \int d^3\mathbf{x}_0 \int d^3\mathbf{v}_0 \; f_0(\mathbf{x}_0, \mathbf{v}_0) \left[\frac{1}{2} m\mathbf{v}^2(\mathbf{x}_0, \mathbf{v}_0) - q\phi(\mathbf{x}(\mathbf{x}_0, \mathbf{v}_0))\right] + \frac{\varepsilon_0}{2} \int d^3\mathbf{x} (\nabla\phi)^2(\mathbf{x}(\mathbf{x}_0, \mathbf{v}_0)) \\ &= \mathcal{L}_p + \mathcal{L}_{\text{int}} + \mathcal{L}_f,\end{aligned} \tag{6.1}$$

where the first and last term represent particle and field energy respectively. The interaction term can be simplified considering that after integrating f over velocity we are left with the spatial

charge distribution,

$$\int d^3\mathbf{x}\ \rho(\mathbf{x}) = \int d^3\mathbf{x}_0 \int d^3\mathbf{v}_0\ q f_0(\mathbf{x}_0, \mathbf{v}_0) = \int d^3\mathbf{x} \int d^3\mathbf{v}\ q f(\mathbf{x}, \mathbf{v}),$$

where it was used, that,

$$f_0(\mathbf{x}_0, \mathbf{v}_0) d^3\mathbf{x}_0 d^3\mathbf{v}_0 = f(\mathbf{x}, \mathbf{v}) d^3\mathbf{x} d^3\mathbf{v}. \tag{6.2}$$

The physical meaning of eq (6.2) is particle number conservation for a phase space element [95], which is a consequence of Liouville's theorem.

The equations of motion can be obtained by variation after $\mathbf{x}$ and $\phi(\mathbf{x}_0)$ respectively,

$$\begin{aligned} m\ddot{\mathbf{x}} &= -q\nabla_x \phi(\mathbf{x}), \\ \nabla_x^2 \phi(\mathbf{x}_0) &= \frac{1}{\varepsilon_0} \int d^3\mathbf{v}\ f(\mathbf{x}_0, \mathbf{v})\ q =: \frac{\rho(\mathbf{x}_0)}{\varepsilon_0} \end{aligned}$$

and turn out as expected.
In order to transition to a discrete set of particles, we can compartmentalize the distribution function with macro-particles f_α, which have a finite spatial shape S_x, a finite velocity shape S_v, a weight ω_α and are located at the position $\boldsymbol{\xi}$,

$$\begin{aligned} f(\mathbf{x}, \mathbf{v}) &= \sum_\alpha f_\alpha(x, v, t) \\ &= \sum_\alpha \omega_\alpha S_x(\mathbf{x} - \boldsymbol{\xi}_\alpha) S_v(\dot{\mathbf{x}} - \dot{\boldsymbol{\xi}}_\alpha). \end{aligned} \tag{6.3}$$

Usually, the ω_α are chosen as the amount of physical particles per macroparticle, S_v is a δ-function and S_x is a B-spline function of order 0 or 1. In the limit of small particle numbers this is not necessary and we can replace S_x, S_v with δ functions accordingly. There are only a few conditions that the shape functions must fulfil. Additionally to being symmetric and compact, it should be normalized to 1,

$$\int_{-\infty}^{\infty} S_x(\mathbf{x} - \boldsymbol{\xi}) d^3\mathbf{x} = 1 = \int_{-\infty}^{\infty} S_v(\dot{\mathbf{x}} - \dot{\boldsymbol{\xi}}) d^3\mathbf{v}.$$

The resulting Lagrangian depends on a discrete set of position and velocity coordinates $\{\boldsymbol{\xi}_\alpha\}$, and a continuous field $\phi(\mathbf{x})$ and looks as follows,

$$\mathcal{L}(\{\boldsymbol{\xi}_\alpha\}, \{\dot{\boldsymbol{\xi}}_\alpha\}, \phi) = \sum_\alpha \frac{m}{2} \omega_\alpha \dot{\boldsymbol{\xi}}_\alpha^2 - \sum_\alpha \omega_\alpha \int d^3\mathbf{x}\ S_x(\mathbf{x} - \boldsymbol{\xi}_\alpha) \phi(\mathbf{x}) + \frac{\varepsilon_0}{2} \int d^3\mathbf{x} (\nabla\phi)^2(\mathbf{x}). \tag{6.4}$$

The charge distribution at $\mathbf{x}$ is now given as the contribution of every particle $\boldsymbol{\xi}_\alpha$ to this point,

$$\rho(\mathbf{x}) = \sum_\alpha \omega_\alpha S_x(\mathbf{x} - \boldsymbol{\xi}_\alpha).$$

6.1.1 Spatial Discretization

P^{3}M and other mesh-based approaches rely on the discretization of the spatial coordinate onto a finite grid. A priori all coordinate systems can be discretized this way but for the sake of argument, lets imagine an euclidean coordinate space $[0, L_x] \times [0, L_y] \times [0, L_z]$ that is discretized as $L_x = N_x h_x$, $L_y = N_y h_y$, $L_z = N_z h_z$. Likewise the electromagnetic potential is given only at a discrete set of mesh-points $\phi_{klm} = \phi(k \cdot h_x, l \cdot h_y, m \cdot h_z)$. To reconcile this with the continuous Lagrangian description, we can use finite element functions $I(x)$ to interpolate in between grid points [97],

$$\phi(\mathbf{x}) = \sum_{klm} \phi_{klm} I_k \left(\frac{x_k - x}{h_x} \right) I_l \left(\frac{y_l - y}{h_y} \right) I_m \left(\frac{z_m - z}{h_z} \right).$$

We can use multi-index notation $i = (k, l, m)$ to write this more succinctly as,

$$\phi(\mathbf{x}) = \sum_i \phi_i I_i \left(\frac{\mathbf{x}_i - \mathbf{x}}{\Delta \mathbf{x}} \right). \tag{6.5}$$

The easiest choice for I_i are B-splines of 0th order, which essentially corresponds to assume a constant charge distribution over a computational cell. This can be seen from the definition,

$$I_i \left(\frac{\mathbf{x}_i - \mathbf{x}}{\Delta \mathbf{x}} \right) = b_0 \left(\frac{\mathbf{x}_i - \mathbf{x}}{\Delta \mathbf{x}} \right) = \begin{cases} 1 & \text{if} \quad \left(\frac{\mathbf{x}_i - \mathbf{x}}{\Delta \mathbf{x}} \right) < \frac{1}{2}. \\ 0 & \text{otherwise.} \end{cases}$$

Alternatively, we can rewrite this as,

$$I_i \left(\mathbf{x}_i - \mathbf{x} \right) = b_0 \left| \mathbf{x}_i - \mathbf{x} \right| = \begin{cases} 1 & \text{if} \quad |\mathbf{x}_i - \mathbf{x}| < |\Delta \mathbf{x}|/2. \\ 0 & \text{otherwise.} \end{cases}$$

Additionally, the derivative in the field energy term must be approximated using finite differences. An x-directed finite difference operator of second order D_x acting on a discrete 3-dim potential ϕ_{jlm} can be defined as follows [98],

$$\begin{aligned} (D_x \phi)_{klm} &= \sum_j (D_x)_{kj} \phi_{jlm} = \phi_{(k+1)lm} + \phi_{(k-1)lm} - 2\phi_{klm} \\ (D_x)_{ji} &= \delta_{j(i+1)} + \delta_{j(i-1)} - 2\delta_{ji} \end{aligned} \tag{6.6}$$

Through the way the mesh was defined, it was already implicitly assumed, that the coordinates are separable. Thus the multi-dimensional discrete Laplacian can be construcuted directly through a Kronecker-sum of discrete one-dimensional Laplacians,

$$D_{xyz} = D_x \otimes \mathbb{1}_y \otimes \mathbb{1}_z + \mathbb{1}_x \otimes D_y \otimes \mathbb{1}_z + \mathbb{1}_x \otimes \mathbb{1}_y \otimes D_z,$$

where $\otimes$ denotes the tensor product. This assumption holds as long as the respective coordinate system is not curved, which usually not the case for mesh-based algorithms. The matrix elements of this operator can analogously be defined as a sum of Kronecker-Deltas,

$$(D_{xyz})_{abc;def} = (D_x)_{ab} \delta_{cd} \delta_{ef} + \delta_{ab} (D_y)_{cd} \delta_{ef} + \delta_{ab} \delta_{cd} (D_z)_{ef}.$$

Before discretization of $\mathcal{L}_{\text{int}}$, one can use partial integration to achieve second order, which allows to directly use finite differences of second order:

$$\begin{aligned} \int d^3\mathbf{x} \, (\nabla \phi(\mathbf{x})) \cdot (\nabla \phi(\mathbf{x})) &= - \int d^3\mathbf{x} \, \phi(\mathbf{x}) \Delta \phi(\mathbf{x}) \\ &= -h_x h_y h_z \sum_{klm} \phi_{klm} (\Delta \phi(\mathbf{x}))_{klm} \\ &= -h_x h_y h_z \sum_{klm} \sum_{abc} \phi_{klm} (D_{xyz})_{klm;abc} \phi_{abc} \\ &= -h_x h_y h_z \sum_i \sum_j \phi_i (D_{xyz})_{i;j} \phi_j, \end{aligned} \tag{6.7}$$

where $i = (k, l, m)$ and $j = (a, b, c)$ are multiindices as defined before.

The discretization of the field has additionally brought about a discrete charge distribution. This can be seen by looking at the interaction term of (6.4),

$$\begin{aligned}\mathcal{L}_{\text{int}} &= -\sum_\alpha q\omega_\alpha \sum_i \phi_i \int d^3\mathbf{x}\; S_x(\mathbf{x}-\boldsymbol{\xi}_\alpha) b_0\left(\frac{\mathbf{x}_i-\mathbf{x}}{\Delta\mathbf{x}}\right)\\ &= -\sum_\alpha q\omega_\alpha \sum_i \phi_i W(\mathbf{x}_i-\boldsymbol{\xi}_\alpha)\\ &= -\sum_i \phi_i\rho_i\\ \rho_i &= \sum_\alpha \omega_\alpha q W(\mathbf{x}_i-\boldsymbol{\xi}_\alpha),\end{aligned}$$

where we have defined the interpolation function W that mediates between particles and grid. If we choose $S_x = b_0$ we regain cloud-in-cell interpolation via the recursion relation for splines,

$$W\left(\frac{\mathbf{x}_i-\boldsymbol{\xi}}{\Delta\mathbf{x}}\right) = \int d^3\mathbf{x}\; b_0\left(\frac{\mathbf{x}-\boldsymbol{\xi}}{\Delta\mathbf{x}}\right) b_0\left(\frac{\mathbf{x}_i-\mathbf{x}}{\Delta\mathbf{x}}\right) = b_1\left(\frac{\mathbf{x}_i-\boldsymbol{\xi}}{\Delta\mathbf{x}}\right).$$

The spatially fully discretized Lagrangian then reads as follows,

$$\mathcal{L} = \sum_\alpha \frac{m}{2}\omega_\alpha \dot{\boldsymbol{\xi}}_\alpha^2 - \sum_\alpha q\omega_\alpha \sum_i \phi_i W(\mathbf{x}_i-\boldsymbol{\xi}_\alpha) - \varepsilon_0 h_x h_y h_z \sum_i\sum_j \phi_i (D_{xyz})_{i;j}\phi_j.$$

This reproduces correctly the discretized equations motion as can be seen by varying ϕ_m and $\boldsymbol{\xi}_\beta$ respectively,

$$(D_{xyz})_{m;j}\phi_j = \frac{1}{\varepsilon_0}\frac{\rho_m}{h_x h_y h_z} \tag{6.8a}$$

$$m\omega_\beta \ddot{\boldsymbol{\xi}}_\beta = -\sum_i \frac{dW}{d\boldsymbol{\xi}}(\mathbf{x}_i-\boldsymbol{\xi}_\beta)\phi_i. \tag{6.8b}$$

The inverse volume factor in (6.8a) is due to assuming that the charge value at grid site $\mathbf{x}_i$ is the average over the cell. The derivative term of the interpolation function in eq (6.8b) can be unterstood as a forward finite difference operator of first order if we use splines as above,

$$\begin{aligned}\frac{d}{d\boldsymbol{\xi}}W(\mathbf{x}_i-\boldsymbol{\xi}) &= \frac{d}{d\boldsymbol{\xi}}\; b_1(\mathbf{x}_i-\boldsymbol{\xi})\\ &= 3\frac{b_0(\mathbf{x}_{i+1}-\boldsymbol{\xi}) - b_0(\mathbf{x}_i-\boldsymbol{\xi})}{3h},\end{aligned}$$

where the factor 3 arises due to summation over three directions in the multiindex i. This tensor locates the grid points nearest to $\boldsymbol{\xi}$ and takes the finite difference of first order.

6.1.2 Temporal Discretization

Every numerical scheme that solves a differential equation of motion presumes a discrete stepping in time. In the following, it will be shown how the Lagrangian can be made to reflect the time discretization by using variational integrators [99–101]. The basic idea is that the optimal trajectory - as described by Hamilton's principle - that minimizes the action is approximated via a discrete

set of patches $\mathcal{L}_d$. The action functional is approximated by a sum over M patches with size Δt,

$$\begin{aligned} S &= \int dt\ \mathcal{L}(\boldsymbol{\xi}(t), \dot{\boldsymbol{\xi}}(t), \phi(\boldsymbol{\xi}(t), t)) \\ &\approx \sum_{n=0}^{M-1} \int_{t_n}^{t_{n+1}} dt\ \mathcal{L}(\boldsymbol{\xi}(t), \dot{\boldsymbol{\xi}}(t), \phi(\boldsymbol{\xi}(t), t)) \\ &\approx \sum_{n=0}^{M-1} \mathcal{L}_d(\boldsymbol{\xi}^n, \boldsymbol{\xi}^{n+1}, \phi^n, \phi^{n+1}, \Delta t), \end{aligned}$$

where,

$$\begin{aligned} \boldsymbol{\xi}^n &= \boldsymbol{\xi}(n \cdot \Delta t) \\ \phi^n &= \phi(\boldsymbol{\xi}(n \cdot \Delta t), n \cdot \Delta t) \\ \mathcal{L}_d(\boldsymbol{\xi}^n, \boldsymbol{\xi}^{n+1}, \phi^n, \phi^{n+1}, \Delta t) &= \int_{t_n}^{t_{n+1}} dt\ \mathcal{L}(\boldsymbol{\xi}(t), \dot{\boldsymbol{\xi}}(t), \phi(\boldsymbol{\xi}(t), t), t). \end{aligned}$$

To reproduce the equations of motion, it is enough to consider the Lagrangian at three points and vary with respect to the middle point [100]. Essentially, this works because discrete equations of motion propagate solutions time step by time step. One can discretize the Lagrangian in the following way,

$$\mathcal{L} \to \mathcal{L}_d(\boldsymbol{\xi}^{n-1}, \boldsymbol{\xi}^n, \phi^{n-1}, \phi^n, \Delta t) + \mathcal{L}_d(\boldsymbol{\xi}^n, \boldsymbol{\xi}^{n+1}, \phi^n, \phi^{n+1}, \Delta t). \tag{6.9}$$

The equations of motion are then given through the discrete Euler-Lagrange equations. For example in the coordinate $\boldsymbol{\xi}$, this looks as follows,

$$\frac{d}{d\boldsymbol{\xi}^n}\mathcal{L}_d(\boldsymbol{\xi}^{n-1}, \boldsymbol{\xi}^n, \phi^{n-1}, \phi^n) - \frac{d}{d\boldsymbol{\xi}^n}\mathcal{L}_d(\boldsymbol{\xi}^n, \boldsymbol{\xi}^{n+1}, \phi^n, \phi^{n+1}) = 0. \tag{6.10}$$

For the most commonly used symplectic integrator - the leap-frog method - one chooses the piecewise Lagrangian in the following way [100],

$$\mathcal{L}_d(\boldsymbol{\xi}^n, \boldsymbol{\xi}^{n+1}, \phi^n, \phi^{n+1}) = \mathcal{L}\left(\boldsymbol{\xi}^n, \frac{\boldsymbol{\xi}^{n+1} - \boldsymbol{\xi}^n}{\Delta t}, \phi(\boldsymbol{\xi})\right),$$

where $\mathcal{L}$ is the time-continuous Lagrangian. Insertion into eq (6.9) leads to the fully discretized three-point Lagrangian,

$$\begin{aligned} \mathcal{L} = &\sum_\alpha \frac{m}{2}\omega_\alpha \left[\frac{\boldsymbol{\xi}_\alpha^n - \boldsymbol{\xi}_\alpha^{n-1}}{\Delta t}\right]^2 - \sum_\alpha q\omega_\alpha \sum_i \phi_i^{n-1} W(\mathbf{x}_i - \boldsymbol{\xi}_\alpha^{n-1}) - \varepsilon_0 h_x h_y h_z \sum_i \sum_j \phi_i^{n-1}(D_{xyz})_{i;j}\phi_j^{n-1} \\ &+ \sum_\alpha \frac{m}{2}\omega_\alpha \left[\frac{\boldsymbol{\xi}_\alpha^{n+1} - \boldsymbol{\xi}_\alpha^n}{\Delta t}\right]^2 - \sum_\alpha q\omega_\alpha \sum_i \phi_i^n W(\mathbf{x}_i - \xi_\alpha^n) - \varepsilon_0 h_x h_y h_z \sum_i \sum_j \phi_i^n (D_{xyz})_{i;j}\phi_j^n. \end{aligned} \tag{6.11}$$

Variation after $\boldsymbol{\xi}_\beta^n$ yields the fully discrete equation of motion for the particle coordinate,

$$\begin{aligned} & m\omega_\beta \frac{1}{\Delta t^2}(\boldsymbol{\xi}_\beta^n - \boldsymbol{\xi}_\beta^{n-1} - \boldsymbol{\xi}_\beta^{n+1} + \boldsymbol{\xi}_\beta^n) = -q\omega_\beta \sum_i \phi_i^n \frac{dW}{d\boldsymbol{\xi}_\beta^n}(\mathbf{x}_i - \boldsymbol{\xi}_\alpha^n) \\ \implies & m\omega_\beta \frac{1}{\Delta t^2}(\boldsymbol{\xi}_\beta^{n-1} + \boldsymbol{\xi}_\beta^{n+1} - 2\boldsymbol{\xi}_\beta^n) = q\omega_\beta \sum_i \phi_i^n \frac{dW}{d\boldsymbol{\xi}_\beta^n}(\mathbf{x}_i - \boldsymbol{\xi}_\alpha^n), \end{aligned}$$

where we recognize a finite difference of order two in the temporal domain.
The corresponding Poisson's equation can be found by varying ϕ_m^n,

$$\sum_j (D_{xyz})_{m;j}\phi_j^n = \frac{1}{\varepsilon_0 h_x h_y h_z}\sum_\alpha qW(\mathbf{x}_i - \boldsymbol{\xi}_\alpha^n).$$

6.2 Ewald's Summation

In order to include collisions into eq (6.11) and transition to the P^{3}M algorithm, the approach will first be motivated by introducing Ewald summation, on which P^{3}M is based.

The electrostatic energy within a charged many-body system is ultimately determined by the pairwise interaction between the particles. Denoting the position and charge of particle i with $\mathbf{r}_i$, q_i respectively, the electrostatic energy for a set of N point particles is given as follows,

$$E = \sum_{i<j}^{N} \frac{q_i q_j}{|\mathbf{r}_i - \mathbf{r}_j|}$$

In cases where a large number of particles is present or many copies of the same system are needed, the direct evaluation of the sum becomes rather costly. The main idea of Ewalds summation [102] is to split the interaction in two parts - long and short ranged - which can be summed individually. The Coulomb potential decays with $\mathcal{O}(r^{-1})$, which means it varies strongly on the short range and slowly on the long range. The advantage of the splitting is, that the long-range part can be summed efficiently in Fourier space, since only few k vectors are needed due to slow variation, whereas the short-range part can be summed in coordinate space. The splitting can be written as follows,

$$\frac{1}{r} = \frac{1-f(r)}{r} + \frac{f(r)}{r}.$$

In the context of electromagnetic interaction, one usually chooses f as the error function,

$$f(r) = \mathrm{Erf}(\alpha r) = \frac{1}{2\sqrt{\pi}}\int_{\alpha r}^{\infty} dt\ e^{-t^2},$$

which gives,

$$\frac{1}{|\mathbf{r}_i - \mathbf{r}_j|} = \frac{\mathrm{Erfc}(\alpha|\mathbf{r}_i - \mathbf{r}_j|)}{|\mathbf{r}_i - \mathbf{r}_j|} + \frac{\mathrm{Erf}(\alpha|\mathbf{r}_i - \mathbf{r}_j|)}{|\mathbf{r}_i - \mathbf{r}_j|}. \tag{6.12}$$

This can be used to split above sum accordingly, where we can already represent the long-range part in Fourier space,

$$E = \sum_{i<j}^{N} \frac{\mathrm{Erfc}(\alpha|\mathbf{r}_i - \mathbf{r}_j|)}{|\mathbf{r}_i - \mathbf{r}_j|} q_i q_j + \sum_{i<j}^{N}\sum_k \frac{4\pi}{k^2} e^{i\mathbf{k}(\mathbf{r}_i - \mathbf{r_j})} e^{-k^2/(4\alpha^2)} q_i q_j.$$

The second part can be evaluated in Fourier space, by using the definition of the Fourier-Transformed charge distribution $\hat{\rho}(\mathbf{k}) = \sum_{i<j} q_i e^{i\mathbf{k}(\mathbf{r}_i - \mathbf{r}_j)}$,

$$E = \sum_{i<j}^{N} \frac{\mathrm{Erfc}(\alpha|\mathbf{r}_i - \mathbf{r}_j|)}{|\mathbf{r}_i - \mathbf{r}_j|} q_i q_j + \sum_k \frac{4\pi}{k^2} |\hat{\rho}(\mathbf{k})| e^{-k^2/(4\alpha^2)} q_j. \tag{6.13}$$

Note, that we have omitted the self-energy from the start, otherwise this would have to be subtracted separately.

6.3 P^{3}M

The P^{3}M algorithm [15, 16, 18, 102–107] is an Ewald summation on a grid, which employs DFFT to quickly handle the second sum of eq (6.13) in reciprocal space. In practice this is done by using a Particle-in-Cell scheme for the long-range forces, complemented by adding a direct summation of the short-range forces. In other words, the long-range interaction is calculated by solving Poisson's equation on a grid, whereas the short-ranged counterpart is summed directly.

Instead of splitting the interaction potential (or more precisely: Green's function), one can equivalently split the charge distribution. Through the subtraction and subsequent re-addition of a screened charge distribution, we obtain the same result. Let γ be the screening function.

$$\rho = \rho - \rho \otimes \gamma + \rho \otimes \gamma \tag{6.14}$$

In terms of the potential this is equivalent to before, because it is given as the convolution between Green's function and charge distribution,

$$\begin{aligned}
\phi &= \frac{1}{r} \otimes \rho \\
&= \frac{1}{r} \otimes (\rho - \rho \otimes \gamma + \rho \otimes \gamma) \\
&= \frac{1}{r} \otimes \rho - \frac{1}{r} \otimes \gamma \otimes \rho + \frac{1}{r} \otimes \gamma \otimes \rho \\
&= \left(\frac{1}{r} - \frac{1}{r} \otimes \gamma + \frac{1}{r} \otimes \gamma \right) \otimes \rho
\end{aligned}$$

If γ is chosen in the form of a Gaussian,

$$\gamma = \frac{\alpha^3}{\sqrt{\pi^3}} e^{-\alpha^2 r^2},$$

we obtain the same splitting with the error function as in eq (6.12).

Since Poisson's equation is linear, we may write the potential as a sum of two potentials originating from two charge distributions,

$$\phi = \phi_{\rho - \rho \otimes \gamma} + \phi_{\rho \otimes \gamma}. \tag{6.15}$$

This interpretation has the advantage, that it does not require the modification of Green's function with the error function as in eq (6.12). Instead Green's function is still $\frac{1}{r}$ and can be considered a fundamental solution to the Laplacian, which makes it more straight-forward to accommodate for boundary conditions. Moreover, splitting the charge instead of Green's function allows us derive a corresponding Lagrangian, because in contrary to Green's function, the charge appears in (6.1).

The Lagrangian (6.1) must distinguish between both potentials, since they stem from different charge distributions. Starting again from Low's Lagrangian (6.1) we make the following Ansatz,

$$\begin{aligned}
\mathcal{L}(\mathbf{x}, \dot{\mathbf{x}}, \phi_{\rho - \gamma \otimes \rho}, \phi_{\rho \otimes \gamma}) = \int d^3\mathbf{x}_1 d^3\mathbf{v}_1 f(\mathbf{x}_1, \mathbf{v}_1) \ \Big[& \frac{m}{2} \dot{\mathbf{x}}^2(\mathbf{x}_1, \mathbf{v}_1, t) \\
& \Big[- q\phi_{\rho - \gamma \otimes \rho}(\mathbf{x}(\mathbf{x}_1, \mathbf{v}_1, t)) - q\phi_{\rho \otimes \gamma}(\mathbf{x}(\mathbf{x}_1, \mathbf{v}_1, t)) \Big] \\
& + \frac{\varepsilon_0}{2} \int d^3\mathbf{x} \ (\nabla \phi_{\rho - \gamma \otimes \rho})^2 + \frac{\varepsilon_0}{2} \int d^3\mathbf{x} \ (\nabla \phi_{\rho \otimes \gamma})^2.
\end{aligned} \tag{6.16}$$

Since the field energy term is quadratic in the potential, we cannot simply reduce this Lagrangian to its old (non-split) form. In other words, inserting (6.15) into (6.1) does give (6.16). Nevertheless, treating both potentials as separate will lead to two Poisson's equations. In order to motivate the above Ansatz (6.16) we can anticipate that both potentials will in the end fulfil (6.15) again.

To simplify the notation, the following shorthand will be used,

$$\begin{aligned}\phi^L &:= \phi_{\rho\otimes\gamma}\\ \phi^S &:= \phi_{\rho-\rho\otimes\gamma},\end{aligned}$$

where ϕ^S, ϕ^L represent short- and long-ranged potential respectively.
We can again write this in terms of a set of discrete particles, using eq (6.3), where we insert the splitting (6.14) as follows,

$$\begin{aligned}\rho(\mathbf{x}) &= \sum_\alpha \omega_\alpha S_x(\mathbf{x}-\boldsymbol{\xi}_\alpha)\\ &= \sum_\alpha \omega_\alpha (S - S\otimes\gamma)(\mathbf{x}-\boldsymbol{\xi}_\alpha) + (S\otimes\gamma)(\mathbf{x}-\boldsymbol{\xi}_\alpha),\end{aligned}$$

which yields the following Lagrangian,

$$\begin{aligned}\mathcal{L}(\{\boldsymbol{\xi}_\alpha\},\{\dot{\boldsymbol{\xi}}_\alpha\},\phi) =& \sum_\alpha \frac{m}{2}\omega_\alpha \dot{\boldsymbol{\xi}}_\alpha^2 - \sum_\alpha q\omega_\alpha \int d^3\mathbf{x}\ (S - S\otimes\gamma)(\mathbf{x}-\boldsymbol{\xi}_\alpha)\phi^S(\mathbf{x})\\ &+ \sum_\alpha q\omega_\alpha \int d^3\mathbf{x}\ (S\otimes\gamma)(\mathbf{x}-\boldsymbol{\xi}_\alpha)\phi^L(\mathbf{x})\\ &+ \frac{\varepsilon_0}{2}\int d^3\mathbf{x}\ (\nabla\phi^S)^2 + \frac{\varepsilon_0}{2}\int d^3\mathbf{x}\ (\nabla\phi^L)^2\\ =& \mathcal{L}_p + \mathcal{L}^S_{\text{int}} + \mathcal{L}^L_{\text{int}} + \mathcal{L}^S_f + \mathcal{L}^L_f,\end{aligned}$$

where $\mathcal{L}^S_f$, $\mathcal{L}^L_f$ are the field energy terms for the short- and long-ranged potentials. Likewise are $\mathcal{L}^S_{\text{int}}$, $\mathcal{L}^L_{\text{int}}$ the corresponding interaction terms.

In P^3M both potential contributions are calculated differently. In other words, whereas the long-range potential undergoes the entire discretization procedure in the spatial (6.5), (6.7) and temporal (6.9) domain, the short-range part is still dependent on continuous coordinates, as it is not solved on a grid. We can put the long-range part on the grid, using eq (6.5) as described above,

$$\begin{aligned}\mathcal{L}^L_{\text{int}} &= \sum_\alpha q\omega_\alpha \int d^3\mathbf{x}\ (S\otimes\gamma)(\mathbf{x}-\boldsymbol{\xi}_\alpha)\phi^L(\mathbf{x})\\ &= \sum_\alpha q\omega_\alpha \sum_i (\phi^L)_i \int d^3\mathbf{x}\ (S\otimes\gamma)(\mathbf{x}-\boldsymbol{\xi}_\alpha) b_0\left(\frac{\mathbf{x}_i-\mathbf{x}}{\Delta\mathbf{x}}\right)\\ &= \sum_\alpha \sum_i q\omega_\alpha (\phi^L)_i W^L(\mathbf{x}_i-\boldsymbol{\xi}_\alpha),\end{aligned}$$

where we have defined the long-range interpolation function W^L,

$$W^L(\mathbf{x}_i-\boldsymbol{\xi}_\alpha) := \int d^3\mathbf{x}\ (S\otimes\gamma)(\mathbf{x}-\boldsymbol{\xi}_\alpha) b_0\left(\frac{\mathbf{x}_i-\mathbf{x}}{\Delta\mathbf{x}}\right) \tag{6.17}$$

The field energy term can be treated using finite differences (6.6) again,

$$\begin{aligned}\mathcal{L}^L_{\text{int}} &= -\frac{\varepsilon_0}{2}\int d^3\mathbf{x}\ \phi^L\Delta\phi^L \\ &= -\varepsilon_0 h_x h_y h_z \sum_i \sum_j (\phi^L)_i (D_{xyz})_{i;j} (\phi^L)_j.\end{aligned}$$

For the sake of consistency we can also define a short-range "interpolation" function,

$$W^S(\mathbf{x}-\boldsymbol{\xi}_\alpha) = S(\mathbf{x}-\boldsymbol{\xi}_\alpha) - (S\otimes\gamma)(\mathbf{x}-\boldsymbol{\xi}_\alpha), \tag{6.18}$$

which does not actually contain interpolation. This is done for easier notation.

The last step - which affects both potentials equally - is to discretize time using the variational integrator for the leap-frog. The fully temporally and spatially discrete three-point Lagrangian for the P^{3}M method then reads as follows,

$$\begin{aligned}\mathcal{L} =& \sum_\alpha \frac{m}{2}\omega_\alpha \left[\frac{\boldsymbol{\xi}^n_\alpha - \boldsymbol{\xi}^{n-1}_\alpha}{\Delta t}\right]^2 + \sum_\alpha \frac{m}{2}\omega_\alpha \left[\frac{\boldsymbol{\xi}^{n+1}_\alpha - \boldsymbol{\xi}^{n}_\alpha}{\Delta t}\right]^2 \\ &- \sum_\alpha q\omega_\alpha \int d^3\mathbf{x}\ (\phi^S)^{n-1}(\mathbf{x}) W^S(\mathbf{x}-\boldsymbol{\xi}^{n-1}_\alpha) - \sum_\alpha q\omega_\alpha \sum_i (\phi^L)^{n-1}_i W^L(\mathbf{x}_i - \boldsymbol{\xi}^{n-1}_\alpha) \\ &- \sum_\alpha q\omega_\alpha \int d^3\mathbf{x}\ (\phi^S)^{n}(\mathbf{x}) W^S(\mathbf{x}-\boldsymbol{\xi}^{n}_\alpha) - \sum_\alpha q\omega_\alpha \sum_i (\phi^L)^{n}_i W^L(\mathbf{x}_i - \xi^{n}_\alpha) \\ &- \varepsilon_0 h_x h_y h_z \sum_i\sum_j (\phi^L)^{n-1}_i (\Delta^2_{xyz})_{i;j} (\phi^L)^{n-1}_j - \varepsilon_0 \int d^3\mathbf{x}\ (\phi^S)^{n-1}(\mathbf{x})\Delta(\phi^S)^{n-1}(\mathbf{x}) \\ &- \varepsilon_0 h_x h_y h_z \sum_i\sum_j (\phi^L)^{n}_i (\Delta^2_{xyz})_{i;j} (\phi^L)^{n}_j - \varepsilon_0 \int d^3\mathbf{x}\ (\phi^S)^{n}(\mathbf{x})\Delta(\phi^S)^{n}(\mathbf{x}).\end{aligned} \tag{6.19}$$

The Lagrangian depends on sets of particle coordinates, continous fields and sets of field values at grid points,

$$\mathcal{L} = \mathcal{L}(\{\boldsymbol{\xi}^{n-1}\}_\alpha, \{\boldsymbol{\xi}^{n}\}_\alpha, \{\boldsymbol{\xi}^{n+1}\}_\alpha, (\phi^S)^{n-1}, (\phi^S)^n, \{(\phi^L)^n\}_i, \{(\phi^L)^{n-1}\}_i).$$

If we use the discrete Euler-Lagrange equations (6.10) with the above Lagrangian (6.19) for the variables $\boldsymbol{\xi}^k_\beta$, $(\phi^S)^k$, $(\phi^L)^k_m$ we obtain the equation of motion describing the particles, as well as a Poisson equation for each potential,

$$\begin{aligned}\omega_\beta m\left[\frac{\boldsymbol{\xi}^{k+1}_\beta + \boldsymbol{\xi}^{k-1}_\beta - 2\boldsymbol{\xi}^k_\beta}{\Delta t^2}\right] &= -\sum_i \omega_\beta q_\beta \frac{dW^L}{d\xi}(\mathbf{x}_i - \boldsymbol{\xi}^k_\beta)(\phi^L)^k_i \\ &\quad - \omega_\beta q_\beta \int d^3\mathbf{x}\ \frac{dW^S}{d\xi}(\mathbf{x}-\boldsymbol{\xi}^k_\beta)(\phi^S)^k(\mathbf{x}),\end{aligned} \tag{6.20a}$$

$$\varepsilon_0 h_x h_y h_z \sum_j (D_{xyz})_{m;j}(\phi^L)^k_j = -\sum_\alpha \omega_\alpha q W^L(\mathbf{x}_m - \boldsymbol{\xi}^k_\alpha), \tag{6.20b}$$

$$\varepsilon_0 \nabla^2(\phi^S)^k(\mathbf{x}) = -q\sum_\alpha \omega_\alpha q_\alpha W^S(\mathbf{x}-\boldsymbol{\xi}^k_\alpha) = [\rho^k - \rho^k\otimes\gamma](\mathbf{x}). \tag{6.20c}$$

At this point it is clear, that self-energy does not contribute to the equations of motion as it is per definition independent of the particle position and vanishes through the derivative in the Euler-Lagrange equations (6.10). Hence, we make no mistake by omitting it from the start.

These microscopic equations (6.20a), (6.20b) and (6.20c) can be connected to the macroscopic distribution function through Klimontovich's averaged equation (5.1), since the phase space is the same. In this picture, collisional effects arise due to the interaction of particles with local electric field fluctuations,

$$\left(\frac{\partial f}{\partial t}\right)_{\text{coll}} = -\frac{q}{m}\left\langle \delta\mathbf{E}\nabla_v \delta f\right\rangle .$$

In P^3M the situation is similar, as the second term in eq (6.20a) represents the interaction of the particle with the near-field, which arises due to the sub-mesh granularity of the charge distribution. It becomes clear, that the short-ranged interaction plays the role of a collision operator.

As for correlation effects, we can see from the second term of eq (6.20a) that all immediately surrounding particles contribute to the interaction. Since there are no assumptions regarding the scattering angle, or the amount of colliding particles per collision, this method includes correlation effects naturally.

The only criterion is that the Ewald parameter α needs to be chosen in such way, that the cut-off radius coincides well with the correlation length, i.e. that all non-negligible correlations are included in the short-range potential. In the spirit of effective potential theory the correlation length can be interpreted as the reach of the effective interaction potential and can be calculated using the hyper netted chain approach, as presented in chapter 2. In figure 6.1, one can see that the prediction of Debye-Hueckel theory is too low for strongly coupled configurations. The common practice of choosing α such that the Ewald-Sphere coincides with the Debye sphere causes an underestimation of correlation effects.

Additionally, one can see that the correlation length initially decreases with decreasing temperature but at lower temperatures starts rising again, if the coupling is strong. As illustrated in figure 6.2 this behaviour persists scaling and is likely due to increasing "stiffness" in the particle configuration.

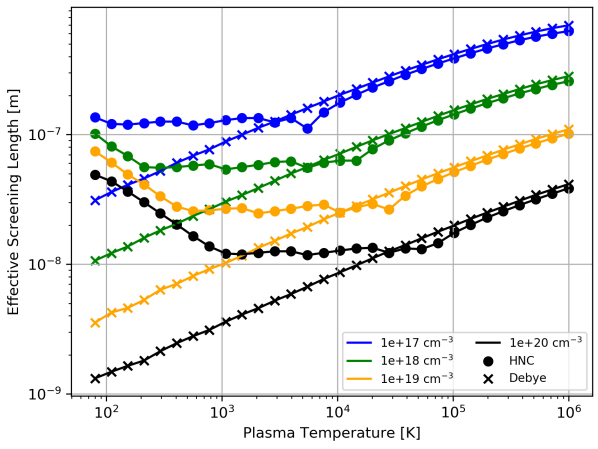

Figure 6.1: The correlation length for various combinations of density and temperature, as predicted by the Ornstein-Zernike equation with hyper netted chain closure (HNC) and by Debye-Hueckel theory.

In summary: the stronger the coupling factor is, the more particles are correlated and the larger the Ewald sphere needs to be. From figure 6.2 one can see, that the sphere radius may certainly not be lower than ten times the Wigner-Seitz radius.

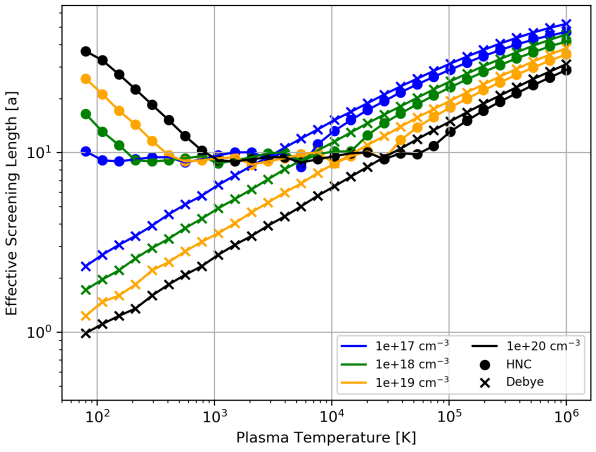

Figure 6.2: The same as in figure 6.1 but the length is scaled to units of the Wigner Seitz radius.

6.4 Interplay with Boundary Conditions

Since the splitting (6.14) does not directly affect Green's function, we can still solve both Poisson's equations (6.20b), (6.20c) using standard methods. However, the potentials will need to be solved with different Green functions, since ϕ^L is discrete and ϕ^S is not. This means we need to distinguish Green's functions G^L, G^S for both ranges and make use of the finite convolution $\otimes_d$ for the long range.

From eqns (6.20b), (6.20c), we can define the charge distributions ρ^L, ρ^S, corresponding to ϕ^L, ϕ^S as follows,

$$(\rho^L)^n_k = -\sum_\alpha \omega_\alpha q W^L(\mathbf{x}_k - \boldsymbol{\xi}^n_\alpha), \tag{6.21a}$$

$$(\rho^S)^n = -q\sum_\alpha \omega_\alpha q_\alpha W^S(\mathbf{x} - \boldsymbol{\xi}^n_\alpha), \tag{6.21b}$$

where again n denotes a temporal index and k a spatial multi-index. The solutions to eqns (6.20b), (6.20c) are then given as,

$$\begin{aligned}(\phi^L)^n_k &= \left[(\rho^L)^n \otimes_d G^L\right](\mathbf{x}_k)\\ &= \frac{h_x h_y h_z}{\varepsilon_0}\sum_q (\rho^L)^n(\mathbf{x}_q) G^L(\mathbf{x}_k - \mathbf{x}_q)\end{aligned} \tag{6.22a}$$

$$\begin{aligned}(\phi^S)^n(\mathbf{x}) &= ((\rho^S)^n \otimes G^S)(\mathbf{x}),\\ &= \frac{1}{\varepsilon_0}\int d^3\mathbf{z}\ (\rho^S)^n(\mathbf{z}) G^S(\mathbf{x} - \mathbf{z}).\end{aligned} \tag{6.22b}$$

The defining equations for Green's function refer to the discrete and continuous Laplacian respectively,

$$\begin{aligned}(D_{xyz})_{klm}(G^L)_{klm;k'l'm'} &= \delta_{kk'}\delta_{ll'}\delta_{mm'},\\ \Delta_{\mathbf{x}}(G^S)(\mathbf{x} - \mathbf{y}) &= \delta^{(3)}(\mathbf{x} - \mathbf{y}).\end{aligned}$$

Ultimately, both potentials together should approximate the true potential in the best way possible for any given boundary conditions. The main problem is, that the short-ranged potential ϕ^S is never actually calculated. Instead the algorithm prescribes that the pairwise interaction is summed up directly, which becomes non-trivial as soon as the potential should adhere to boundaries. In other words, setting $G^S \neq 1/r$ requires that the coordinate space term in Ewalds summation formula (6.13) needs to be changed. If we choose to ignore this and sum up the free interaction, as it is usually done, the potential will be erroneous.

The following calculations serve the purpose of investigating this error.

Green's Function for a Planar Cathode

The electrostatic boundary value problem is given by Poisson's equation and a boundary value condition for a Volume V in coordinate space,

$$\begin{aligned} \Delta\phi(\mathbf{x}) &= \frac{\rho(\mathbf{x})}{\varepsilon_0} \qquad \text{for } \mathbf{x} \in V \\ \phi(\mathbf{x}) &= 0 \qquad \text{for } \mathbf{x} \in \partial V, \end{aligned}$$

which is solved by a suitable Green's function. Green's function is defined as a smooth harmonic function that fulfils the boundary condition and is a fundamental solution to the Laplacian everywhere else. Formally, these constraints read,

$$\begin{aligned} \Delta G(\mathbf{x}-\mathbf{y}) &= \delta^{(3)}(\mathbf{x}-\mathbf{y}) \qquad \text{for } \mathbf{x} \in V, \\ G(\mathbf{x}-\mathbf{y}) &= 0 \qquad \text{for } \mathbf{x} \in \partial V. \end{aligned}$$

The "free" choice $G^F(\mathbf{r}) = \frac{1}{|\mathbf{r}|}$ (where $\mathbf{r} = \mathbf{x}-\mathbf{y}$) refers to the "free" boundary condition $G^F(\mathbf{r}) \overset{r\to\infty}{\longrightarrow} 0$. With a correction function G^C one can apply the modification $G(r) \to G(r) - G^C(r)$ to enforce Dirichlet's condition as above, if the correction fulfils the following conditions,

$$\begin{aligned} G^C(\mathbf{x}-\mathbf{y}) &= 0 \qquad \text{for } \mathbf{x} \in V \\ G^C(\mathbf{x}-\mathbf{y}) &= G(\mathbf{x}-\mathbf{y}) \quad \text{for } \mathbf{x} \in \partial V. \end{aligned}$$

For certain geometries, this correction can be found by interpreting it as the influence of oppositely charged mirror images of the original charges [108, 109]. The limitations of this approach are expanded upon in appendix E.

For the sake of argument, let us consider the case of a planar cathode at $z = 0$, which is depicted in figure 6.4. The correction function reads as follows,

$$G^C(\mathbf{x}, \mathbf{y}) = G^F(\mathbf{x}, S(\mathbf{y})), \tag{6.23}$$

where $S : \mathbb{R}^3 \to \mathbb{R}^3$ is the mirror symmetry map,

$$S(x, y, z) = (x, y, -z). \tag{6.24}$$

This means the Green's function that accommodates for the boundary at $z = 0$ is given as,

$$G(\mathbf{x}-\mathbf{y}) = G^F((\mathbf{x}-\mathbf{y})) - G^F(\mathbf{x} - S(\mathbf{y})).$$

Numerically, the issue with this technique is that the location of the mirror image must be part of the computational domain. In other words, the entire distance between charge and image must be resolved as well. This is leads to poorer resolution and higher computational cost.

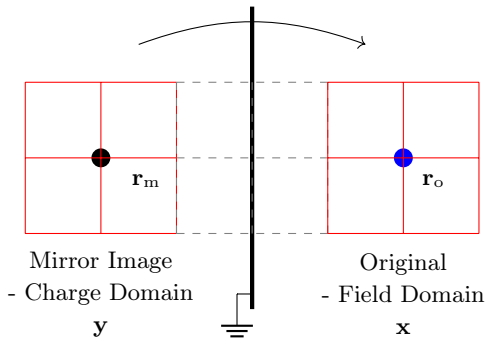

Figure 6.3: Illustration of the planar Green's function. Thanks to the decoupling of charge and field domain, the entire (dashed) space in between does not need to be resolved. $\mathbf{r}_m$ and $\mathbf{r}_o$ denote the position of image and original respectively.

As demonstrated by Qiang *et al.* [110], one can reduce the work load by shifting Green's function (see figure 6.4). This method decouples the location of the image (charge domain) from the location where its field is calculated (field domain). If Green's function is denoted as $G(\mathbf{x}, \mathbf{y})$, then $\mathbf{x}$ lies in the field domain and $\mathbf{y}$ in the charge domain. If we denote with $\mathbf{r}_o$ the location of the original charge, we can shift Green's function, which reduces the domain needed for $\mathbf{x}$. Everything together, the correction functions is given as,

$$G^C(\mathbf{x}, \mathbf{y}) = G^F(\mathbf{x} + \mathbf{r}_o, S(\mathbf{y})).$$

Potential Error due to Free Short-Range Function

Having established the Green function formalism, we can proceed to quantify the error invoked by neglecting the boundary condition in the short range.

Let Φ be the true potential for a given geometry that is to be approximated. It can be denoted as the convolution between the analytic Green function R for this geometry and the total continuous charge distribution,

$$\Phi(\mathbf{x}) = R \otimes \rho = \frac{q}{\varepsilon_0} \int d^3\mathbf{y}\ R(\mathbf{x} - \mathbf{y}) \sum_\alpha \omega_\alpha S_x(\mathbf{y} - \boldsymbol{\xi}_\alpha).$$

The total computed potential using P^{3}M will be denoted as ϕ^{tot}. It can be put together by adding eqns (6.22a) and (6.22b) and insert from eqns (6.21a), (6.21b). Additionally, the long-range part needs to be re-interpolated, using W^L again,

$$\phi^{\mathrm{tot}} = \frac{1}{\varepsilon_0} \sum_\alpha \omega_\alpha \left[\int d^3\mathbf{z}\ W^S(\mathbf{z} - \boldsymbol{\xi}_\alpha^n) G^S(\mathbf{x} - \mathbf{z}) + \sum_{q,k} W^L(\mathbf{x}_q - \boldsymbol{\xi}_\alpha) G^L(\mathbf{x}_k - \mathbf{x}_q) W^L(\mathbf{x} - \mathbf{x}_k) \right].$$

For a more general picture, we can remove the fixed charge distribution and instead write the dependence on the charge position explicitly. The potentials depend on charge position $\boldsymbol{\xi}$ and are evaluated at $\mathbf{x}$, i.e. they determine the potential value at $\mathbf{x}$ due to one particle at $\boldsymbol{\xi}$. For the sake of simplicity, we set $\omega = 1$, so the potentials are given as follows,

$$\Phi(\mathbf{x},\boldsymbol{\xi}) = \frac{q}{\varepsilon_0}\int d^3\mathbf{y}\ R(\mathbf{x}-\mathbf{y})S_x(\mathbf{y}-\boldsymbol{\xi})$$
$$\phi^{\mathrm{tot}}(\mathbf{x},\boldsymbol{\xi}) = \frac{q}{\varepsilon_0}\int d^3\mathbf{y}\ G^S(\mathbf{x}-\mathbf{y})W^S(\mathbf{y}-\boldsymbol{\xi}) + \frac{q}{\varepsilon_0}\sum_{q,k} W^L(\mathbf{x}_q-\boldsymbol{\xi})G^L(\mathbf{x}_k-\mathbf{x}_q)W^L(\mathbf{x}-\mathbf{x}_k)$$

A statement about the overall error of this method is difficult to make, as there are interdependent contributions from discretization, interpolation and finite differencing. In addition the difference between ϕ^{tot} and Φ depends on the position and the amount of charges present. An error measure that captures the overall deviation can be found by integrating, as proposed by Hockney and Eastwood [16], over both degrees of freedom. Let us denote the error measure by E,

$$E = \int d^3\boldsymbol{\xi}\int d^3\mathbf{x}\ |\phi^{\mathrm{tot}}(\mathbf{x},\boldsymbol{\xi}) - \Phi(\mathbf{x},\boldsymbol{\xi})|^2$$

In order to quantify the error made by summing the short-range contributions with the free interaction potential, we can assume that the total error is dominated by the short-range error. If the long-range part approximates the continuous case well, then this assumption holds. The error reads,

$$E = \int d^3\boldsymbol{\xi}\int d^3\mathbf{x}\ |\phi^S(\mathbf{x},\boldsymbol{\xi}) - \Phi^S(\mathbf{x},\boldsymbol{\xi})|^2,$$

where,

$$\Phi^S(\mathbf{x},\boldsymbol{\xi}) = q\int d^3\mathbf{y}\ R(\mathbf{x}-\mathbf{y})\omega(S_x - S_x\otimes\gamma)(\mathbf{y}-\boldsymbol{\xi}) = q\int d^3\mathbf{y}\ G^S(\mathbf{x}-\mathbf{y})\omega W^S(\mathbf{y}-\boldsymbol{\xi}),$$

denotes the true short-range potential. For illustration we assume the case of a planar cathode, which implies that the difference between the Green functions is exactly the image charge contribution. Furthermore, we can consider point charges $S=\delta$ to get the following,

$$\begin{aligned}
E &= \int d^3\mathbf{x}\int d^3\boldsymbol{\xi}\ \left|\int d^3\mathbf{y}\ \left[\omega(\boldsymbol{\xi})W^S(\mathbf{y}-\boldsymbol{\xi})\right]\left(\frac{1}{|\mathbf{x}-\mathbf{y}|} - R(\mathbf{x}-\mathbf{y})\right)\right|^2 \\
&= \int d^3\mathbf{x}\int d^3\boldsymbol{\xi}\ \left|\int d^3\mathbf{y}\ \left[\omega(\boldsymbol{\xi})W^S(\mathbf{y}-\boldsymbol{\xi})\right]\frac{1}{|\mathbf{x}-S(\mathbf{y})|}\right|^2 \\
&= \int d^3\mathbf{x}\int d^3\boldsymbol{\xi}\ \left|\int d^3\mathbf{y}\ \omega(\boldsymbol{\xi})\left[S_x(\mathbf{y}-\boldsymbol{\xi}) - (S_x\otimes\gamma)(\mathbf{y}-\boldsymbol{\xi})\right]\frac{1}{|\mathbf{x}-S(\mathbf{y})|}\right|^2 \\
&= \int d^3\mathbf{x}\int d^3\boldsymbol{\xi}\ \left|\int d^3\mathbf{y}\ \left[\delta(\mathbf{y}-\boldsymbol{\xi}) - \gamma(\mathbf{y}-\boldsymbol{\xi})\right]\frac{1}{|\mathbf{x}-S(\mathbf{y})|}\right|^2 \\
&= \int d^3\mathbf{x}\int d^3\boldsymbol{\xi}\ \left|\frac{1}{|\mathbf{x}-S(\boldsymbol{\xi})|} - \int d^3\mathbf{y}\frac{\gamma(\mathbf{y}-\boldsymbol{\xi})}{|\mathbf{x}-S(\mathbf{y})|}\right|^2.
\end{aligned}$$

The action of the mirror charge onto the original charge location is equivalent to the action of the original charge to the mirror charge domain. Hence, we can rewrite this expression,

$$
\begin{aligned}
E &= \int d^3\mathbf{x} \int d^3\boldsymbol{\xi} \left| \frac{1}{|S(\mathbf{x}) - \boldsymbol{\xi}|} - \int d^3\mathbf{y} \frac{\gamma(\mathbf{y} - \boldsymbol{\xi})}{|S(\mathbf{x}) - \mathbf{y}|} \right|^2 \\
&= \int d^3\mathbf{x} \int d^3\boldsymbol{\xi} \left| \frac{1}{|S(\mathbf{x}) - \boldsymbol{\xi}|} - \int d^3\mathbf{y} \frac{\gamma(\mathbf{y})}{|(S(\mathbf{x}) - \boldsymbol{\xi}) - \mathbf{y}|} \right|^2 \\
&= \int d^3\mathbf{x} \int d^3\boldsymbol{\xi} \left| \frac{\mathrm{Erfc}(\alpha|S(\mathbf{x}) - \boldsymbol{\xi}|)}{|S(\mathbf{x}) - \boldsymbol{\xi}|} \right|^2 \\
&= \int d^3\mathbf{x} \int d^3\boldsymbol{\xi} \left| \frac{\mathrm{Erfc}(\alpha|\mathbf{x} - S(\boldsymbol{\xi})|)}{|\mathbf{x} - S(\boldsymbol{\xi})|} \right|^2 \\
&> \left| \int d^3\mathbf{x} \int d^3\boldsymbol{\xi} \, \frac{\mathrm{Erfc}(\alpha|\mathbf{x} - S(\boldsymbol{\xi})|)}{|\mathbf{x} - S(\boldsymbol{\xi})|} \right|^2 .
\end{aligned}
$$

This means that the error committed is equal to the integral of the short-range potential from the corresponding mirror charge. Due to the strong decay of the complementary error function, the error is strongly confined. If we restrict the integration to the original charge domain and require that the image charge is sufficiently far away from the original, the error is nil. Consequentially, only if a particle is within half the Ewald cut-off length to the cathode, the error (within the computational domain) will be non-vanishing as can be seen in figure 6.4.

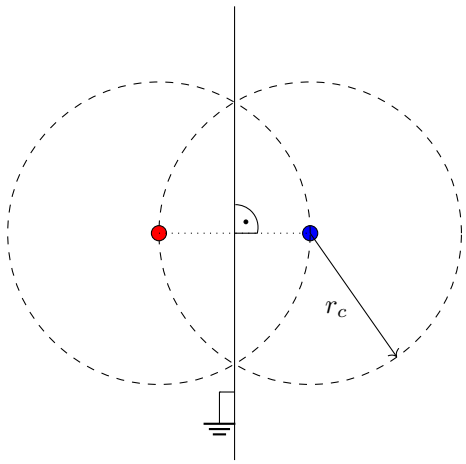

Figure 6.4: When r_c denotes the cut-off radius of the method, only particles closer than $\frac{r_c}{2}$ to the cathode are affected by the boundary condition.

For any other geometry, we may infer that although the value will be different, the boundedness will be the same, as it arises due to the charge screening. For illustration, one can consider the long- (6.20b) and short-ranged (6.20c) Poisson equations as continuous:

$$
\begin{aligned}
\varepsilon_0 \nabla^2 \phi^S &= \rho - \rho \otimes \gamma \\
\varepsilon_0 \nabla^2 \phi^L &= \rho \otimes \gamma .
\end{aligned}
$$

The argument, why the above result may be generalized, is that the screening is independent of the geometry. By solving both equations with the same boundary conditions, we essentially solve the same problem twice, but on different length scales. Instead, one can solve both equations

separately, with and without a boundary condition respectively. The error, as has been shown above, is negligible. A visualization of the short-ranged potential can be seen in figure 6.5, which illustrates that boundary conditions have no impact in the short range. For the long-ranged potential, as depicted in figure 6.6, the boundaries do influence the potential. In figure 6.7 the solution of the unaltered Poisson's equation is shown, which coincides well with the sum of short- and long-ranged potential.

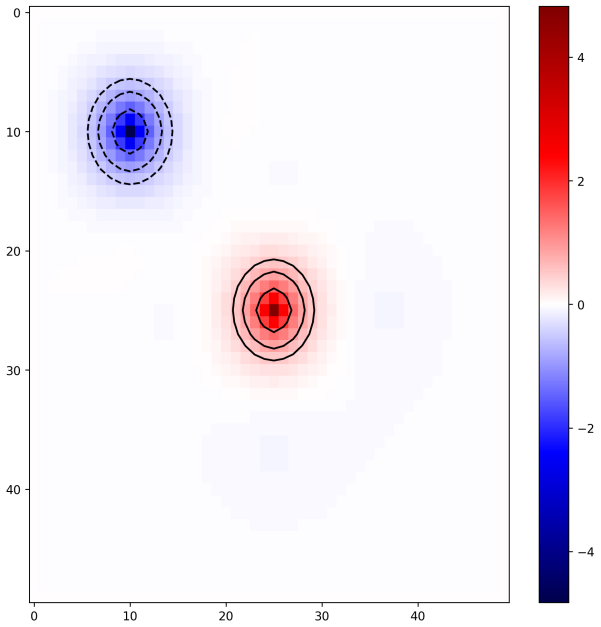

Figure 6.5: Solution of the short-ranged Poisson equation in a box with Dirichlet condition for two point charges, using a Gauss-Seidel solver.

Total Potential Constraint with Analytic Short-Range Function

The following derivation closely follows the derivation of Hockney & Eastwood [16].

In the above calculation, it was assumed that the long-range *computed* potential perfectly approximates reality, and that the error was predominantly coming from the short-ranged part. The existence of such a perfect approximation will be shown in the following section. With regard to optimizing the long-range part, the calculations become easier if we use $G^S = R$. The optimization condition reads as follows,

$$\frac{\delta}{\delta G^L_{klm;k'l'm'}} \int d^3\boldsymbol{\xi} \int d^3\mathbf{x}\ |\phi^{\mathrm{tot}}(\mathbf{x},\boldsymbol{\xi}) - \Phi(\mathbf{x},\boldsymbol{\xi})|^2 \stackrel{!}{=} 0.$$

The form of the potentials and the many integrations makes this derivative difficult to evaluate, but one can simplify the calculation by transforming to Fourier space. For the continuous parts, this poses no challenge. If we denote a Fourier space vector with $\mathbf{k}$ the transforms read,

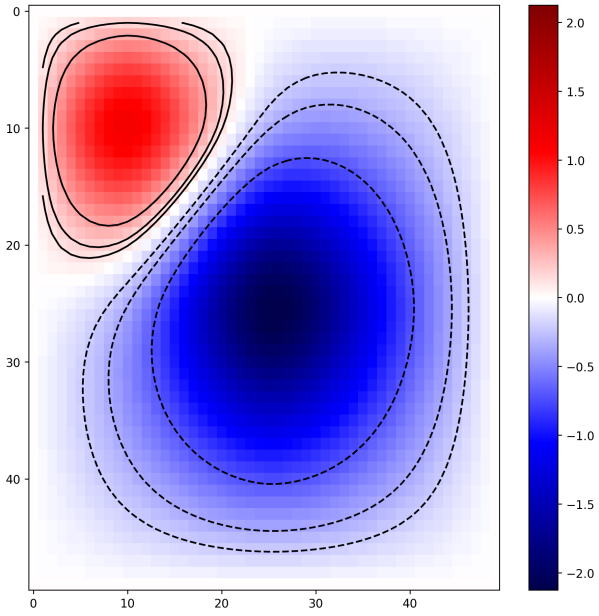

Figure 6.6: Solution of the long-ranged Poisson equation in a box with Dirichlet condition for two point charges, using a Gauss-Seidel solver.

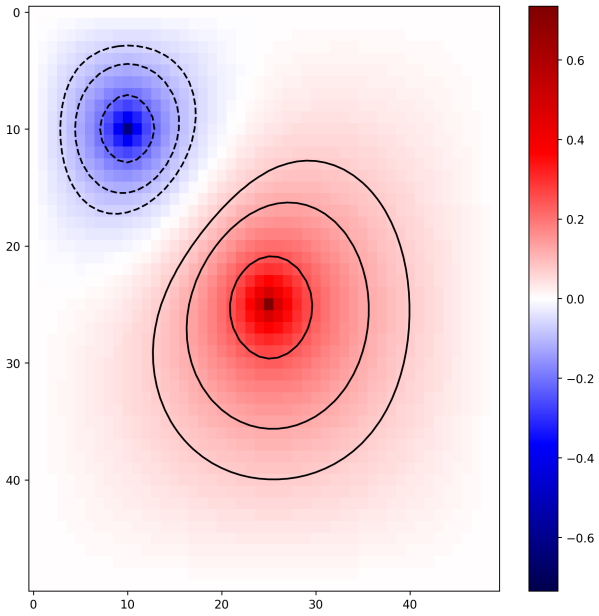

Figure 6.7: Solution of the total Poisson equation in a box with Dirichlet condition for two point charges, using a Gauss-Seidel solver.

$$\hat{\Phi}(\mathbf{k}) = q\frac{1}{\varepsilon_0}\sum_{\alpha}\omega_\alpha \hat{R}(\mathbf{k})\hat{S}_x(\mathbf{k})e^{-i\mathbf{k}\boldsymbol{\xi}_\alpha} \tag{6.25a}$$

$$\hat{\phi}^S(\mathbf{k}) = \frac{1}{\varepsilon_0}\sum_{\alpha}\omega_\alpha \hat{W}^S(\mathbf{k})\hat{R}(\mathbf{k})e^{-i\mathbf{k}\boldsymbol{\xi}_\alpha}. \tag{6.25b}$$

The long-range potential is the result of a discrete convolution, which transform to the product of Fourier series coefficients,

$$\begin{aligned}\mathcal{F}[(\phi^L)^n_k](\mathbf{m}) &= \mathcal{F}\left[\sum_q \overbrace{\left\{\sum_\alpha W^L(\mathbf{x}_q - \boldsymbol{\xi}^n_\alpha)\right\}}^{(\rho^L)^n_q} G^L(\mathbf{x}_k - \mathbf{x}_q)\right] \\ &= (\hat{\rho}^L)^n(\mathbf{m}) \cdot \hat{G}^L(\mathbf{m})\end{aligned}$$

Note that $\mathbf{m}$ is a reciprocal lattice vector, which means this representation is defined on the lattice only and not continuous like $\mathbf{k}$. In order to be able to compare to the continuous transforms, we rewrite the discrete convolution using a *Dirac comb*,

$$\text{Ш}_{h_x}(x) = \sum_{k=-\infty}^{\infty} \delta(x - kh_x).$$

In three dimensions this generalizes to the corresponding product,

$$\text{Ш}(\mathbf{x}) = \text{Ш}_{h_x}(x)\text{Ш}_{h_y}(y)\text{Ш}_{h_z}(z).$$

The corresponding Fourier transform is a Dirac comb with the period of the reciprocal lattice.,

$$\widehat{\text{Ш}}_{2\pi/h_x}(k_x) = \sum_{n=-\infty}^{\infty} \delta(k_x - n2\pi/h_x).$$

Using this, the discrete convolution in eq (6.22a) can be written in continuous form, assuming we know the continuous form of G^L and W^L, which is usually the case but can be readily obtained by making the grid constants infinitely small. The result is a continuous function $(\tilde{\phi}^L)^n$ that reproduces the meshed potential at grid points,

$$\begin{aligned}(\tilde{\phi}^L)^n(\mathbf{x}) &= \int d^3\mathbf{y}_1 \; W^L(\mathbf{y}_1 - \boldsymbol{\xi}^n_\alpha)\text{Ш}(\mathbf{y}_1)G^L(\mathbf{x} - \mathbf{y}_1) \\ (\tilde{\phi}^L)^n(\mathbf{x}_k) &= (\phi^L)^n_k.\end{aligned}$$

The re-interpolated long-range potential is given as the convolution with the interpolation function,

$$(\phi^L)^n(\mathbf{x}) = (W \otimes (\tilde{\phi}^L)^n)(\mathbf{x}) \tag{6.26}$$

The continuous Fourier transform of (6.26) can then be readily calculated,

$$\widehat{(\tilde{\phi}^L)^n}(\mathbf{k}) = (\widehat{W}^L \otimes \text{Ш}_{(2\pi/h)})(\mathbf{k})\widehat{G}e^{-i\mathbf{k}\boldsymbol{\xi}^n_\alpha}.$$

The convolution can be evaluated directly. Let $\mathbf{n} \in \mathbb{N}^3$ denote a vector of integers,

$$\begin{aligned}\widehat{\widetilde{W}}^L \otimes \text{Ш}_{(2\pi/h)}(\mathbf{k}) &= \int d^3\,\mathbf{q} \sum_{\mathbf{n}} \delta(\mathbf{k}_x - n_x 2\pi/h_x)\delta(\mathbf{k}_y - n_y 2\pi/h_y)\delta(\mathbf{k}_z - n_z 2\pi/h_z)W(\mathbf{k}) \\ &= \sum_{\mathbf{n}} \widehat{W}^L\left[\mathbf{k} - 2\pi(n_x/h_x, n_y/h_y, nz/h_z)\right] \\ &=: \sum_{\mathbf{n}} \widehat{W}^L\left[\mathbf{k} - \frac{2\pi}{h}\mathbf{n}\right]\end{aligned}$$

The sum can be identified as aliasing sum [16]. It describes the influence of the aliases of the principal harmonic of the charge distribution, i.e. every harmonic that is periodically shifted to the original. Basically, it arises due to the sampling onto the mesh that is done during the charge assignment and as such it is the price paid for a discrete description.

Now the corresponding continuous Fourier representation of the long-range potential looks as follows,

$$\begin{aligned}(\widehat{\phi^L})^n(\mathbf{k}) &= \widehat{W}^L(\mathbf{k})\widehat{(\tilde{\phi}^L)}^n(\mathbf{k}) \\ &= \widehat{W}^L(\mathbf{k})\hat{G}(\mathbf{k})\sum_{\mathbf{n}}\widehat{W}^L\left[\mathbf{k}-\frac{2\pi}{h}\mathbf{n}\right]e^{-i\mathbf{k}\boldsymbol{\xi}^n_\alpha}\end{aligned}$$

The total potential thus has the following form,

$$\phi^{\text{tot}}(\mathbf{x}) = \sum_\alpha\sum_{\mathbf{k}}\left[\hat{W}^S(\mathbf{k})\hat{G}^S(\mathbf{k})e^{i\mathbf{k}\boldsymbol{\xi}^n_\alpha} + \widehat{W}^L(\mathbf{k})\hat{G}(\mathbf{k})\sum_{\mathbf{n}}\widehat{W}^L\left[\mathbf{k}-\frac{2\pi}{h}\mathbf{n}\right]e^{-i(\mathbf{k}-2\pi\mathbf{n}/h)\boldsymbol{\xi}^n_\alpha} - \hat{R}(\mathbf{k})\hat{S}_x(\mathbf{k})e^{i\mathbf{k}\boldsymbol{\xi}^n_\alpha}\right]e^{-i\mathbf{k}\mathbf{x}}.$$

By omitting the the sum over particles α, we can again rewrite this to the potential caused by one particle at $\boldsymbol{\xi}$,

$$\phi^{\text{tot}}(\mathbf{x},\boldsymbol{\xi}) = \sum_{\mathbf{k}}\left[\hat{W}^S(\mathbf{k})\hat{G}^S(\mathbf{k})e^{i\mathbf{k}\boldsymbol{\xi}^n} + \widehat{W}^L(\mathbf{k})\hat{G}(\mathbf{k})\sum_{\mathbf{n}}\widehat{W}^L\left[\mathbf{k}-\frac{2\pi}{h}\mathbf{n}\right]e^{-i(\mathbf{k}-2\pi\mathbf{n}/h)\boldsymbol{\xi}^n} - \hat{R}(\mathbf{k})\hat{S}_x(\mathbf{k})e^{i\mathbf{k}\boldsymbol{\xi}^n}\right]e^{-i\mathbf{k}\mathbf{x}}.$$

In addition, potentials depend only on absolute distance values, hence it makes sense to write a dependence on the particle position and the distance from it. We denote $\mathbf{r} = \mathbf{x} - \boldsymbol{\xi}^n$, which yields,

$$\phi^{\text{tot}}(\mathbf{r},\boldsymbol{\xi}) = \sum_{\mathbf{k}}\left[\hat{W}^S(\mathbf{k})\hat{G}^S(\mathbf{k})e^{i\mathbf{k}\boldsymbol{\xi}^n} + \widehat{W}^L(\mathbf{k})\hat{G}(\mathbf{k})\sum_{\mathbf{n}}\widehat{W}^L\left[\mathbf{k}-\frac{2\pi}{h}\mathbf{n}\right]e^{-i(\mathbf{k}-2\pi\mathbf{n}/h)\boldsymbol{\xi}^n+i\mathbf{k}\boldsymbol{\xi}^n} - \hat{R}(\mathbf{k})\hat{S}_x(\mathbf{k})e^{i\mathbf{k}\boldsymbol{\xi}^n}\right]e^{-i\mathbf{k}\mathbf{r}}.$$

The Fourier transform can be read off,

$$\phi^{\text{tot}}(\mathbf{k},\boldsymbol{\xi}) = \left[\hat{W}^S(\mathbf{k})\hat{G}^S(\mathbf{k})e^{i\mathbf{k}\boldsymbol{\xi}^n} + \widehat{W}^L(\mathbf{k})\hat{G}(\mathbf{k})\sum_{\mathbf{n}}\widehat{W}^L\left[\mathbf{k}-\frac{2\pi}{h}\mathbf{n}\right]e^{-i(\mathbf{k}-2\pi\mathbf{n}/h)\boldsymbol{\xi}^n+i\mathbf{k}\boldsymbol{\xi}^n} - \hat{R}(\mathbf{k})\hat{S}_x(\mathbf{k})e^{i\mathbf{k}\boldsymbol{\xi}^n}\right],$$

We can then propose the following minimization condition analogous to the above, while remembering that Φ and ϕ^S are independent of G^L:

$$\hat{E} = \frac{\delta}{\delta(\widehat{G}^L)(\mathbf{k})}\int d^3\boldsymbol{\xi}\ \left|\phi^{\text{tot}}(\mathbf{k},\boldsymbol{\xi}) - \Phi(\mathbf{k})\right|^2 = \int d^3\boldsymbol{\xi}\ 2\left|\phi^{\text{tot}}(\mathbf{k},\boldsymbol{\xi}) - \Phi(\mathbf{k})\right|\frac{\delta\phi^L(\mathbf{k},\boldsymbol{\xi})}{\delta(\widehat{G}^L)(\mathbf{k})} \stackrel{!}{=} 0.$$

We can resolve the integral over $\boldsymbol{\xi}$ to obtain $\delta(\mathbf{k}-(\mathbf{k}-2\pi\mathbf{n}/h))$ and solve for $\hat{G}^L$, while keeping in mind that $\hat{G}^L$ is a periodic function in $\mathbf{k}$-space. For simplicity, we will set $\hat{G}^S = \hat{R}$ to get the following,

$$\begin{aligned}\hat{E} &= \sum_{\mathbf{n}}\widehat{W^L}^2\left[\mathbf{k}-\frac{2\pi}{h}\mathbf{n}\right]\left[\hat{G}^L(\mathbf{k})\sum_{\mathbf{n}}\widehat{W^L}^2\left[\mathbf{k}-\frac{2\pi}{h}\mathbf{n}\right] - \hat{R}\left[\mathbf{k}-\frac{2\pi}{h}\mathbf{n}\right](\hat{S}_x - \hat{W}^S)\left[\mathbf{k}-\frac{2\pi}{h}\mathbf{n}\right]\right] \\ &= \hat{G}^L(\mathbf{k})\left|\sum_{\mathbf{n}}\widehat{W^L}^2\left[\mathbf{k}-\frac{2\pi}{h}\mathbf{n}\right]\right|^2 - \sum_{\mathbf{n}}\widehat{W^L}^2\left[\mathbf{k}-\frac{2\pi}{h}\mathbf{n}\right]\hat{R}\left[\mathbf{k}-\frac{2\pi}{h}\mathbf{n}\right](\hat{S}_x - \hat{W}^S)\left[\mathbf{k}-\frac{2\pi}{h}\mathbf{n}\right]\end{aligned}$$

This leads to the following expression,

$$\hat{G}^L(\mathbf{k}) = \frac{\sum_{\mathbf{n}} \widehat{W^L}^2 \left[\mathbf{k} - \frac{2\pi}{h}\mathbf{n}\right] \hat{R} \left[\mathbf{k} - \frac{2\pi}{h}\mathbf{n}\right] \left(\hat{S}_x - \hat{W}^S\right) \left[\mathbf{k} - \frac{2\pi}{h}\mathbf{n}\right]}{\left|\sum_{\mathbf{n}} \widehat{W^L}^2 \left[\mathbf{k} - \frac{2\pi}{h}\mathbf{n}\right]\right|^2}$$

Per definition (6.17), (6.18), the Fourier transforms of the interpolation functions, are given as follows,

$$\hat{W}^S = \hat{S}_x - \hat{S}_x\hat{\gamma}$$
$$\hat{W}^L = \hat{S}_x\hat{\gamma}\hat{b}_0,$$

therefore all aliasing sums contain a decaying factor $\hat{\gamma}(\mathbf{k}) = e^{-k^2/(4\alpha^2)}$. If mesh-size and Ewald-sphere are chosen sufficiently small [104], we can only keep the principal harmonic $\mathbf{n} = 0$.

$$\hat{G}^L(\mathbf{k}) = \frac{\hat{R}\hat{S}_x\hat{\gamma}}{\left(\hat{S}_x\hat{\gamma}\hat{b}_0\right)^2} = \hat{R} \cdot \frac{1}{\hat{\gamma}\hat{S}_x\hat{b}_0^2}$$

This results shows, that the assumed minimum exists.

In conclusion, it was proven that,

$$G^L \text{ is a good approximation} \iff G^S = \frac{1}{r} \text{ is a good approximation,}$$

which means that the only error committed is the error of the long-range function.

Chapter 7

Statistical Description of Collision Dynamics

This chapter reviews a branch of models which employ statistical treatment to account for collision dynamics. In rough terms the main idea is to consider collisions as rotations of particle velocity vectors and to choose the rotation angles statistically.

7.1 Random binary Collisions

For a collision between two particles of identical mass, we can define the centre of mass velocity $\mathbf{v}_{\mathrm{COM}} = (\mathbf{v}_2 + \mathbf{v}_1)/2$ and the relative velocity $\mathbf{u} = \mathbf{v}_2 - \mathbf{v}_1$. This allows the following notation,

$$\begin{aligned}\mathbf{v}_2 &= \mathbf{v}_{\mathrm{COM}} + \frac{\mathbf{u}}{2}\\ \mathbf{v}_1 &= \mathbf{v}_{\mathrm{COM}} - \frac{\mathbf{u}}{2},\end{aligned}$$

where the factor $\frac{1}{2}$ comes from the reduced mass. Since the centre of mass does not change through collision, the change in velocity is dependent only on the change in relative velocity $\mathbf{v}_2' - \mathbf{v}_2 = \delta\mathbf{u}/2$. The change can be written as,

$$\begin{aligned}\mathbf{v}_2' &= \mathbf{v}_2 + \frac{1}{2}\delta\mathbf{u}\\ \mathbf{v}_1' &= \mathbf{v}_1 - \frac{1}{2}\delta\mathbf{u}.\end{aligned}$$

Since the collision can be assumed to be elastic, the velocities do not change in magnitude $|\mathbf{u}'| = |\mathbf{u}|$ and the change may be described solely by a the scattering angle θ,

$$\begin{aligned}|\delta\mathbf{u}|^2 &= |\mathbf{u}'|^2 + |\mathbf{u}|^2 - 2|\mathbf{u}'||\mathbf{u}|\cos\theta\\ &= 2|\mathbf{u}|^2(1-\cos\theta)\end{aligned}$$

Additionally, each component of $\delta\mathbf{u}$ can be expressed through a rotation as well. One can use spherical coordinates (r, φ, ϑ), where the axis $\vartheta = 0$ is coincides with the incident relative velocity vector $\mathbf{u}$. This choice implies that the polar angle ϑ is the scattering angle θ. In this coordinate system $\delta\mathbf{u}$ is given as follows,

$$\delta\mathbf{u} = \mathbf{u}' - \mathbf{u} = |\mathbf{u}| \left[\begin{pmatrix} \sin\theta\cos\varphi \\ \sin\theta\sin\varphi \\ \cos\theta \end{pmatrix} - \begin{pmatrix} 0 \\ 0 \\ 1 \end{pmatrix} \right]$$

The two angles θ, φ are free since momentum and energy conservation are already given through the choice of coordinates. This idea is the fundament of the collision model by Takizuka and Abe [24]. The model takes essentialy two steps, which consist firstly of choosing the angles randomly and secondly of pairing particles together for a collision and change their velocities oppositely. The random pairing process is - given that the time-stepping is sufficiently small - equivalent to a Monte Carlo integration of the distribution function, which is why the model asymptotes to results consistent with Landau's equation. However, they choose $\tan(\theta/2)$ according to a Gaussian distribution with a variance of $\sigma = \delta t(e^2e^2\rho\lambda)/(2\pi\varepsilon_0|\mathbf{u}|^3)$, where λ is the Coulomb logarithm. Due to explicit dependence on δt, this approach tends to choose θ too large, compared to the Landau-Operator, if the time-stepping is not small enough.

Another approach, that does not have this drawback, has been proposed by Wang *et al.* [20]. The choice of the relative velocity vector is chosen as,

$$\delta\mathbf{u} = \sin(\varepsilon)\hat{\mathbf{n}} \wedge \mathbf{u} + (1 - \cos(\varepsilon))\hat{\mathbf{n}} \wedge \hat{\mathbf{n}} \wedge \mathbf{u},$$

where $\hat{\mathbf{n}}$ is a random unit vector in spherical coordinates, depending on θ and φ, and ε is chosen small. This operator can be shown to asymptote exactly to the Landau-Fokker-Planck form, which is why both models share the same assumptions and drawbacks.

7.2 Cumulative Collisions

The main issue with computing all collisions one-by-one is the steep growth of computational cost with the number of particles. Especially for dense configurations, this approach quickly becomes inefficient. A possible solution was proposed by Nanbu [19] in the form of cumulative collisions, which essentially groups multiple binary collisions together. This is possible, since several rotations in velocity space can be expressed through a single rotation with a "cumulative" angle. Let us denote $R(\theta, \varphi)$ as a rotation matrix around azimuthal and polar angle:

$$R(\theta,\varphi) = \begin{pmatrix} \cos(\theta) & 0 & \sin(\theta) \\ 0 & 1 & 0 \\ -\sin(\theta) & 0 & \cos(\theta) \end{pmatrix} \begin{pmatrix} \cos(\varphi) & -\sin(\varphi) & 0 \\ \sin(\varphi) & \cos(\varphi) & 0 \\ 0 & 0 & 1 \end{pmatrix}.$$

Let us further say that a particle has undergone i collisions before the $(i+1)$-th, which have induced cumulative angular deviations θ_i, φ_i. If the deviation from the $(i+1)$-th collision is named $\Delta\theta_{i+1}$, $\Delta\varphi_{i+1}$, then the velocity after the $(i+1)$-th collision is given as follows,

$$\mathbf{u}_{i+1} = R(\theta_i, \varphi_i)R(\Delta\theta_{i+1}, \Delta\varphi_{i+1})\hat{\mathbf{z}}|\mathbf{u}|,$$

where the coordinate system has been chosen as above, such that the initial $\mathbf{u}$ lies along the z-axis. By virtue of Rutherford's relation eq (D.8), and the assumption that collision partners haven been uniformly distributed in space, one can write,

$$\Delta\theta_i = \tan^{-1}\left(\frac{1}{Eb_{\max}\sqrt{\alpha}}\right),$$

where $b_i = b_{\max}\sqrt{\alpha_i}$ is the random impact parameter with α_i as uniform random numbers in $[0, 1)$. Due to isotropy, the azimuthal angle $\Delta\varphi_i$ can be chosen uniformly in $[0, 2\pi)$. Given these relations, one can derive the distribution $f(\theta_N)$ of the cumulative scattering angle after N collisions, which

can be sampled and used to modify the velocity vectors. In the original, this derivation makes several assumptions to arrive at an analytical expression for the distribution $f(\theta_N)$, which is then fundamentally bound to the same limitations as the Landau operator.

A possible extension of this method is to consider empirical distributions for the cumulative scattering angle, as proposed by Chap and Sedwick [21]. Instead of deriving $f(\theta_N)$ analytically, the idea is to conduct numerical experiments to measure the cumulative scattering angle. For weakly coupled plasmas it was demonstrated that this approach consistently reproduces large-angle scattering events and thus breaks the limitations of Landau's equation.

For this thesis it was investigated, whether this model can be expanded into the high coupling regime to be used in the simulation of ultracold electron plasmas. The main hindrance is the set-up of the numerical experiments to determine the angle distribution function numerically. In the original work, the test particle was put in a box filled with randomly placed and fixed collision partners. The trajectory of the test particle is evolved over a certain time, and the angular deviation between initial and final velocity represents one sample for the distribution of cumulative scattering angles.

In weakly coupled plasmas, the thermal energy dominates the Coulomb interaction and the particle positions can be considered random, since the high thermal velocities are just weakly influenced by the repulsive electric energy. In other words, the particles can be very close to each other or very far apart, i.e. their positions and velocities are uncorrelated. However, in strongly coupled plasmas, the upcoming correlation effects lead to local modifications of the density (see eq (2.12)), due to the particle positions depending on each other.

In order to get an idea, whether the cumulative collision approach can be extended to the strong coupling regime, one needs to set up configurations of strongly coupled particles, to do measurements of $f(\theta_N)$. To this end it is possible to derive the radial pair distribution function of a strongly coupled configuration of particles even for very high coupling factors, by solving the Ornstein-Zernike equation (2.4), which is presented in section 2.3. From the pair distribution function one can then reconstruct one possible bunch of particles in a box, so essentially this approach allows to find particle configurations for arbitrary coupling factors. The numerical details on how this reconstruction can be achieved are given in appendix C.

Figure 7.1 depicts examples for two different coupling strengths. The graphs on the right show the distribution of inter-particle distances for the particles in the box on the left, whereas the solid line displays the pair distribution function, as expected from the Ornstein-Zernike equation for the given coupling factor. One may observe that for a higher coupling factor the configuration assumes a minimal distance. Consequentially, chosen particle positions randomly does not do the physical situation justice.

The gradual appearance of a structured low-temperature state, gives a clear indication of the shortcomings of the existing model. For the purpose of extending to the strong coupling regime, one could try to find a scattering angle distribution for larger coupling factors by sampling the particles in the right way. Unfortunately, finding a configuration adjusted to a pair distribution function is a very slowly converging process and not free from grave deviations, as can be seen the in the presence of very close particle pairs in figure 7.1 for the second graph. For setting up numerous simulations to compute a distribution function $f(\theta_N)$ it is far too inefficient and imprecise.

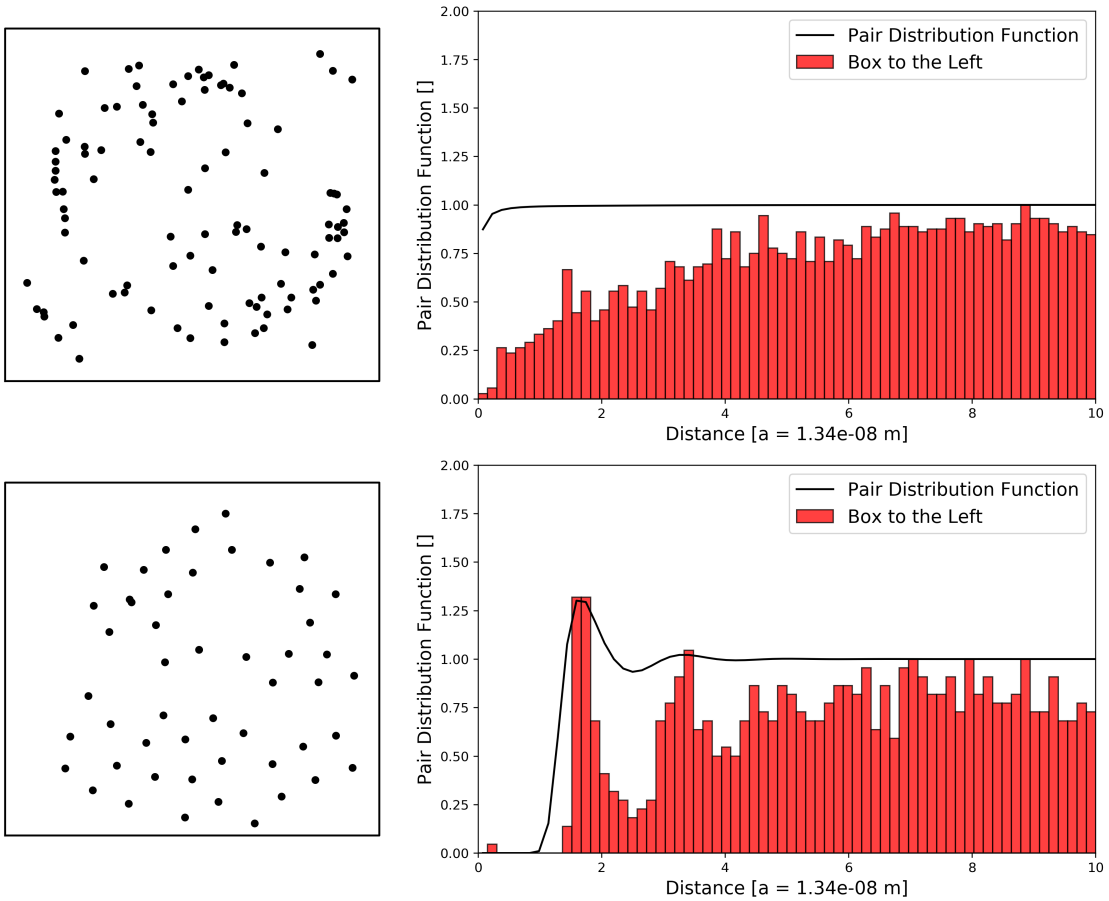

Figure 7.1: Particle configurations (left) and their respective pair distribution functions as a histogram (right). The solid line represents the analytical pair distribution function to be expected for a one-component-plasma. The radius is measured in units of the Wigner-Seitz radius.

Part III

Summary

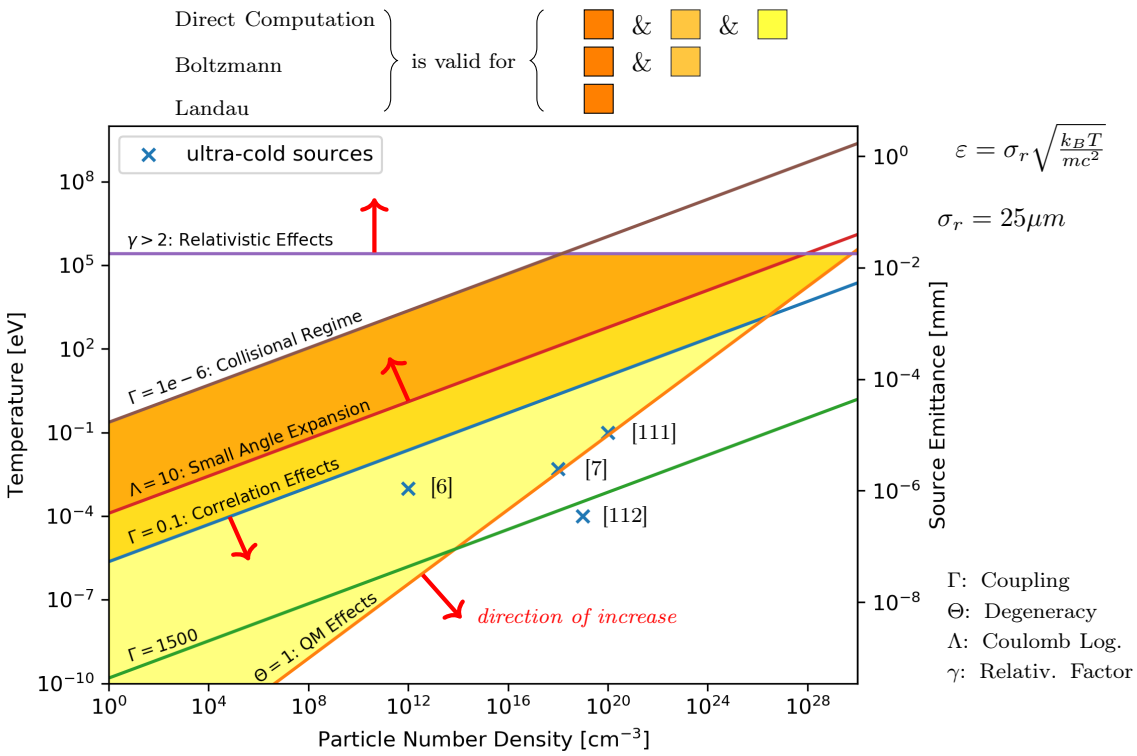

Figure 7.2: Overview over different regimes, including regions of validity for different collision models and data from ultra-cold sources. The data cited may not appear explicitly in the sources and is to be understood as an estimate based on the information provided. The point from [112] is hypothetical, whereas the others refer to experiments.

State-of-the art electron sources have demonstrated that increases in brightness of several orders of magnitude are possible by using cryo-cooled photo-cathodes or ultracold atomic gases as targets for laser excitation. This brings about substantial increases in brightness from which applications like free electron lasers or electron diffraction systems profit greatly. It is expected that these result provide a significant milestone in the development of next-generation high-brightness electron sources. Nevertheless, the emittance of a particle source is also dependent on our ability to control and mitigate space charge effects. In order to fully harness the potential of ultracold sources, it is crucial to have an accurate understanding for the influence of inter-particle collisions. Using a precise numerical collision model, one can employ large-scale simulations to gear the source towards optimal performance.

The extracted beams have very low temperatures in the tens of Kelvin, which lead inevitably to a peculiar physical picture, which is characterized by strong inter-particle coupling and - potentially - quantum mechanical interaction. For visualization, the parameter space is mapped out in figure 7.2, where several physical regimes are shown as well as recent experimental data. The figure illustrates that any successful collision model must accommodate the increasing relevance of inter-particle correlations as well as quantum mechanical effects. Thanks to unprecedented experimental progress we are advancing into a regime which poses a serious challenge to existing collision models.

A truism of physical simulations is, that there is always a trade-off between accuracy and speed. This is no different for the simulation of charged many-body systems that are interact predominantly electrically. In the collisionless limit the interaction is resolved routinely by mesh-based

mean-field calculations or by using tree-algorithms with multipole expansions. In general a collision model provides a way to reintroduce the electromagnetic interaction, that these approaches neglected. On a microscopic level this can be achieved by directly summing up the missing interaction, which is done in schemes like P^3M or FMM, or by accounting for them in a stochastic way, for example through cumulative collisions or Langevin's approach. Obviously, some approaches require stricter assumptions than others, so we can expect that not all collision models will hold in the low-temperature limit.

The most common assumption, under which most collision models operate, is the assumption of binary scattering. In this picture collisional interaction happens between two particles at a time only, or in other words, the surrounding particles do not partake in the interaction. Of course the positions of all particles are correlated with each other on some level due to Newton's equations, but as long as the correlation is negligible, the binary collision picture remains a valid assumption. Nevertheless, in the more strongly coupled ultracold sources, the binary assumption will inevitably fail. In figure 7.2 is is shown that the regime of validity of Boltzmann's collision operator does not reach far enough into the low-temperature region. The Landau operator is even more restricted by the fact that it is a small-angle approximation of Boltzmann's operator. In conclusion common kinetic collision modelling schemes like the Langevin equation, direct simulation Monte Carlo or fluid-based descriptions are not applicable to ultracold sources. The reason behind is that collisions in the low-temperature limit can no longer be considered random, as the inter-connectedness between particles grows stronger. As a consequence every kind of statistical or stochastic approximation of collision behaviour will not properly reflect physical reality. One way to still include collisions into the numerical model is by partially computing the entire interaction instead of approximating it. In figure 7.2 it is shown that "direct computation" models, such as P^3M or FMM, can describe collisions while still accommodating inter-particle correlation.

An additional way to construct a more broadly valid collision model is provided by an effective interaction potential. Basically, one incorporates correlation effects directly into the two-particle interaction potential, which allows to maintain the binary collision picture even into the strongly coupled regime. The Debye-screened Yukawa potential is probably the most famous representative of this method in plasma physics. A more general approach that goes further into the strongly coupled regime was pioneered by Baalrud and Daligault [1] and relies on the Ornstein-Zernike equation to compute an effective potential. It has been shown that classical Boltzmann theory can reliably compute various properties of strongly coupled plasmas simply by using an effective interaction potential. By using this technique the fundamental limitations of previous binary models can be circumvented.

Direct computation schemes or effective interaction potentials provide accurate ways to properly account for collision effects in a strongly coupled environment. Nevertheless, all these methods are strictly rooted in classical electrodynamics or statistical mechanics. From figure 7.2 we can see that it cannot be excluded that the collision model must take quantum interaction into consideration, where it is not entirely clear which quantum mechanical effects we have to expect. While there are categorizations of quantum corrections (e.g. [59]) they usually rely on the fluid limit, which is not valid for one-component electron plasmas. On the other hand, commonly used methods to simulate quantum many-particle-systems, such as time-dependent density functional theory, CHNC or quantum-corrected pseudo-potentials, do not hold in the low-temperature limit - again due to correlation effects - and do not allow any statements either. In general there is little known neither which quantum mechanical effects take place in strongly coupled electron plasmas nor in which hierarchy they appear. This thesis achieved - for the first time - to make a statement about the quantum contribution to the collision dynamics in ultracold sources.

This thesis proposed a method how one can measure the relevance of quantum mechanical effects,

using Pauli repulsion as a proxy. The Ornstein-Zernike equation was used to compute an effective interaction potential that fully accounts for classical correlation effects. The potential-based approach allows to include quantum effects by adding a potential representation of the Pauli exclusion principle. Through the comparison of classical cross sections, once with Pauli correction and once without, one is able to tell exactly from which point onwards Pauli repulsion can no longer be ignored. As a result of this thesis it could be determined that a classical description of particle dynamics suffices for state-of-the art electron sources. Moreover, the results showed clearly that quantum effects impact mostly the occurrence of large angle collisions. As results of Gordon *et al.* [14] indicate, large angle collisions have a direct impact on the emittance. This means on the grounds of our findings, we can heuristically expect Pauli repulsion to have a tangible influence on the final emittance. If future experiments will accomplish even higher densities, the classical description will reach its limit, which will be directly visible in key observables.

Overall it can be said that it is still unclear how to properly conceptualize a low temperature plasma in the quantum regime without a full first-principles quantum approach, which does not exist yet. The divergence occuring in CHNC simulations could be interpreted to that effect, that homogeneous mixtures of electrons with different spins are physically unreasonable at low temperatures. On the other hand, there is too little known on the topic of spin distributions in ultracold plasmas to substantiate this interpretation. In conclusion it can be said that there is still a lot open regarding the quantum nature of non-continuous low temperature charged many-particle systems.

In the context of photo-cathode-based electron sources an additional complication arises in the form of electrostatic boundary conditions from the grounded cathode. On one hand lies the fact that collision dynamics usually happens over distances, that are short compared to the distance to the cathode. On the other hand it cannot be denied that inter-particle collisions are mediated by electric interaction and can therefore be impacted by boundary conditions. This thesis investigated for the first time the magnitude of the error comitted by ignoring boundary conditions in collision events.

For this calculation a variational and fully discrete representation of the P^3M scheme has been employed that had not existed previously. On the grounds of a discretized Low's Lagrangian, a Gaussian charge screening procedure rendered it possible to reconstruct the spatially and temporally fully discrete equations of motion of the P^3M algorithm. In contrast to Ewald's direct splitting of the interaction, this approach retains the full potential. As a consequence Green's function is kept a fundamental solution to the Laplacian and allows to investigate the boundary value problem on basis of two distinct Poisson's equations. Through this formalism it could be proven that the magnitude of the error incurred by regarding collision interaction as unbounded, is directly tied to the magnitude of the discretization error coming from the meshed non-collisional interaction. This means that for all intents and purposes the error is not only completely under control, but in most applications also negligible.

The aforementioned Lagrangian provides a way to derive fully discrete and physically valid equations of motion, which describe space charge dynamics with the inclusion of close-ranged inter-particle collisions. This result provides a framework for deriving other kinetic collisional particle algorithms, by using e.g. functional expansions instead of finite-element-mesh discretization, which opens up a broad range of possibilities. For future work this could be used as a first step towards a fully symplectic collisional space-charge map.

Part IV

Appendix

Appendix A

Numerical Transforms

In this chapter the numerical methods, that are underpinning the evaluation of the Fourier transform in the Ornstein-Zernike solver, are presented.

A.1 Discrete 3-dim Fourier Transform

It was shown previously (2.13) that the evaluation of 3-dimensional Fourier transforms can be reduced to a 1-dimensional Fourier-Bessel Transform if the function to be transformed exhibits spherical symmetry. For a function $f : \mathbb{R} \to \mathbb{R}$ in L_2, the transform reads as follows,

$$\hat{f}(k) = 4\pi \int_0^\infty f(r) \frac{\sin(kr)}{kr} r^2 dr. \tag{A.1}$$

This can be reformulated to the evaluation of a Fourier Sine transform, SinT$[\cdot]$,

$$\begin{aligned}
\hat{f}(k) &= 4\pi \int_0^\infty f(r) \frac{\sin(kr)}{kr} r^2 dr \\
&= \frac{4\pi}{k} \int_0^\infty r f(r) \sin(kr) dr \\
&= \frac{4\pi}{k} \mathrm{SinT}[r f(r)].
\end{aligned}$$

For a numerical evaluation of eq (A.1) the interval is restricted to $[r_0, L]$, which is discretized with N points. The stepping is given through the following expressions,

$$\begin{aligned}
dr &= \frac{L - r_0}{N} \\
dk &= \frac{2\pi}{L}
\end{aligned}$$

One can readily discretize eq (A.1) with $k_i = idk + \frac{2\pi}{L}$, $r_i = idr + r_0$, which yields,

$$\hat{f}(k_j) = 4\pi \sum_{i=1}^{N} f(r_i) \frac{\sin(k_j r_i)}{k_j r_i} r_i^2 dr.$$

Again, this may be further reduced to the evaluation of a discrete Fourier-Sine-Transform DST$[\cdot]$,

$$\hat{f}(k_j) = \frac{4\pi}{k_j} \mathrm{DST}[r \cdot f(r)](k_j),$$

where $\mathrm{DST}[r \cdot f(r)]$ is the evaluation of the discrete Fourier-Sine-Transform over the same interval with the same discretization.

A fast way to evaluate the sine transform via FFT was provided by Makhoul [115]. Let us denote $f(r_i)$ as f_i for simplicity. Then a set of points $\{g_i\}$ is constructed as follows,

$$g_i = f_{2i} \qquad \text{for } i = 1, ..., \frac{N}{2} - 1$$
$$g_{N-1-j} = -f_{2i+1} \qquad \text{for } i = 1, ..., \frac{N}{2} - 1,$$

where the even and odd points are separated. The discrete Sine Transform can then be obtained from the FFT,

$$\mathrm{DST}[b]_j = -\,\mathrm{Im}\left(\mathrm{FFT}[g]_j e^{-i\pi \frac{k}{2N}}\right). \tag{A.2}$$

In figure A.1 one can see the numerical Sine transform of the function $\frac{e^{-r}}{r}$, for which the analytic Sine Transform is known to be $\arctan(k)\sqrt{2/\pi}$. It can be seen that the implementation is indeed bijective, even though there are deviations from the expected Sine Transform. The Fourier-Bessel transform essentially shows the same behaviour, as shown in figure A.2.

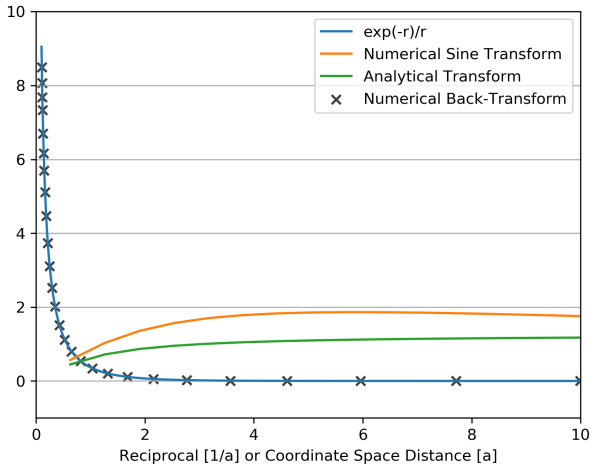

Figure A.1: Forward and backward Sine Transformation for the function $\frac{e^{-r}}{r}$.

These deviations stem from the fact that in Python 3.7.6 the expression `np.sin(r)/r` is divergent if evaluated at `r=0`, even though it analytically is not. This means that numerically, the evaluation of a Fourier-Bessel Transform $\hat{f}$ as a Sine Transform of $r \cdot f(r)$ is not entirely accurate, because `np.sin(kr)/(kr)` is not entirely the same as `np.sinc(kr)`. By virtue of the same problem, the expression $\mathrm{SinT}[r \cdot f(r)]/k$ is analytically the same as $\mathrm{SinT}[r \cdot f(r)/k]$ but they are not equal numerically.

It is possible to circumvent this issue, using an Taylor expansion of the sine function. However, in figure A.2 it can be seen that the the numerical solution via eq. (A.2) diverges less for $r \to 0$ than the analytical solution. Overall, this tendency to smaller values is beneficial for the solution of the Ornstein-Zernike equation as it means greater stability.

Since the solution procedure for the Ornstein-Zernike equation always uses the forward and back-transform successively within one iteration step, the precision of the solution is not affected because the transform is still bijective. The main advantage of this procedure is its speed that comes naturally from using FFT and the increased stability against divergence.

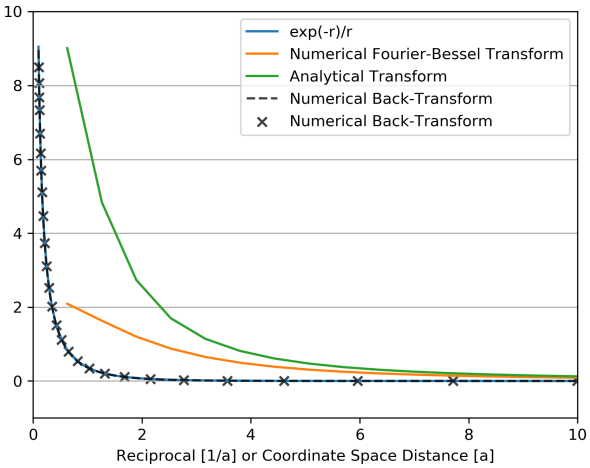

Figure A.2: Forward and backward Fourier-Bessel Transform of the Yukawa Potential with reach 1.

A.2 Regularization

The Coulomb potential has by definition infinite reach and will not vanish at the end of the integration interval. As a consequence the discrete Fourier transform shows severe numerical instabilities that lead to strong deviations in any application. In order to compute a transform of a long-ranged function it needs to be regularized to be zero at the end of the interval.

This is done by using a correction function $K(r)$, as proposed by Springer *et al.* [116], which is subtracted and later added again. Let f be a function that is non-zero at the end of the transformation interval. Instead of directly transforming f, we evaluate the corrected version as follows,

$$\mathrm{FFT}[f] = \mathrm{FFT}[f - K] + \hat{K},$$

which amounts to the same result since Fourier transforms are linear. As long as $f - K$ vanishes at the end of the interval, the transform can be evaluated without issue.

In the case of the Ornstein-Zernike solver described in section 2.3, this correction is applied to all major quantities in the calculation, i.e. the direct correlation function $c(r)$ (see eq (2.8)), the indirect correlation function $\gamma(r)$ (see eq (2.4)) and the interaction potential $\phi(r)$. The correction is applied as follows,

$$\begin{aligned}
\phi(r) &\to \phi(r) - K(r), \\
\gamma(r) &\to \gamma(r) + K(r), \\
c(r) &\to c(r) - K(r).
\end{aligned}$$

This choice implies that the corrections from γ and ϕ will cancel each other, such that the pair distribution function is not affected. In the algorithm one can leave out the correction for γ, which means we compute an "already" corrected γ, which leads to regular transforms. Applying the above corrections to eqns (2.4) and (2.8), the iteration cycle is then given by the following two equations,

$$\begin{aligned}
c(r) &= e^{-\frac{q(\phi - K)}{k_B T} + \gamma(r) + B(r)} - \gamma(r) - 1, \\
\hat{\gamma}(k) &= \frac{\rho(\hat{c}(k) - \hat{K}(k))^2}{1 - \rho(\hat{c}(k) - \hat{K}(k))} - \hat{K}(k).
\end{aligned} \tag{A.3}$$

For the calculations in this thesis the correction function from Ng [47],

$$K(r) = \frac{\mathrm{Erf}(\alpha r)}{r}$$
$$\hat{K}(k) = \frac{4\pi}{k^2} e^{-\frac{k^2}{4\alpha^2}},$$

where the choice of α depends on the interval length. Generally, $\alpha = 0.8 - 1.08$ work well, but it is advisable to check with plots like figure A.3, whether the goal of regularizing the transform was achieved. In a successful case the transform is regular as in figure A.3.

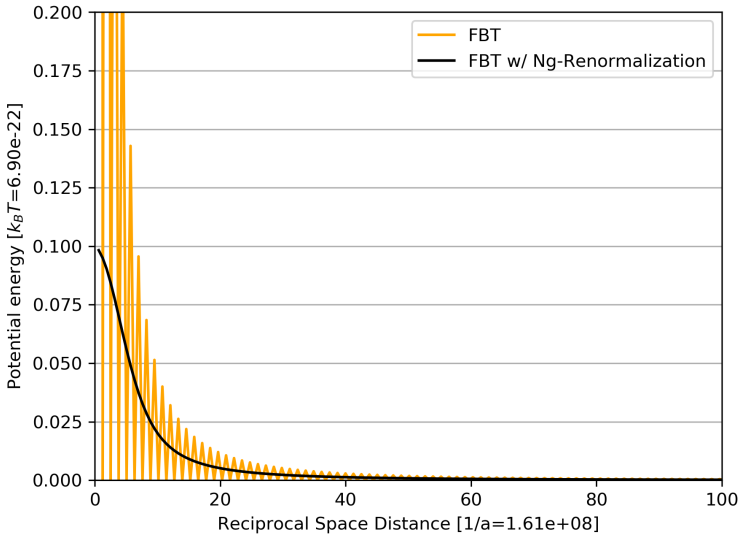

Figure A.3: Comparison between the discrete Fourier-Bessel Transforms (FBT) of the corrected and uncorrected bare Coulomb potential.

Appendix B

Computation of Pauli's Potential

As soon as the quantum nature of electrons starts to become important, they begin to obey Fermi-Dirac statistics, whose effect can be incorporated with the Pauli potential. Essentially, it is a method to describe the repulsive effect of quantum statistics by means of an interaction potential.

B.1 Theoretical Basis

The computation of the Pauli potential for this thesis follows the scheme outlined by Dharma-Wardana and Perrot [70]. The main idea of the approach is to find an expression for the pair distribution function, from which the potential can be obtained, using the Ornstein-Zernike equation.

The pair distribution function corresponding to the Pauli Potential is given as,

$$g(r) = 1 - F_T(r)^2, \tag{B.1}$$

where F_T is the 3-dimensional Fourier Transform of the Fermi-Dirac distribution function $n(k)$,

$$F_T(\mathbf{r}) = \mathcal{F}^{-1}\left[\frac{1}{1 + e^{\frac{E_F(\mathbf{k}^2-1)}{k_B T}}}\right](\mathbf{r}),$$

where E_F corresponds to the Fermi energy.
From the pair distribution function, the Pauli potential $\frac{P}{k_B T}$ can be obtained,

$$\frac{P}{k_B T} = -\log(g) + h(r) - c(r),$$

where h and c can be calculated by combined use of (2.8) and (2.4) and (B.1). The numerical steps of the calculation include the computation of the Fourier-Bessel Transform above, the subsequent computation of the potential as an effective potential and the continuation of the result outside of the solution interval.

B.2 Numerical Transform

If it is required to obtain the Fourier-Bessel Transform of an expression to high accuracy, one needs a different implementation than the FFT-based version from appendix A. The algorithm used for this thesis was proposed by Candel [117, 118] and relies on weighted summation of different Fourier components.

At $T \approx 0$ the Fermi-Dirac distribution is a step function and the Fourier Transform can be calculated analytically [119],

$$\hat{n}(r) = 2\frac{J_1(k_F r)}{k_F r},$$

where k_F is the Fermi wave vector corresponding to the Fermi energy $E_F = \hbar^2 k_F^2/(2m)$. In figure B.1, one can see that the numerical result for $T \approx 0$ lies in good accordance with the analytical result.

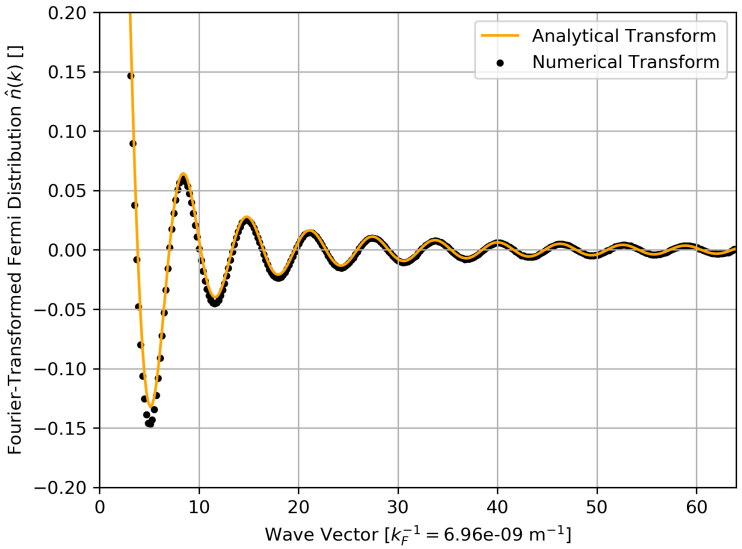

Figure B.1: Comparison between the analytical Fourier Transform of the Fermi-Dirac distribution with its numerical counterpart, computed with the algorithm of Candel [117]. Length is scaled to the inverse Fermi wave vector.

On a side note: despite that the algorithm displays very good accuracy, it is unfit to be used in the OZ-iteration. Firstly, the back-transform is not specified by Candel and secondly the computational cost is too high for repeated application, compared to FFT.

B.3 Continuation

In the same spirit as for the effective potential, one would like to have a continuous function that can be evaluated outside of the integration interval. The easiest way to proceed, is to notice that the pair distribution function has the general shape of a sigmoid. The fitting routine used for the calculations in this thesis fits the following function,

$$g^c(r) = \frac{\mathrm{Erf}(a_1 r - a_2) + 1}{2},$$

where a_1, a_2 are fitting parameters. Additionally one can fit $\gamma = h - c$, which has been found to be described appropriately by the following function,

$$\gamma^c(r) = \frac{\mathrm{Erf}(a_3 r) + 1}{\sqrt{r}},$$

where a_3 is a fitting parameter. The result of this routine then gives the Pauli potential,

$$\frac{P(r)}{k_B T} = -\log(g^c(r)) - \gamma^c(r). \tag{B.2}$$

The result can be seen in figure B.2, which coincides well with the graph from Dharma-Wardana and Perrot [70] thus verifying the procedure.

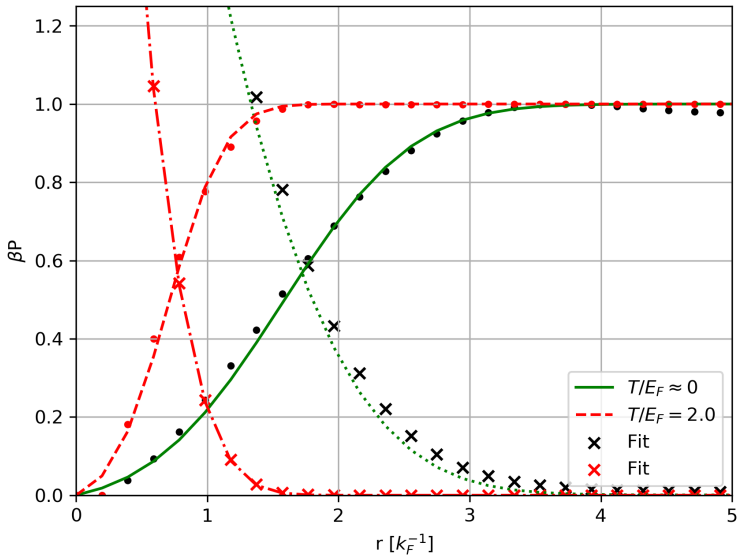

Figure B.2: Discrete and Fitted Pauli potential and corresponding pair distribution function.

In order to extract the potential from (B.2) one needs to multiply by $k_B T_{\mathrm{cf}}$, where T_{cf} is given according to eq (3.1).

Appendix C

Reconstructing Distributions from a Pair Distribution Function

The solution to the OZ equation comes in the form of a pair distribution function, which is a statistical measure for local modulations of the particle number density. In order to get insight on what exactly this means in terms of particles in a box, one can attempt to reconstruct a configuration that corresponds to a given pair distribution function. One possible method, based on an approach by Rintoul and Torquato [120], is rooted in simulated annealing.

The idea is to generate a random distribution of N particles p_i, that are given within a box $[-L, L] \times [-L, L]$. The pair distribution $g(r)dr$ of this configuration gives the probability for the inter-particle distance to assume a value within $[r, r+dr]$. This can be approximated by discretizing distance as $r_i = i\Delta r$ and measuring the occurrence $H(r_i)$ of each bin. The discrete approximation $g_d(r_i)$ of the pair distribution function $g(r)$ is then given as,

$$g_d(r_i) \approx \frac{H(r_i)}{M\Delta r},$$

where $M = \binom{N}{2}$ is the number of distance samples.

The deviation between the pair distribution function and its discrete approximation $\Delta g = \sum_i (g(r_i) - g_d(r_i))^2$ is a measure for the deviation between the present configuration from the desired one. The initial distribution is now successively modified by going through each particle and deviating it by (dx, dy), which is picked from a uniform distribution on $[-1, 1] \times [-1, 1]$. In the sense of the Metropolis algorithm, the acceptance probability for the change is given as,

$$P = e^{-\frac{\Delta g}{k_B T}},$$

where T can be gradually decreased or chosen as the physical plasma temperature. For the present case, the move is also rejected, if the particle would end up outside of the simulation box. The computation cost grows quadratically with the particle number and the method generally converges very slowly, due to the randomness of the changes. An example can be found in figure 7.1.

Appendix D

Classical Two-Body Scattering Cross Sections

This chapter serves the purpose of reviewing classical two-body scattering formulae, which are used throughout the thesis. In addition, it will be shown, how cross sections change in the presence of screening. The material presented here can be found in every standard textbook to classical mechanics or scattering dynamics, e.g. [121]. A different take on the derivation of Rutherford's cross section was given by Krane [122].

D.1 Classical Two-Body Scattering Theory

The Lagrangian for two particles that interact via Coulomb's potential ϕ reads as follows,

$$\mathcal{L} = \frac{1}{2}m\dot{\mathbf{r}}_1 + \frac{1}{2}m\dot{\mathbf{r}}_2 - q\phi(|\mathbf{r}_1 - \mathbf{r}_2|).$$

We can introduce the relative distance vector $\mathbf{r} = \mathbf{r}_1 - \mathbf{r}_2$ and the centre of mass vector $\mathbf{R} = (\mathbf{r}_1 + \mathbf{r}_2)/2$ to simplify the situation to a one body problem. We have,

$$\mathbf{r}_1 = \mathbf{R} + \frac{1}{2}\mathbf{r}$$
$$\mathbf{r}_2 = \mathbf{R} - \frac{1}{2}\mathbf{r}$$

Inserting yields the following,

$$\mathcal{L} = m\dot{\mathbf{R}} + \frac{m}{4}\dot{\mathbf{r}} - q\phi(|\mathbf{r}|)$$

Obviously $\dot{\mathbf{R}}$ is a cyclic coordinate, so the problem is simplified by choosing the frame of reference such that $\dot{\mathbf{R}} = 0$ and transforming into the centre-of-mass frame. Since angular momentum is conserved as well, the dynamics are restricted to a plane and the problem can be treated as two-dimensional. Therefore, one can transform to polar coordinates (r, φ) as the Coulomb potential is dependent on distance only,

$$\mathcal{L} = \frac{m}{4}\left(\dot{r}^2 + r^2\dot{\varphi}^2\right) - q\phi(r),$$

where it was used that $\dot{\mathbf{r}} = \dot{r}\mathbf{e}_r + r\dot{\varphi}\mathbf{e}_\varphi$, denoting $|\mathbf{r}| =: r$. For further simplification, one can express angular momentum in polar coordinates as well,

$$l = \mathbf{r} \wedge \frac{m}{2}\dot{\mathbf{r}} = \frac{m}{2} r^2 \dot{\varphi},$$

which allows to write the polar Lagrangian in the following way,

$$\mathcal{L} = \frac{m}{4}\dot{r}^2 - q\phi(r) - \frac{l^2}{mr^2}. \tag{D.1}$$

As already mentioned, the two governing integrals of motion are energy and angular momentum, which yield two coupled, first-order ordinary differential equations,

$$\frac{d}{dt}\left[\frac{m}{4}\dot{r}^2 + \frac{l^2}{mr^2} + q\phi(r)\right] = 0 = \frac{d}{dt}E$$
$$\frac{d}{dt}\left[\frac{m}{2} r^2 \dot{\varphi}\right] = 0 = \frac{d}{dt} l.$$

We can find a differential equation for the angle as a function of the radius, by solving above equations for $\dot{r}$ and $\dot{\phi}$,

$$\frac{d\varphi}{dr} = \frac{\dot{\varphi}}{\dot{r}} = \frac{\frac{2l}{mr^2}}{E - (\frac{l^2}{mr^2} + q\phi(r))},$$

which can be readily integrated to give the following expression for the angle,

$$\varphi(r) = \int_{r_{\min}}^{\infty} \frac{\frac{2l}{mr^2}}{E - (\frac{l^2}{mr^2} + q\phi(r))} dr,$$

where $r_{\min}$ belongs to the singularity,

$$E - \frac{l^2}{mr_{\min}^2} - q\phi(r_{\min}) = 0.$$

The set-up of a two-body scattering situation is illustrated in figure D.1. Going by this notation we can rewrite the angular momentum as $l = b\sqrt{2mE}$, assuming the projectile starts out far away from the target.

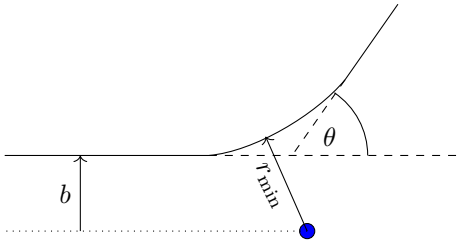

Figure D.1: The smallest distance between target (blue) and projectile (solid line) is $r_{\min}$, the deviation angle is θ and b denotes the impact parameter.

The scattering angle $\theta = \pi - 2\varphi$, can then be expressed through the classical scattering integral in the following way,

$$\theta = \pi - 2\int_{r_{\min}}^{\infty} \frac{b}{r^2\sqrt{1 - \frac{\phi(r)}{E} - \frac{b^2}{r^2}}} dr, \tag{D.2}$$

with the relation for the radius of minimal distance,

$$1 = \frac{\phi(r_{\min})}{mv^2/2} + \frac{b^2}{r_{\min}^2}. \tag{D.3}$$

The classical cross section is given by the ratio of the area element $d\sigma = bd\phi db$ of the incident annulus and the solid angle element $d\Omega = \sin(\phi)d\phi d\theta$. Consequentially, the formula is given as follows,

$$\frac{d\sigma}{d\Omega} = \frac{b}{\sin\theta}\left|\left(\frac{d\theta}{db}\right)^{-1}\right|. \tag{D.4}$$

Together the relations (D.2), (D.3), (D.4) compose the classical picture of a collision cross section.

D.2 Rutherford's Cross Section

The equations (D.2), (D.3), (D.4) can be solved analytically for the bare Coulomb potential,

$$e\phi(r) = \frac{e^2}{4\pi\varepsilon_0}\frac{1}{r} =: k_C\frac{1}{r},$$

where k_C denotes the constant pre-factor. With the following substitution,

$$\begin{aligned} r &= \frac{1}{u} \\ dr &= -r^2 du, \end{aligned} \tag{D.5}$$

the scattering integral can be solved analytically by using the following formula,

$$\begin{aligned} \frac{d}{dx}\arccos\left(\frac{\alpha x+1}{\sqrt{\beta+1}}\right) &= \frac{-1}{\sqrt{1-\frac{(\alpha x+1)^2}{\beta+1}}}\cdot\frac{a}{\sqrt{\beta+1}} \\ &= \frac{-1}{\sqrt{\frac{\beta}{\alpha^2}-x^2-\frac{2}{\alpha}x}}. \end{aligned} \tag{D.6}$$

The minimial radius $u_{\min} = \frac{1}{r_{\min}}$ can be rewritten accordingly,

$$\begin{aligned} &\frac{\beta}{\alpha^2} - u_{\min}^2 - \frac{2}{\alpha}u_{\min} = 0 \\ \Longrightarrow\ &u_{\min} = \frac{1}{a}\left(\sqrt{1+\beta}-1\right). \end{aligned} \tag{D.7}$$

The θ-b relation can then be found in a straightforward manner, using eq (D.6) with $\alpha = \frac{2Eb}{k_C}$ and $\beta = \frac{4E^2b^2}{k_C^2}$,

$$
\begin{aligned}
\theta &= \pi - 2\int_{r_{\min}}^{\infty} \frac{-1}{\sqrt{\frac{1}{b^2} - \frac{k_C}{Eb^2}u - u^2}} du \\
&= \pi - 2\left[\arccos\left(\frac{\frac{2Eb^2}{k_C}u}{\sqrt{\frac{4E^2b^2}{k_C}+1}}\right)\right]_{1/r_{\min}}^{0} \\
&= \pi - 2\arccos\left(\frac{1}{\sqrt{\frac{4E^2b^2}{k_C^2}+1}}\right) \\
&= 2\arcsin\left(\frac{1}{\sqrt{\frac{4E^2b^2}{k_C^2}+1}}\right) \\
\implies \frac{1}{\sin^2\left(\frac{\theta}{2}\right)} - 1 &= \frac{4E^2b^2}{k_C^2} \\
\cot^2\left(\frac{\theta}{2}\right) &= \frac{4E^2b^2}{k_C^2} \\
\cot\left(\frac{\theta}{2}\right) &= \frac{2Eb}{k_C}
\end{aligned}
\tag{D.8}
$$

Rutherford's cross section can then be calculated with eq (D.4),

$$
\begin{aligned}
\frac{d\sigma}{d\Omega} &= \frac{b}{\sin\theta}\left|\frac{-k_C}{4E\sin^2\left(\frac{\theta}{2}\right)}\right| \\
&= \frac{k_C^2\cot\left(\frac{\theta}{2}\right)}{8E^2\sin(\theta)\sin^2\left(\frac{\theta}{2}\right)} \\
&= \frac{k_C^2}{16E^2\sin^4\left(\frac{\theta}{2}\right)}
\end{aligned}
\tag{D.9}
$$

D.3 Cross Sections of Screened Potentials

Introduction of screening to a potential usually means a steep decline in strength, such that it becomes negligible after a certain distance. In the following the consequences of this will be illustrated with respect to the classical collision cross section.

In order to calculate an analytical result, a first order approximation of Yukawa's potential will be used,

$$
\phi(r) = k_C\left(\frac{1}{r} - \frac{1}{\lambda_D}\right)\Theta(\lambda_D - r), \tag{D.10}
$$

where Θ denotes the Heaviside function. Another possibility is to leave the subtraction out and multiply the heaviside function directly with the free Green function. However, although the potential still converges to the unscreened original for $\Lambda_D \to \infty$, the corresponding cross-section does not converge to Rutherford's formula, as shown by Semon and Taylor [123]. For this reason the formulation (D.10) will be used. For simplicity we will also set $k_C = 1$.

Insertion of (D.10) into (D.2) yields two integrals,

$$\theta - \pi = -2\int_{r_m}^{\lambda_D} \frac{b\frac{dr}{r^2}}{\sqrt{1 - \frac{1}{E}\frac{1}{r} + \frac{1}{E}\frac{1}{\lambda_D} - \frac{b^2}{r^2}}} - 2\int_{\lambda_D}^{\infty} \frac{b\frac{dr}{r^2}}{\sqrt{1 - \frac{b^2}{r^2}}}.$$

Both can be solved by application of the same methods found in eqns (D.5), (D.6) and (D.7). The result for $\theta(b)$ reads as follows,

$$\frac{\theta}{2} = \arcsin\left(\frac{\frac{4E^2b^2}{2\lambda_D} + 1}{\sqrt{4E^2b^2 + \frac{4Eb^2}{\lambda_D} + 1}}\right) + \arcsin\left(\frac{b}{\lambda_D}\right), \tag{D.11}$$

where λ_D is again the Debye length. This expression reduces nicely to (D.8) in the limit $\lambda_D \to \infty$. The derivative can be readily evaluated,

$$\frac{d\theta}{db} = 2\frac{\frac{4Eb}{\lambda_D\sqrt{\frac{4Eb^2}{\lambda_D}+4E^2b^2+1}} - \frac{\left(\frac{2Eb^2}{2\lambda_D}+1\right)\left(\frac{8Eb}{\lambda_D}+8E^2b\right)}{2\left(\frac{4Eb^2}{\lambda_D}+4E^2b^2+1\right)^{3/2}}}{\sqrt{1 - \frac{\left(\frac{2Eb^2}{\lambda_D}+1\right)^2}{\frac{4Eb^2}{\lambda_D}+4E^2b^2+1}}} + \frac{2}{\lambda_D\sqrt{1-\frac{b^2}{\lambda_D^2}}}$$

$$\overset{\lambda_D\to\infty}{\longrightarrow} \frac{4E}{1+4E^2b^2} = 4E\sin^2\frac{\theta}{2}.$$

For the cross section, the following can be obtained,

$$\frac{d\sigma}{d\Omega} = \frac{b}{\sin\theta}\left|\left(2\frac{\frac{4Eb}{\lambda_D\sqrt{\frac{4Eb^2}{\lambda_D}+4E^2b^2+1}} - \frac{\left(\frac{2Eb^2}{2\lambda_D}+1\right)\left(\frac{8Eb}{\lambda_D}+8E^2b\right)}{2\left(\frac{4Eb^2}{\lambda_D}+4E^2b^2+1\right)^{3/2}}}{\sqrt{1 - \frac{\left(\frac{2Eb^2}{\lambda_D}+1\right)^2}{\frac{4Eb^2}{\lambda_D}+4E^2b^2+1}}} + \frac{2}{\lambda_D\sqrt{1-\frac{b^2}{\lambda_D^2}}}\right)^{-1}\right|. \tag{D.12}$$

Since the inversion of eq (D.11) is highly non-trivial, (D.12) can no longer be reduced to depend only on b or only on θ. However, Rutherford's result (D.9) can still be recovered in the limit of large Debye lenghts.

From eq (D.12) one observes, that the second term resembles the cross section of a hard-sphere potential with radius λ_D, which becomes complex for $b > \lambda_D$. This can be understood through the observation that impact parameters $b > \lambda_D$ cause a divergence in a screened potential, since they are not influenced and correspond to the same angle of deviation, namely $\theta = 0$. In other words, there are infinitely many paths to "miss" the sphere and not scatter at all. In conclusion it makes no sense to consider impact parameters larger than the screening length. The physical argument is, it would be unreasonable to consider a collision between particles, that are not influenced by each others presence in the first place.

Even though other types of screening do not directly lead to a hard-sphere potential they will still display this behaviour. Numerically, there will be a point where the potential can be considered effectively zero and the divergence will take place. This means the impact parameters must be chosen carefully, when considering the cross section of a screened potential.

D.4 Solving Classical Scattering Integrals

The computation of a classical collision cross section involves numerically integrating equation (D.2), solving equation (D.3) and finite differences to compute (D.4). In the following the numerical difficulties of these calculations will be presented alongside a high-precision method to overcome them.

D.4.1 Root Solver

The main difficulty of finding the root of eq (D.3) is the nature of the potential considered. The effective potential corresponding to a pair distribution function oscillates in the high coupling regime (e.g. visible in figure 2.9). Due to this oscillating behaviour there can be several roots to eq (D.3) of which we need to select the largest. Therefore, a method is needed that manages to find all the roots and select the largest among them. Compared to all the other steps of the calculation - even the solution of the OZ equation - this step usually requires the most time.

Additionally, the convergence of a root solver depends strongly on the initial conditions. This can be alleviated by using e.g. the bisection method, that takes two points, for which the function evaluates to opposite signs. This requires more computation time but has guaranteed convergence.

The perihelion function f is given from eq (D.3) and reads,

$$f(r) = 1 - \frac{\phi(r)}{E} - \frac{b^2}{r^2},$$

of which the roots correspond to the radius of minimal distance $r_{\min}$. The calculations in this thesis were done by traversing $f(r)$ and making a list of points $p_1, p_2, p_3, ...$, where $f(p_1)$, $f(p_2)$ have opposite sign and $f(p_2)$, $f(p_3)$ have opposite sign. To proceed one can form brackets $[p_1, p_2]$, $[p_2, p_3], ...$ from this list and use standard methods. The procedure is outlined in listing D.1.

Listing D.1: Root Solver

```
import numpy as np
import scipy.optimize as opt

# x is the discrete radius
# peri is the perihelion

pts = [x[-1]] # farthest point
roots = []

# start from the last element of x, since we search the largest root
for i in np.flip(x)[::m]:
   if(np.sign(peri(i)) != np.sign(peri(pts[-1])) and peri(i)!=0.0):
      pts.append(i)

# solve for roots with standard bracketed root solver
for i in range(len(pts)-1):
   roots.append(opt.root_scalar(peri, bracket=[pts[i],pts[i+1]], method='brentq').root)

# desired root is largest element of roots
# max(roots)
```

D.4.2 Scattering Integral Solver

The scattering integral eq (D.2) has an infinite integration interval. Consequentially, if one simply uses an integrator on samples over a fixed interval (e.g. Simpson quadrature) a large portion of the integration is neglected. For the bare Coulomb potential, the θ-b relation is given as eq (D.8),

$$2Eb = \cot\frac{\theta}{2}.$$

In figure D.2 one can see a comparison between the analytical result and the numerical solution obtained with direct integration. It is clearly visible that towards the end of the interval, the cut-off induces large deviations.

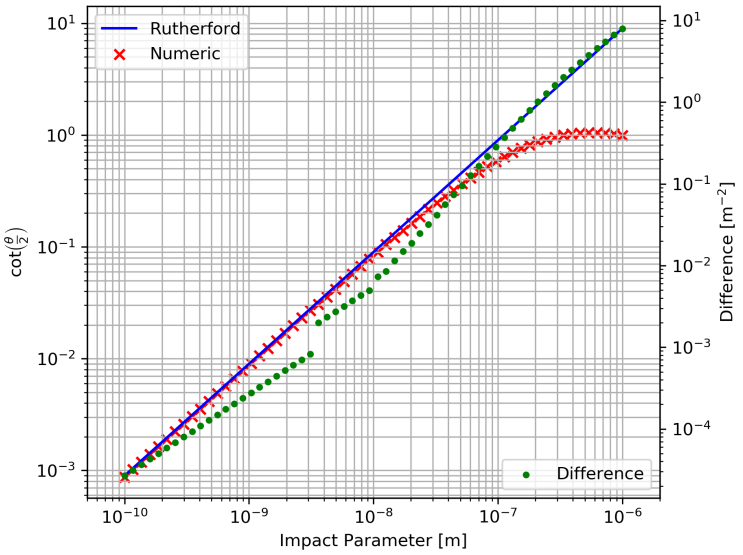

Figure D.2: Comparison between the function $\theta(b)$ from Rutherford's solution and from sample-based Simpson integration. The incident energy was assumed to be the thermal energy. The right axis shows the deviations.

In order to evaluate the integral over the full integration range, it must be transformed to a finite domain. While there are several possibilities to do so [42, 124], in the following the prescription by Mendenhall and Weller [125] will be used,

$$r = \frac{r_{\min}}{\cos\left(\frac{z\pi}{2}\right)},$$
$$dr = \frac{\pi r_{\min} \sin\left(\frac{\pi z}{2}\right)}{1+\cos(\pi z)} dz,$$

where $r_{\min}$ is the radius of minimal distance, given by eq (D.3). The scattering integral (D.2) transforms as follows,

$$\phi(r) = \int_0^1 b \left(\left[\frac{4r_{\min}^2}{\pi^2 \sin^2\left(\frac{\pi z}{2}\right)} \right] \left[1 - \frac{\phi(r(z))}{E} - b^2 \frac{\cos^2\left(\frac{z\pi}{2}\right)}{r_{\min}^2} \right] \right)^{-\frac{1}{2}} dz.$$

This can be further simplified by reusing eq (D.3) in the form $1 = \frac{\phi(r_{\min})}{E} + \frac{b^2}{r_{\min}^2}$, which gives the following,

$$\begin{aligned}
\phi(r) &= \int_0^1 b \left(\left[\frac{4r_{\min}^2}{\pi^2 \sin^2\left(\frac{\pi z}{2}\right)} \right] \left[\frac{\phi(r_{\min})}{E} - \frac{\phi(r(z))}{E} + \frac{b^2}{r_{\min}^2} - b^2 \frac{\cos^2\left(\frac{z\pi}{2}\right)}{r_{\min}^2} \right] \right)^{-\frac{1}{2}} dz, \\
&= \int_0^1 b \left(\left[\frac{4r_{\min}^2}{\pi^2 \sin^2\left(\frac{\pi z}{2}\right) E} \right] \left[\phi(r_{\min}) - \phi(r(z))\right] + \frac{4b^2}{\pi^2} \frac{1 - \cos^2\left(\frac{\pi z}{2}\right)}{\sin^2\left(\frac{\pi z}{2}\right)} \right)^{-\frac{1}{2}} dz, \\
&= \int_0^1 b \left(\left[\frac{4r_{\min}^2}{\pi^2 \sin^2\left(\frac{\pi z}{2}\right) E} \right] \left[\phi(r_{\min}) - \phi(r(z))\right] + \frac{4b^2}{\pi^2} \right)^{-\frac{1}{2}} dz.
\end{aligned}$$

It is noteworthy that the term $\sim \frac{1}{\sin^2(z)}$ does not diverge, because $z \to 0$ corresponds to $r \to r_{\min}$. This can be confirmed by de L'Hôpital's rule,

$$\frac{\frac{d}{dz}\left[\phi(r_{\min}) - \phi(r(z))\right]}{\frac{d}{dz}\sin^2\left(\frac{\pi z}{2}\right)} = \frac{\left.\frac{d\phi}{dr}\right|_{r_{\min}} r_{\min}}{2\cos^3\left(\frac{\pi z}{2}\right)} \xrightarrow{z\to 0} \text{const}$$

By the same reasoning the overall divergence (formerly $r \to r_{\min}$) is removed as well, as long as

$$\left.\frac{d\phi}{dr}\right|_{r_{\min}} < 2\frac{b^2 E}{r_{\min}^3} \cos^3\left(\frac{\pi z}{2}\right),$$

which is given as the potential is repulsive and the RHS strictly positive.

For the treatment of effective potentials there are two things to keep in mind. Firstly, since the largest root of the perihelion is chosen for $r_{\min}$, the oscillations occurring in an effective potential make no difference in the above condition on the derivative. Secondly, this transformation still evaluates the radius in the full intervall $[r_{\min}, \infty)$, which means it must be possible to evaluate the effective potential at these points. The techniques for finding a suitable continuation are shown in section 2.3.

With this transformation and a continuous potential function, we can integrate e.g. with a Gauss-Legendre quadrature. In figure D.3 it is shown that the integration routine reproduces Rutherford's result with high accuracy.

D.4.3 Computing the Cross Section

The final step is to take finite differences to obtain the cross section from eq (D.4), which does not pose further problems, except that it becomes inaccurate when too few points are computed. For completeness sake figure D.4 illustrates the good accordance between the analytical result and the numerical values.

D.4.4 Choice of Incident Impact Parameter

From eqns (D.11), (D.12) we know that screened potentials are divergent in classical theory, if the impact parameter is chosen larger than the screening length. In order to avoid distortion of the results one needs to assess the screening length of the potential considered and choose the impact parameters smaller. The methods to find the screening length for an effective potential is outlined in section 2.3.

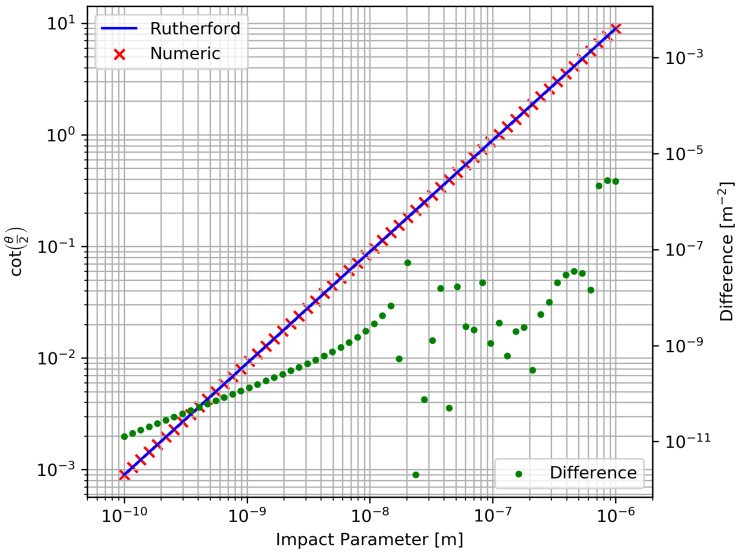

Figure D.3: Comparison between the function $\theta(b)$ from Rutherford's solution and from Gauss-Legendre integration.

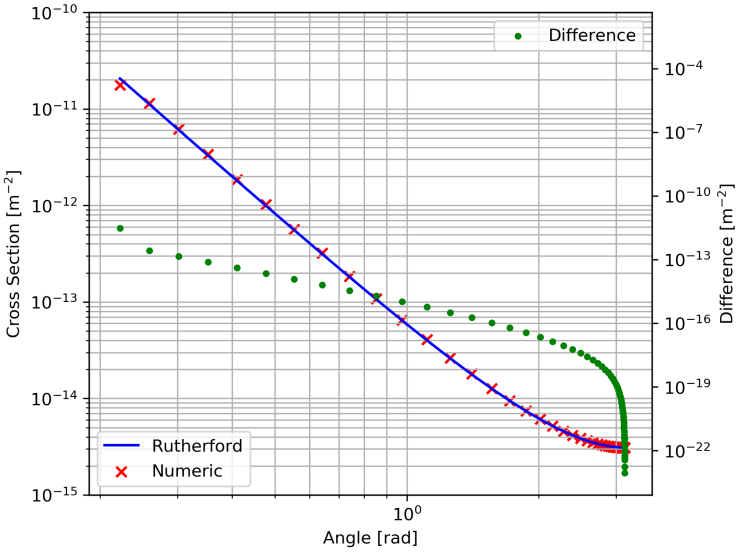

Figure D.4: Comparison between Rutherford's cross section and the numerical result.

Appendix E

Mirror Charge Configurations

It was shown before that for a planar cathode the correction function assumes the form of eqns (6.23), (6.24). This concept can be generalized to a family of symmetry maps S_j, where $S_j(\mathbf{x})$ is the j-th mirror charge to the original charge located at $\mathbf{x}$. The correction to the free Green's function assumes the following form,

$$G^C(\mathbf{x},\mathbf{y}) = \sum_j G(\mathbf{x}, S_j(\mathbf{y})),$$

where the summation goes over the family of maps or over mirror charges respectively. For the plane at $z = 0$, this must reduce to the known form (6.24),

$$S_j(x,y,z) = S_0(x,y,z) = (x,y,-z).$$

In order to convince ourselves of the validity of this approach and to get an idea of the properties of this map S, we can insert into Poisson's equation. Within the spatial volume V, one can obtain the following,

$$\begin{aligned}
\Delta\phi &\stackrel{!}{=} \rho \\
\Delta([G - G^C] \otimes \rho)(\mathbf{x}) &= \Delta(G \otimes \rho) - \Delta(G^C \otimes \rho) \\
&= (\Delta G) \otimes \rho - (\Delta G^C) \otimes \rho \\
&= \int d^3\ \mathbf{y}\ \Delta G(\mathbf{x}-\mathbf{y})\rho(\mathbf{y}) - \sum_j \int d^3\mathbf{y} \Delta G(\mathbf{x}, S_j(\mathbf{y}))\rho(\mathbf{y}) \\
&= \int d^3\ \mathbf{y}\ \delta(\mathbf{x}-\mathbf{y})\rho(\mathbf{y}) - \sum_j \int d^3\ \mathbf{y}\delta(\mathbf{x} - S_j(\mathbf{y}))\rho(\mathbf{y}) \\
&= \rho(\mathbf{x}) + \sum_j \rho(S_j^{-1}(\mathbf{x})) \\
&= \rho(\mathbf{x}),
\end{aligned}$$

where δ denotes the delta-distribution. Note that $\mathbf{x}$ lies in V and $S_j^{-1}(\mathbf{x})$ correspondingly outside of it. For Poisson's equation to be fulfilled, S may not map to positions that lie within V and it must approach $\mathbb{1}$ at the boundary.

This places a severe restriction on the cathode geometries that can be treated this way. Figure E.1 depicts an example of a boundary that is protruding. It is clearly visible, that not only are mirror charges required in the solution domain but the mirror charges that counter the original charge,

must be compensated as well. Since θ is not a multiple of π many mirror charges (potentially infinitely many) are needed.

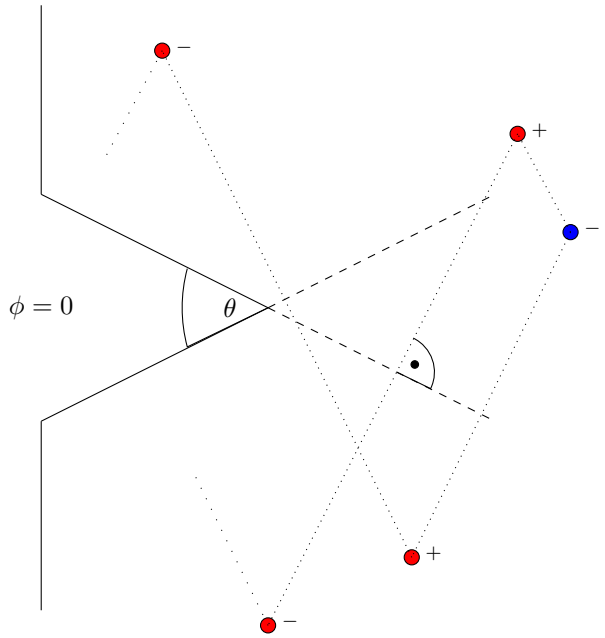

Figure E.1: Part of a mirror charge configuration, needed to balance the blue point charge.

If the indentation is perfectly spherical as depicted in figure E.2, one can find a mirror charge outside the charge domain, via spherical inversion [126]. Let's say the sphere of radius R is centred around $\mathbf{r}_s$ and the original charge is placed at $\mathbf{r}_0$. The mirror charge is then placed at,

$$S(\mathbf{r}_0) = \frac{R^2}{|\mathbf{r}_0 - \mathbf{r}_s|^2}(\mathbf{r}_0 - \mathbf{r}_s),$$

with the charge,

$$S(q) = \frac{R^2}{|\mathbf{r}_0 - \mathbf{r}_s|^2}q.$$

Nevertheless, infinitely many mirror charges are needed, once the rest of the surface $z = 0$ is required to be grounded. Additionally, while it is possible to find a finite amount of mirror charges for two intersecting spheres [126], as soon as two disconnected spheres are present, again the number of required images diverges. The more general case of elliptic surfaces can be obtained via conformal mapping from a spherical surface [108, 127, 128] and - again - requires outside charges.

In general one can say, that there are very few geometries, that can be solved using mirror charge configurations.

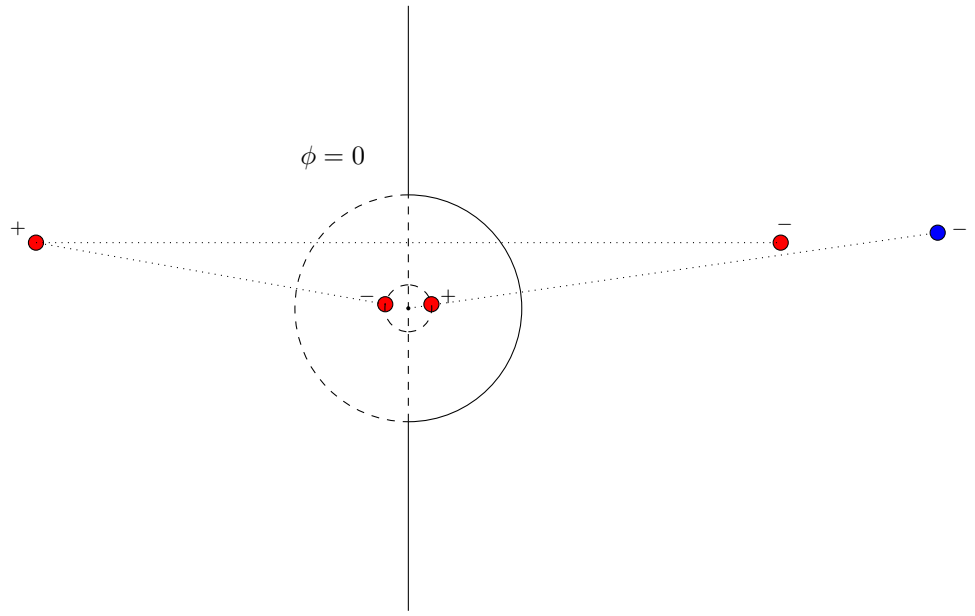

Figure E.2: The blue point charge cannot be countered by one single image if the potential must also vanish for $z = 0$.

References

[1] S. D. Baalrud and J. Daligault, "Effective potential theory for transport coefficients across coupling regimes," *Physical Review Letters*, vol. 110, no. 23, Jun. 4, 2013.

[2] J. Feng *et al.*, "Thermal limit to the intrinsic emittance from metal photocathodes," *Applied Physics Letters*, vol. 107, no. 13, Sep. 28, 2015.

[3] C. M. Pierce *et al.*, "The role of low intrinsic emittance in modern photoinjector brightness," *arXiv:2004.08034*, Apr. 16, 2020.

[4] C. M. Pierce *et al.*, "Low intrinsic emittance in modern photoinjector brightness," *Physical Review Accelerators and Beams*, vol. 23, no. 7, Jul. 21, 2020.

[5] G. Xia *et al.*, "An ultracold low emittance electron source," *Journal of Instrumentation*, vol. 9, no. 6, Jun. 2014.

[6] H. Lee, "For brighter electron sources: A cryogenically cooled photocathode and DC photogun," Ph.D. dissertation, Cornell University, Aug. 30, 2017.

[7] S. Karkare *et al.*, "Ultracold electrons via near-threshold photoemission from single-crystal cu(100)," *arXiv:2002.11579*, Feb. 26, 2020.

[8] M. Lyon and S. D. Bergeson, "The influence of electron screening on disorder-induced heating," *Journal of Physics B: Atomic, Molecular and Optical Physics*, vol. 44, no. 18, Sep. 2011.

[9] M. Lyon and S. L. Rolston, "Ultracold neutral plasmas," *Reports on Progress in Physics*, vol. 80, no. 1, Nov. 2016.

[10] B. J. Claessens *et al.*, "Ultracold electron source," *Physical Review Letters*, vol. 95, no. 16, Oct. 12, 2005.

[11] W. J. Engelen *et al.*, "Effective temperature of an ultracold electron source based on near-threshold photoionization," *Ultramicroscopy*, vol. 136, Jan. 1, 2014.

[12] J. Franssen, "An ultracold and ultrafast electron source," Ph.D. dissertation, Technische Universiteit Eindhoven, May 6, 2019.

[13] L. Greengard and V. Rokhlin, "A fast algorithm for particle simulations," *Journal of Computational Physics*, vol. 73, no. 2, Dec. 1, 1987.

[14] M. Gordon *et al.*, "The effects of stochastic space charge in high brightness photolectron beamlines for ultrafast electron diffraction," *Proceedings of the 10th Int. Particle Accelerator Conf.*, vol. IPAC2019, in collab. with B. Mark (Ed.) *et al.*, 2019.

[15] J. Grotendorst *et al.*, "Quantum simulations of complex many-body systems: From theory to algorithms," Jan. 1, 2002.

[16] R. W. Hockney and J. W. Eastwood, *Computer Simulation Using Particles*. CRC Press, Jan. 1, 1988, 566 pp., ISBN: 978-1-4398-2205-0.

[17] K. Matyash *et al.*, "P3m simulations of dusty plasmas," *Plasma Physics and Controlled Fusion*, vol. 52, no. 12, Nov. 2010.

[18] S. Aboud *et al.*, "A poisson p3m force field scheme for particle-based simulations of ionic liquids," *Journal of Computational Electronics*, vol. 3, no. 2, Apr. 1, 2004.

[19] K. Nanbu, "Theory of cumulative small-angle collisions in plasmas," *Physical Review E*, vol. 55, no. 4, Apr. 1, 1997.

[20] W. X. Wang *et al.*, "An accurate nonlinear monte carlo collision operator," National Institute for Fusion Science, Nagoya, Japan, 1995.

[21] A. M. Chap and R. J. Sedwick, "Coulomb collision model for use in nonthermal plasma simulation," *Physical Review E*, vol. 95, no. 6, Jun. 29, 2017.

[22] A. M. Dimits *et al.*, "Understanding the accuracy of nanbu's numerical coulomb collision operator," *Journal of Computational Physics*, vol. 228, no. 13, Jul. 20, 2009.

[23] P. N. Giuliano and I. D. Boyd, "Particle simulation of collision dynamics for ion beam injection into a rarefied gas," *Physics of Plasmas*, vol. 20, no. 3, Mar. 1, 2013.

[24] T. Takizuka and H. Abe, "A binary collision model for plasma simulation with a particle code," *Journal of Computational Physics*, vol. 25, no. 3, Nov. 1, 1977.

[25] J. Zhang *et al.*, "A particle-in-cell/monte-carlo-collision code for the simulation of stepwise ionization of lithium in 2.45 GHz ECR ion source," *Proceedings of the 23th Int. Workshop on ECR Ion Sources*, vol. ECRIS2018, in collab. with S. RW (Ed.) Volker and P. Pietro (Ed.), 2019.

[26] D. Wu *et al.*, "Monte carlo approach to calculate ionization dynamics of hot solid-density plasmas within particle-in-cell simulations," *Physical Review E*, vol. 95, no. 2, Feb. 16, 2017.

[27] V. Vahedi and M. Surendra, "A monte carlo collision model for the particle-in-cell method: Applications to argon and oxygen discharges," *Computer Physics Communications*, Particle Simulation Methods, vol. 87, no. 1, May 2, 1995.

[28] P. P. J. M. Schram, "Klimontovich equation, b.b.g.k.y.-hierarchy and vlasov-maxwell equations," in *Kinetic Theory of Gases and Plasmas*, ser. Fundamental Theories of Physics, P. P. J. M. Schram, Ed., Dordrecht: Springer Netherlands, 1991, ISBN: 978-94-011-3612-9.

[29] P. Degond *et al.*, Eds., *Modeling and Computational Methods for Kinetic Equations*, Modeling and Simulation in Science, Engineering and Technology, Birkhäuser Basel, 2004, ISBN: 978-0-8176-3254-0.

[30] C. Birdsall, "Particle-in-cell charged-particle simulations, plus monte carlo collisions with neutral atoms, PIC-MCC," *IEEE Transactions on Plasma Science*, vol. 19, no. 2, Apr. 1991.

[31] M. H. Mendenhall and R. A. Weller, "An algorithm for computing screened coulomb scattering in geant4," *Nuclear Instruments and Methods in Physics Research Section B: Beam Interactions with Materials and Atoms*, vol. 227, no. 3, Jan. 2005.

[32] H. Risken and T. Frank, *The Fokker-Planck Equation: Methods of Solution and Applications*, 2nd ed., ser. Springer Series in Synergetics. Berlin Heidelberg: Springer-Verlag, 1996, ISBN: 978-3-540-61530-9.

[33] M. G. Cadjan and M. F. Ivanov, "Langevin approach to plasma kinetics with coulomb collisions," *Journal of Plasma Physics*, vol. 61, no. 1, Jan. 1999.

[34] J. Daligault, "On the quantum landau collision operator and electron collisions in dense plasmas," *Physics of Plasmas*, vol. 23, no. 3, Mar. 2016.

[35] Ji Qiang *et al.*, "Self-consistent langevin simulation of coulomb collisions in charged-particle beams," in *ACM/IEEE SC 2000 Conference (SC'00)*, Dallas, TX, USA: IEEE, 2000, ISBN: 978-0-7803-9802-3.

[36] M. E. Jones *et al.*, "A grid-based coulomb collision model for PIC codes," *Journal of Computational Physics*, vol. 123, no. 1, Jan. 1, 1996.

[37] W. M. Manheimer *et al.*, "Langevin representation of coulomb collisions in PIC simulations," *Journal of Computational Physics*, vol. 138, no. 2, Dec. 1, 1997.

[38] J. P. H. Goedbloed *et al.*, *Principles of Magnetohydrodynamics: With Applications to Laboratory and Astrophysical Plasmas*. Cambridge University Press, Aug. 5, 2004, 646 pp., ISBN: 978-0-521-62607-1.

[39] A. Piel, *Plasma Physics*. Berlin Heidelberg: Springer-Verlag, 2010, ISBN: 978-3-642-10490-9.

[40] S. F. Ruggiero, "Kinetic theory of charged particle beams," *Proceedings of the third Advanced Accelerator Physics Course*, 1989.

[41] S. D. Baalrud and J. Daligault, "Extending plasma transport theory to strong coupling through the concept of an effective interaction potential," *Physics of Plasmas*, vol. 21, no. 5, May 1, 2014.

[42] S. D. Baalrud, "Transport coefficients in strongly coupled plasmas," *Physics of Plasmas*, vol. 19, no. 3, Mar. 1, 2012.

[43] J.-P. Hansen and I. R. McDonald, "Theory of simple liquids," in *Theory of Simple Liquids (Fourth Edition)*, Oxford: Academic Press, Jan. 1, 2013, ISBN: 978-0-12-387032-2.

[44] A. Busigin and C. R. Phillips, "Efficient newton-raphson and implicit euler methods for solving the HNC equation," *Molecular Physics*, vol. 76, no. 1, May 1, 1992.

[45] G. M. Abernethy and M. J. Gillan, "A new method of solving the HNC equation for ionic liquids," *Molecular Physics*, vol. 39, no. 4, Mar. 1, 1980.

[46] R. Bredow, "Berechnung der struktureigenschaften dichter plasmen mit der classical-map hypernetted chain approximation," Ph.D. dissertation, Rostock, Sep. 30, 2016, 137 pp.

[47] K.-C. Ng, "Hypernetted chain solutions for the classical one-component plasma up to =7000," *The Journal of Chemical Physics*, vol. 61, no. 7, Oct. 1, 1974.

[48] J. Anta *et al.*, "A fast method of solving the hypernetted-chain equation for molecular lennard-jones fluids," *Molecular Physics*, vol. 84, no. 4, Mar. 1995.

[49] M. S. Wertheim, "Exact solution of the percus-yevick integral equation for hard spheres," *Physical Review Letters*, vol. 10, no. 8, Apr. 15, 1963.

[50] M. Bonitz, *Quantum Kinetic Theory*. Cham: Springer International Publishing, 2016, ISBN: 978-3-319-24119-7.

[51] L. G. Garcia *et al.*, "Modified zakharov equations for plasmas with a quantum correction," *Physics of Plasmas*, vol. 12, no. 1, Dec. 3, 2004.

[52] F. Haas, "A magnetohydrodynamic model for quantum plasmas," *Physics of Plasmas*, vol. 12, no. 6, Jun. 1, 2005.

[53] F. Haas *et al.*, "Multistream model for quantum plasmas," *Physical Review E*, vol. 62, no. 2, Aug. 1, 2000.

[54] M. Marklund and G. Brodin, "Dynamics of spin-1/2 quantum plasmas," *Physical Review Letters*, vol. 98, no. 2, Jan. 8, 2007.

[55] Z. Moldabekov *et al.*, "Statically screened ion potential and bohm potential in a quantum plasma," *Physics of Plasmas*, vol. 22, no. 10, Oct. 1, 2015.

[56] P. K. Shukla, "A new dust mode in quantum plasmas," *Physics Letters A*, vol. 352, no. 3, Mar. 27, 2006.

[57] M. Bonitz *et al.*, "Quantum hydrodynamics for plasmas—quo vadis?" *Physics of Plasmas*, vol. 26, no. 9, Sep. 1, 2019.

[58] M. Bonitz *et al.*, "Attractive forces between ions in quantum plasmas: Failure of linearized quantum hydrodynamics," *Physical Review E*, vol. 87, no. 3, Mar. 20, 2013.

[59] G. Brodin *et al.*, "Quantum plasma effects in the classical regime," *Physical Review Letters*, vol. 100, no. 17, Apr. 28, 2008.

[60] S. P. Thampi *et al.*, "Lattice-boltzmann-langevin simulations of binary mixtures," *Physical Review E*, vol. 84, no. 4, Oct. 24, 2011.

[61] Y.-D. Jung, "Quantum-mechanical effects on electron–electron scattering in dense high-temperature plasmas," *Physics of Plasmas*, vol. 8, no. 8, Jul. 18, 2001.

[62] T. S. Ramazanov *et al.*, "Multipole expansion in plasmas: Effective interaction potentials between compound particles," *Physical Review E*, vol. 93, no. 5, May 9, 2016.

[63] L. G. Stanton and M. S. Murillo, "Unified description of linear screening in dense plasmas," *Physical Review E*, vol. 91, no. 3, Mar. 6, 2015.

[64] W. Steffen and H.-J. Kull, "Relaxation of plasma waves in fermi-degenerate quantum plasmas," *Physical Review E*, vol. 93, no. 3, Mar. 25, 2016.

[65] H. D. Whitley *et al.*, "Lenard-balescu calculations and classical molecular dynamics simulations of electrical and thermal conductivities of hydrogen plasmas," *Contributions to Plasma Physics*, vol. 55, no. 2, Feb. 1, 2015.

[66] F. R. Graziani *et al.*, "Large-scale molecular dynamics simulations of dense plasmas: The cimarron project," *High Energy Density Physics*, vol. 8, no. 1, Mar. 1, 2012.

[67] K. E. Nagaev, "Reprint of : The boltzmann–langevin approach: A simple quantum-mechanical derivation," *Physica E: Low-dimensional Systems and Nanostructures*, Frontiers in quantum electronic transport - In memory of Markus Büttiker, vol. 82, Aug. 1, 2016.

[68] C. Ullrich, "Time-dependent density-functional theory: Features and challenges, with a special view on matter under extreme conditions," in *Frontiers and Challenges in Warm Dense Matter*, ser. Lecture Notes in Computational Science and Engineering, F. Graziani *et al.*, Eds., Springer International Publishing, 2014, ISBN: 978-3-319-04911-3.

[69] J. Tonge *et al.*, "Two-dimensional semiclassical particle-in-cell code for simulation of quantum plasmas," *Computer Physics Communications*, Proceedings of the 18th International Conferene on the Numerical Simulation of Plasmas, vol. 164, no. 1, Dec. 1, 2004.

[70] M. W. C. Dharma-Wardana and F. Perrot, "A simple classical mapping of the spin-polarized quantum electron gas: Distribution functions and local field corrections," *Physical Review Letters*, vol. 84, no. 5, Jan. 31, 2000.

[71] R. Bredow *et al.*, "Classical-map hypernetted chain calculations for dense plasmas: Classical-map hypernetted chain calculations for dense plasmas," *Contributions to Plasma Physics*, vol. 55, no. 2, Feb. 2015.

[72] G. Kelbg, "Theorie des quanten-plasmas," *Annalen der Physik*, vol. 467, no. 3, 1963.

[73] H. Minoo *et al.*, "Temperature-dependent coulomb interactions in hydrogenic systems," *Physical Review A*, vol. 23, no. 2, Feb. 1, 1981.

[74] R. Bredow *et al.*, "Hypernetted chain calculations for multi-component and NonEquilibrium plasmas," *Contributions to Plasma Physics*, vol. 53, no. 4, 2013.

[75] M. K. Issanova *et al.*, "Classical scattering and stopping power in dense plasmas: The effect of diffraction and dynamic screening," *Laser and Particle Beams*, vol. 34, no. 3, Sep. 2016.

[76] A. Campa *et al.*, *Physics of Long-Range Interacting Systems*. Oxford University Press, 2014, ISBN: 978-0-19-178714-0.

[77] C. Villani, "Chapter 2 - a review of mathematical topics in collisional kinetic theory," in *Handbook of Mathematical Fluid Dynamics*, S. Friedlander and D. Serre, Eds., vol. 1, North-Holland, Jan. 1, 2002, ISBN: 978-0-444-50330-5.

[78] R. Alexandre and C. Villani, "On the landau approximation in plasma physics," *Annales de l'Institut Henri Poincare (C) Non Linear Analysis*, vol. 21, no. 1, Jan. 1, 2004.

[79] P. Danielewicz, "Nonrelativistic and relativistic landau/fokker-planck equation for arbitrary statistics," *Physica A: Statistical Mechanics and its Applications*, vol. 100, no. 1, Jan. 1, 1980.

[80] J. D. Huba, "NRL plasma formulary," Naval Research Lab Washington DC, Plasma Physics Division, 2019.

[81] M. N. Rosenbluth *et al.*, "Fokker-planck equation for an inverse-square force," *Physical Review*, vol. 107, no. 1, Jul. 1, 1957.

[82] S. D. Baalrud, "A generalized coulomb logarithm for strongly coupled plasmas," *arXiv:1109.4826*, Dec. 1, 2011.

[83] M. Honda, "Coulomb logarithm formulae for collisions between species with different temperatures," *Japanese Journal of Applied Physics*, vol. 52, no. 10, Oct. 1, 2013.

[84] P. Mulser *et al.*, "Revision of the coulomb logarithm in the ideal plasma," *Physics of Plasmas*, vol. 21, no. 4, Apr. 2014.

[85] J. A. Krommes, "An introduction to the physics of the coulomb logarithm with emphasis on quantum-mechanical effects," *Journal of Plasma Physics*, vol. 85, no. 1, Feb. 2019.

[86] Y. Chang and D. Li, "The correct cutoff for rutherford scattering cross-section," *Plasma Research Express*, vol. 2, no. 2, Apr. 16, 2020.

[87] Y. Chang, "The failure of the scattering angle cutoff for coulomb interactions," *Physics of Plasmas*, vol. 13, no. 1, Jan. 2006.

[88] Y. Chang and D. Li, "Normal approach to the linearized fokker-planck equation for the inverse-square force," *Physical Review E*, vol. 53, no. 4, Apr. 1, 1996.

[89] Y. Chang, "The concept of collision strength and a unified kinetic calculation for hard-sphere interactions and inverse square force law interactions," *Physics of Plasmas*, vol. 10, no. 12, Nov. 20, 2003.

[90] M. R. Zaghloul, "On the cutoff distance and the classical energy-averaged electron–ion momentum transport cross section in ideal and nonideal plasmas," *IEEE Transactions on Plasma Science*, vol. 46, no. 2, Feb. 2018.

[91] G. E. Cooper and P. T. Herman, "Effect of velocity dependence of coulomb logarithm on the solution of the fokker-planck equation," *The Physics of Fluids*, vol. 16, no. 1, Jan. 1, 1973.

[92] C. A. Ordonez and M. I. Molina, "Evaluation of the coulomb logarithm using cutoff and screened coulomb interaction potentials," *Physics of Plasmas*, vol. 1, no. 8, Aug. 1, 1994.

[93] C. K. Li, "A fokker-planck equation for moderately," 1993.

[94] F. E. Low and S. Chandrasekhar, "A lagrangian formulation of the boltzmann-vlasov equation for plasmas," *Proceedings of the Royal Society of London. Series A. Mathematical and Physical Sciences*, vol. 248, no. 1253, Nov. 11, 1958.

[95] J. J. Galloway and H. Kim, "Lagrangian approach to non-linear wave interactions in a warm plasma," *Journal of Plasma Physics*, vol. 6, no. 1, Aug. 1971.

[96] E. Hirvijoki, "Action principle for coulomb collisions in plasmas," *Physics of Plasmas*, vol. 23, no. 9, Sep. 14, 2016.

[97] E. G. Evstatiev and B. A. Shadwick, "Variational formulation of particle algorithms for kinetic plasma simulations," *Journal of Computational Physics*, vol. 245, Jul. 2013.

[98] J. M. Berger and G. J. Lasher, "The use of discrete green's functions in the numerical solution of poisson's equation," *Illinois Journal of Mathematics*, vol. 2, no. 4, Nov. 1958.

[99] M. Kraus, "Variational integrators in plasma physics," Ph.D. dissertation, Technische Universität München, Dec. 5, 2014.

[100] A. Lew *et al.*, "An overview of variational integrators," *Finite Element Methods*, 2003.

[101] C. Rowley and J. Marsden, "Variational integrators for degenerate lagrangians, with application to point vortices," in *Proceedings of the 41st IEEE Conference on Decision and Control, 2002.*, vol. 2, Las Vegas, NV, USA: IEEE, 2002, ISBN: 978-0-7803-7516-1.

[102] D. Frenkel and B. Smit, *Understanding Molecular Simulation*. Elsevier, 2002, ISBN: 978-0-12-267351-1.

[103] R. W. Hockney, "Potential calculation and some applications," *Methods Comput. Phys. 9: 135-211(1970).*, 1970.

[104] M. Deserno and C. Holm, "How to mesh up ewald sums (II): An accurate error estimate for the particle–particle–particle-mesh algorithm," *The Journal of Chemical Physics*, vol. 109, no. 18, Nov. 8, 1998.

[105] M. Deserno and C. Holm, "How to mesh up ewald sums (i): A theoretical and numerical comparison of various particle mesh routines," *The Journal of Chemical Physics*, vol. 109, no. 18, Nov. 8, 1998.

[106] B. Ulmer, "The p3m model on emerging computer architectures with application to microbunching," ETHZ, Zurich, Master's Thesis, Jun. 30, 2016.

[107] A. Pukhov, "Particle-in-cell codes for plasma-based particle acceleration," *CERN Yellow Reports*, vol. 1, no. 0, Feb. 16, 2016.

[108] H. Alshal *et al.*, "Image charges re-imagined," *arXiv:1808.08300*, Dec. 4, 2018.

[109] R. Nelson *et al.*, "Using image theory for finite electrostatic problems-some observations and guidelines," in *IEEE 1997, EMC, Austin Style. IEEE 1997 International Symposium on Electromagnetic Compatibility. Symposium Record (Cat. No.97CH36113)*, Austin, TX, USA: IEEE, 1997, ISBN: 978-0-7803-4140-1.

[110] J. Qiang *et al.*, "A parallel particle-in-cell model for beam–beam interaction in high energy ring colliders," *Journal of Computational Physics*, vol. 198, no. 1, 2004.

[111] G. Xia *et al.*, "Ultracold and high brightness electron source for next generation particle accelerators," in *Proceedings, 4th International Particle Accelerator Conference*, Shanghai, China, 2013.

[112] J. M. Maxson *et al.*, "Fundamental photoemission brightness limit from disorder induced heating," *New Journal of Physics*, vol. 15, no. 10, Oct. 2013.

[113] J. Qiang, "Symplectic multiparticle tracking model for self-consistent space-charge simulation," *Physical Review Accelerators and Beams*, vol. 20, no. 1, Jan. 23, 2017.

[114] J. Qiang, "Symplectic particle-in-cell model for space-charge beam dynamics simulation," *Physical Review Accelerators and Beams*, vol. 21, no. 5, May 29, 2018.

[115] J. Makhoul, "A fast cosine transform in one and two dimensions," *IEEE Transactions on Acoustics, Speech, and Signal Processing*, vol. 28, no. 1, Feb. 1980.

[116] J. F. Springer *et al.*, "Integral equation solutions for the classical electron gas," *The Journal of Chemical Physics*, vol. 58, no. 11, Jun. 1, 1973.

[117] S. M. Candel, "An algorithm for the fourier-bessel transform," *Computer Physics Communications*, vol. 23, no. 4, Aug. 1, 1981.

[118] S. M. Candel, "Simultaneous calculation of fourier-bessel transforms up to order n," *Journal of Computational Physics*, vol. 44, no. 2, Dec. 1, 1981.

[119] F. Lado *et al.*, "Solutions of the reference-hypernetted-chain equation with minimized free energy," *Physical Review A*, vol. 28, no. 4, Oct. 1, 1983.

[120] M. D. Rintoul and S. Torquato, "Reconstruction of the structure of dispersions," *Journal of Colloid and Interface Science*, vol. 186, no. 2, Feb. 15, 1997.

[121] R. G. Newton, *Scattering Theory of Waves and Particles*. Berlin, Heidelberg: Springer Berlin Heidelberg, 1982, ISBN: 978-3-642-88130-5.

[122] K. S. Krane, *Introductory Nuclear Physics*. Wiley India, 2008, 874 pp., ISBN: 978-81-265-1785-5.

[123] M. Semon and J. Taylor, "Cross sections for screened potentials," *Journal of Mathematical Physics*, vol. 17, Jan. 1975.

[124] M. T. Robinson, "Tables of classical scattering integrals," Oak Ridge National Lab., Tenn., ORNL-4556, Jan. 1, 1970.

[125] M. H. Mendenhall and R. A. Weller, "Algorithms for the rapid computation of classical cross sections for screened coulomb collisions," *Nuclear Instruments and Methods in Physics Research Section B: Beam Interactions with Materials and Atoms*, vol. 58, no. 1, May 2, 1991.

[126] I. V. Lindell *et al.*, "Electrostatic image theory for two intersecting conducting spheres," *Journal of Electromagnetic Waves and Applications*, vol. 17, no. 11, Jan. 2003.

[127] G. Dassios, "Directional dependent green's function and kelvin images," *Archive of Applied Mechanics*, vol. 82, no. 10, Oct. 2012.

[128] T. L. Curtright *et al.*, "Charged line segments and ellipsoidal equipotentials," *European Journal of Physics*, vol. 37, no. 3, May 1, 2016.